

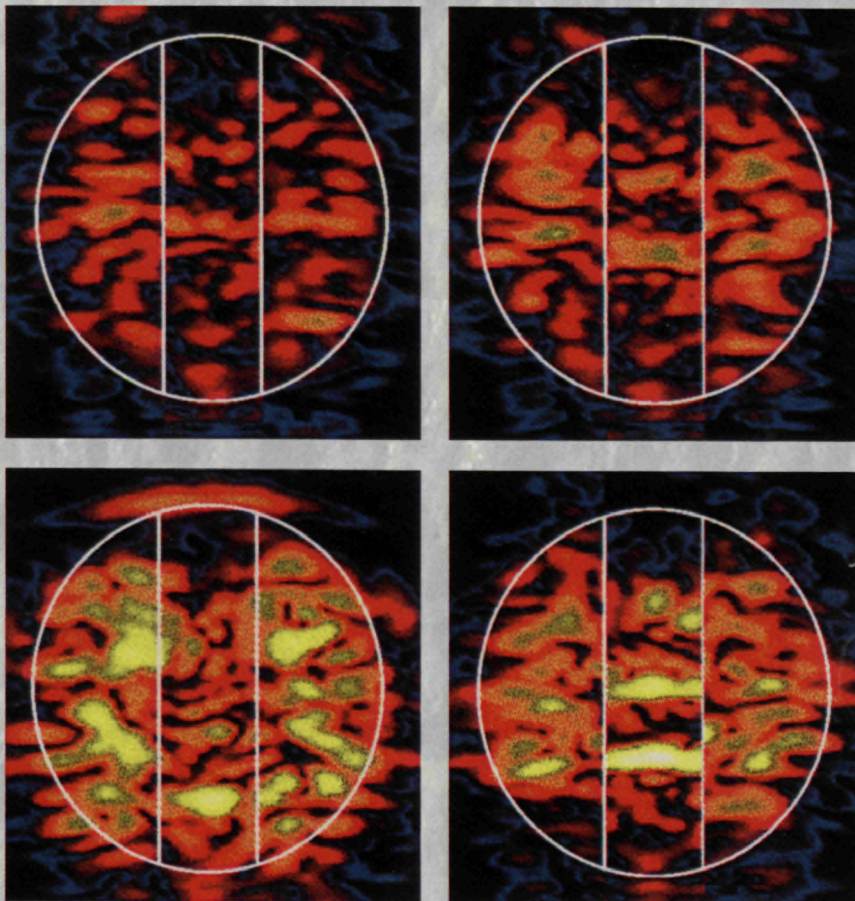


EUROPEAN MICROWAVE SIGNATURE LABORATORY

1st EMSL USER WORKSHOP

Ispra 23/24 April 1996

Proceedings



Organised by:
Space Application Institute
Advanced Techniques Unit



EUR 17326 EN



1st EMSL USER WORKSHOP - PROCEEDINGS

559 gr
C21 21637
C22 1530



EUROPEAN MICROWAVE SIGNATURE LABORATORY

1st EMSL USER WORKSHOP

Ispra 23/24 April 1996

Proceedings

Edited by:
G. Nesti

Organised by:
Space Application Institute
Advanced Techniques Unit

LEGAL NOTICE

Neither the European Commission nor any person acting on behalf of the Commission is responsible for the use which might be made of the following information

Cataloguing data can be found at the end of this publication

Contents

Introduction	III
Part I: Results of working with EMSL	1
Adaptive algorithm for SAR Subsurface Imaging J. Fortuny and A.J. Sieber	3
The RoCoCo Project: a cooperation between EMSL and Daimler-Benz H. Rudolf and E. Ohlmer	13
SAR focusing and interferometry experiments with EMSL data P. Pasquali, C. Prati and F. Rocca.....	19
Laboratory experiments for the interpretation of phase shift in SAR interferograms J.P. Rudant, A. Bédidi, R. Calonne, D. Massonnet, G. Nesti and D. Tarchi,	31
Microwave scattering from randomly rough surfaces: electromagnetic models and experimental data P. Coppo, P. Pampaloni and S. Lolli.....	41
Estimating microwave observation depth in bare soil through multi-frequency scatterometry P.A. Troch, F. Vandersteene, Z. Su, R. Hoeben and M. Wuethrich.....	45
Part II: New ideas for potential use of EMSL	55
A circular synthetic aperture radar system for ground-based applications A. Broquetas, R. De Porrata and Ll. Sagues	57
The inversion of objects buried in a layered embedding: the outline of a multi-pronged investigation D. Lesselier and B. Duchêne.....	67
Inversion algorithms for microwave imaging using different modalities and for various applications Ch. Pichot, P. Lobel, C. Dourthe, L. Blanc-Féraud and M. Barlaud.....	75
Localisation and identification of anti-personal mines: the JRC Study Report A.J. Sieber	87
Reference targets P. Corona, G. Ferrara, C. Gennarelli and G. Riccio	91
The task force “Car of Tomorrow” oriented to telematics technologies integration Y.R. Crutzen	101
Noise radar technology for civilian applications K.A. Lukin	105
Bare soil surfaces and electromagnetic scattering: a fractal approach P. Borderies, S. Rouvier, I. Chênerie, M. Jauregui, C. Ruiz, J.C. Sourys, T. Le Toan, N. Floury and F. Mattia	113

Experiments on precipitation detection and soil moisture measurements M. Martin-Neira	133
Experimental proposal on backscattering enhancement and clustering effects on artificial random media: application to bare soil a vegetation canopy P. Coppo, P. Pampaloni and P. Brusaglioni.....	141
Proposal for an experimental investigations of soil radio physical property peculiarities on soil moisture content N.V. Ruzhentsev	145
List of participants.....	155

Introduction

The first EMSL User Workshop was held at the JRC, Ispra on 23 and 24 April 1996.

The main objectives of the workshop were:

- to provide a status report to the scientific and industrial user community after almost four years of operating this unique facility,
- to raise the visibility of the EMSL user groups and
- to foster co-operation between scientists as well as with industrial customers.

All these are important in relation to the request by the Board of Governors of the JRC and its Director General to submit proposals to EC Programmes (e.g. Training and Mobility of Researchers; Standards, Measurements & Testing), to create thematic networks, to support and diversify the EMSL activity and to finance the access of external users. In addition, it is important to make an active contribution to a future European programme on the improvement of sensors for detecting anti-personnel mines and to the task force "Car of Tomorrow".

About 50 experts attended the meeting from EU countries and from Israel, USA and Ukraine. The workshop comprised seven sessions, related to a wide range of topics including SAR Imaging and Interferometry, industrial applications of microwave sensors, scattering modelling and signal analysis. The EMSL Advisory Committee originally identified these themes as priority research topics.

With regard to the industrial use of radar sensors, one session of the workshop was dedicated to the proposed European RTD programme on the improvement of searching methods for anti-personnel mines, and another to a possible EMSL contribution to the European Commission "Car of Tomorrow" task force.

The papers collected in these Proceedings cover all the topics presented and discussed at the workshop, divided into two parts:

- the first deals with results of working with EMSL related in particular to the activities of the user subgroups on Imaging Techniques, Interferometry Techniques, Scattering from Non Vegetated Terrain, and to the Road Condition and Control (RoCoCo) Project.
- the second looks at ideas for using the EMSL, ranging from validation of scattering models to testing and validation of new sensors, measurement and inversion techniques for applications in remote sensing and industrial fields.

These Proceedings confirm the conclusions of the workshop, showing that there is a need for the EMSL facility, with demand from research establishments and industry.

Giuseppe Nesti
AT/EMSL
Space Applications Institute
JRC, Ispra

Part 1
Results of working with
EMSL

Adaptive Algorithm for SAR Subsurface Imaging

J. Fortuny-Guasch and A.J. Sieber
SAI-AT, Joint Research Centre
I-21020 Ispra (Va), Italy

Abstract

This paper presents an adaptive algorithm for the formation of SAR subsurface images. Focusing a SAR subsurface image presents a number of additional problems (compared to conventional SAR) even when the soil's properties are known. The effects of refraction, dispersion and propagation losses on the SAR's phase history must be taken into account when forming the imagery. It is shown that, assuming the soil surrounding the target has been properly characterized, one can form the image by correcting the phase history with the effective propagation constant. This will result in a higher signal to clutter ratio and lower geometric distortion. Experimental results show a remarkable performance of the presented algorithm.

1 Introduction

The development of subsurface radar techniques for the detection and location of buried objects has received considerable interest for many years [1, 2]. Fields of application of such techniques include underground probing, archaeological surveying, nondestructive evaluation and others. One application area which has gained considerable attention is the use of vehicle-mounted Synthetic Aperture Radar (SAR) for detecting anti-personnel mines (APMs) [3, 4]. The mean size of the anti-personnel mines range from 5 to 15 cm. APMs are usually on the ground or just beneath the surface, being the maximum depth around 30 cm. The spatial resolution required to be able to identify the APMs against other objects such as ordnance, stones or soil inhomogeneities is in the order of 4 cm. This leads to the need to have a stand-off imaging system operating in the near-field. 3-D capability and high dynamic range are required in order to help discriminate buried targets from surface clutter. Focusing a SAR subsurface image presents a number of additional problems (compared to conventional SAR) even when the soil's properties are known. The effects of refraction, dispersion and propagation losses on the SAR's phase history must be taken into account when forming the imagery. Assuming the soil surrounding the target has been properly characterized, one can form the image by correcting the phase history with the effective propagation constant. This will result in a higher signal to clutter ratio and lower geometric distortion.

This paper is organized as follows. The formulation involved in the formation of the subsurface images is addressed in Section II. A description of the experimental validation undertaken with measurement data acquired at the EMSL is given in Section III. Results obtained with the proposed algorithm are shown in Section IV. The concluding remarks are summarized in Section V.

2 Problem Formulation

The geometry of measurement is shown in Figure 1, where a TX/RX antenna off the ground illuminates the air-ground interface with a looking angle θ_i . This antenna can be displaced both along an arc (by changing the looking angle) and along a linear axis parallel to the interface (x-axis), forming a two-dimensional synthetic aperture which will provide spatial resolution in the three dimensions.

2.1 Lossless Soil

Modelling the subsurface medium as homogeneous, isotropic and non-magnetic, one can define a correction term for the changes in the phase history due to the differences in the propagation constants. In the medium the wavelength will become shorter and therefore the wavefront will propagate with a lower velocity. This means that when reconstructing the reflectivity at a point underground the phase term will include an additional phase shift due to the higher propagation constant of the medium.

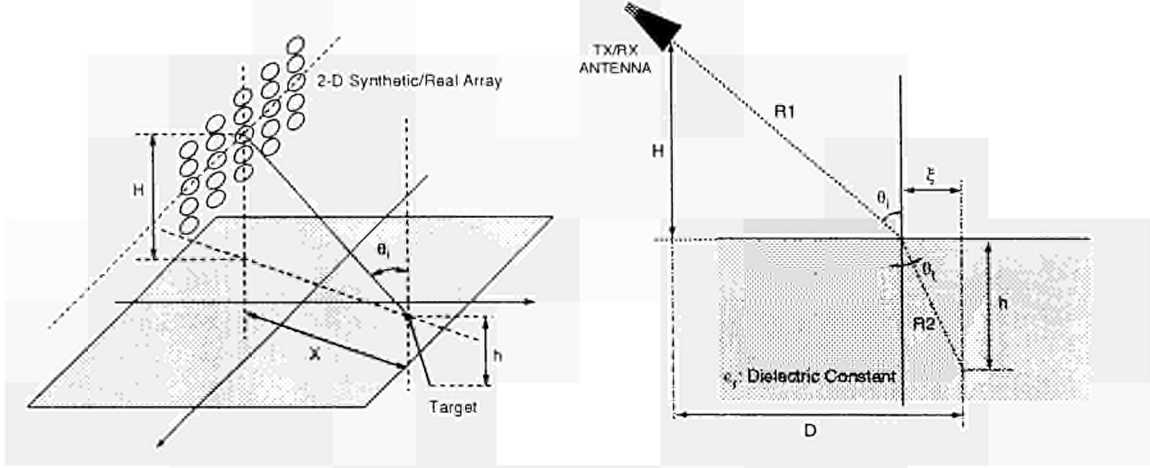


Figure 1: Imaging geometry for 3-D subsurface sensing.

In the processing of SAR data, it is usually assumed that the target response is independent of the observation angle. For subsurface sensing, this assumption is usually not satisfied and a new focusing technique taking account of this problem is required. Calculating the backscatter from a shallow sub-surface is a difficult electromagnetics problem to solve. Here, a simple model which assumes the incident spherical wave to be locally planar is used. Hence, considering a point scatterer underground at a depth h , its associated phase history will be defined by the electrical length of the two-way path travelled by an spherical wave from the antenna to the point scatterer. In order to calculate accurately such a distance, one must find the point on the surface where the refraction takes place. The position of this point will be the solution of the Snell equation of refraction, thus,

$$\begin{aligned} R &= R_1 + R_2 \\ &= \sqrt{H^2 + (D - \xi)^2} + \sqrt{\epsilon_r} \sqrt{h^2 + \xi^2} \end{aligned} \quad (1)$$

where R is the electrical length, R_1 and R_2 are the electrical lengths in the air and in the medium, respectively; ϵ_r is the relative dielectric constant of the medium, H is the height of the antenna, and ξ denotes the horizontal distance between the antenna and the point scatterer, which can be obtained by finding the zero of the following function,

$$\begin{aligned} F(\xi) &= \sin\theta_i - \sqrt{\epsilon_r} \sin\theta_r \\ &= \frac{D - \xi}{\sqrt{H^2 + (D - \xi)^2}} - \sqrt{\epsilon_r} \frac{\xi}{\sqrt{h^2 + \xi^2}} \end{aligned} \quad (2)$$

Once the electrical length R is known for each antenna position, it is used to correct for the distortion due to the differences in the propagation constant. It is clear that such a correction is applicable only when one knows a priori the dielectric properties of the medium surrounding the target of interest. Furthermore, the relative position of the antenna referred to the interface must be precisely known.

2.2 Lossy Soil

When the medium is lossy ($\epsilon_r = \epsilon' - j\epsilon''$), see Figure 2, the planes of constant phase and those of constant amplitude do not coincide and the direction of propagation is determined by the normal to the constant phase planes \hat{n}_ψ , which is given by,

$$\tan \psi_t = \frac{\sqrt{2} \tan \theta'_t}{\sqrt{1 + \sqrt{1 + \left(\frac{2 \tan \delta}{\cos^2 \theta'_t}\right)^2}}} \quad (3)$$

where $\tan \delta$ is the loss tangent and $\sin \theta'_t = \frac{\sin \theta_i}{\sqrt{\epsilon'}}$. The total electrical length (one-way) is now expressed as,

$$R = R_1 + n(\theta_i)R_2 = \sqrt{H^2 + (D - \xi)^2} + \frac{\beta_e}{(w/c)} \sqrt{h^2 + \xi^2} \quad (4)$$

where $n(\theta_i)$ is the effective refractive index which depends on the incidence angle, and ξ is obtained by finding the zero of the following function,

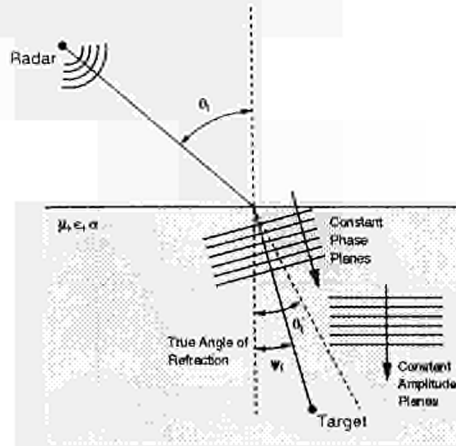


Figure 2: Scenario with a lossy medium surrounding the target of interest

$$F(\xi) = \sin \theta_i - \frac{\beta_e}{(w/c)} \sin \psi_t = \frac{D - \xi}{\sqrt{H^2 + (D - \xi)^2}} - n(\theta_i) \frac{\xi}{\sqrt{h^2 + \xi^2}} \quad (5)$$

where β_e and α_e denote the effective phase and amplitude constants, respectively, and are given by,

$$\begin{aligned} \beta_e &= \frac{w}{c} \sqrt{\epsilon'} \sqrt{\frac{1 + \sin^2 \theta'_t}{2} + \sqrt{\tan^2 \delta + \left(\frac{\cos^2 \theta'_t}{2}\right)^2}} \\ \alpha_e &= \frac{w}{c} \sqrt{\epsilon'} \sqrt{-\frac{\cos^2 \theta'_t}{2} + \sqrt{\tan^2 \delta + \left(\frac{\cos^2 \theta'_t}{2}\right)^2}} \\ \theta'_t &= \arcsin\left(\frac{\sin \theta_i}{\sqrt{\epsilon'}}\right) \end{aligned} \quad (6)$$

2.3 Imaging Algorithm

Considering that the antenna is located within the near-field region of the object underground. i.e. it illuminates the object with a spherical wavefront, and its radiation pattern introduces a negligible distortion, then the 3-D complex reflectivity image can be written as follows,

$$I(\mathbf{r}) \simeq \int_f df \int_{\theta_a} \theta_a \int_{x_a} E_s(f, x_a, \theta_a) F(|\mathbf{r} - \mathbf{r}_a|, f) dx_a \quad (7)$$

where θ_a denotes the antenna viewing angle, x_a is the cross-range coordinate of the antenna, and $F(\cdot)$ is a near-field focusing function (or space-variant matched filter) which can be expressed as.

$$F(|\mathbf{r} - \mathbf{r}_a|, f) = \exp[j2k(R - R_a)] \quad (8)$$

where R denotes the total electrical length between the antenna and the point with coordinates \mathbf{r} , R_a is the range to the center of the coordinates system and zero-phase reference point, and k is the frequency wavenumber. In Eq. (7), the exact near-field phase history is accounted for by the exponential function. This is a generalized imaging algorithm [5] especially tailored for 3-D SAR subsurface imaging. It is important to note that the focusing function $F(\cdot)$ is defined only by the measurement geometry and the working frequency. Thus, if calculated once and stored on memory, $F(\cdot)$ could be reused with different data sets measured under the same conditions. This is the case of a fully polarimetric measurement, where four data sets have to be focused using identical processing parameters. The core of this algorithm resides in the calculation of the azimuth convolution in Eq. (7), which is efficiently implemented by using FFT codes.

Alternatively, when using a 2-D synthetic aperture that lays on the surface of a sphere, the 3-D complex reflectivity image is then given by,

$$I(\mathbf{r}) \simeq \int_f df \int_{\theta_a} d\theta_a \int_{\phi_a} E_s(f, \phi_a, \theta_a) F(|\mathbf{r} - \mathbf{r}_a|, f) d\phi_a \quad (9)$$

where ϕ_a and θ_a denote two rotation angles about axes which are mutually orthogonal.

3 Experimental Validation

The presented subsurface imaging algorithm has been validated experimentally using the anechoic chamber of the EMSL [6], a European large-scale facility tailored for subsurface 3-D linear and inverse SAR imaging. Two series of test measurements have been undertaken.

The target used in the first test measurement is a 3-D arrangement of eight metallic spheres of diameter 7.62 cm which are buried in dry sand ($\epsilon_r = 2.5$), as shown in Fig. 3. The measurement has been conducted with the same angular span in azimuth and elevation, with 61 points equally spaced within the ranges 0 to 45 deg for ϕ_a and 22.5 to 67.5 deg for θ_a , acquiring the backscattered fields in the HH polarization at 801 frequency points spaced 5 MHz within the frequency range 2 to 6 GHz. Here, the number of frequency points has been decimated by a factor of 10 after calibration. The range to the center of the coordinates system is again $R_a = 9.56$ m. The measurement time required in this experiment is approximately 50 h. Note that there are 3600 antenna positions on the spherical 2-D synthetic aperture. A 3-D ISAR image consisting of $N_z = 61$ horizontal slices on a polar raster with $N_\rho = 101$ and $N_\phi = 480$ has been reconstructed and is shown in Fig. 4. Achieved resolutions, as expected, are about 4 cm in the cross-range and height directions, and 6 cm in the ground-range direction.

The second test measurement has been conducted with nine metallic dihedrals buried in three types of lossy soils. The main characteristics of these soils are summarized in Tables 1 and 2.

The effective propagation constants have been estimated by measuring the backscattered fields on a sample of each soil confined in a box with a metallic plate underneath. These measurement have been conducted using two different frequency bands: 1.5 to 3.5 GHz and 1.5 to 5.5 GHz. As expected, the wider the frequency band, the higher the losses in the medium. Concerning the 3-D linear SAR measurement, the set-up is shown in Figure 5. The dihedrals are slightly tilted in order to be pointed towards the antenna. This is a 3-D linear SAR measurement with a total cross-range extent of 4 m. The synthetic aperture in elevation is 10 deg wide, covering the angular range from 40 to 50 deg. The sequence of horizontal slices using the measured effective propagation constant in the formation of the reflectivity image is shown in Figure 6. These slices correspond to the VV-polarization and the frequency range from 1 to 5 GHz. Note that the horizontal location as well as the depth are in agreement with the expected ones. The horizontal slice at 15 cm depth is shown separately in Figure 7 with a dynamic range of 10 dB.

Soil	Material	Mean Size (cm)
Soil 1	Backed Soil	1
Soil 2	Rolling Stones	3-8
Soil 3	Rugged Stones	3-8

Table 1: Materials characteristics in the measurement with the nine metallic dihedrals

Frequency Band:	1.5-3.5 GHz			1.5-5.5 GHz		
	Soil 1	Soil 2	Soil 3	Soil 1	Soil 2	Soil 3
α (dB/m)	20	70	85	25	120	110
β/β_0	1.4	1.7	1.9	1.4	1.7	1.9

Table 2: Measured phase and attenuation constants in the frequency ranges 1.5-3.5 GHz and 1.5-5.5 GHz

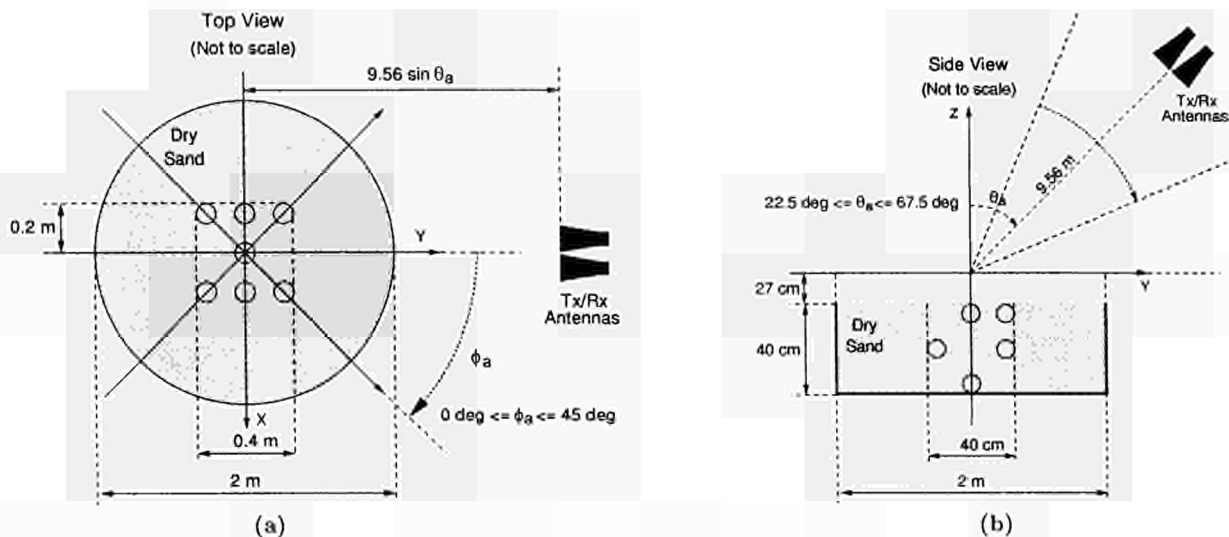


Figure 3: Measurement set-up with the eight metallic spheres underground: (a) top view and (b) side view

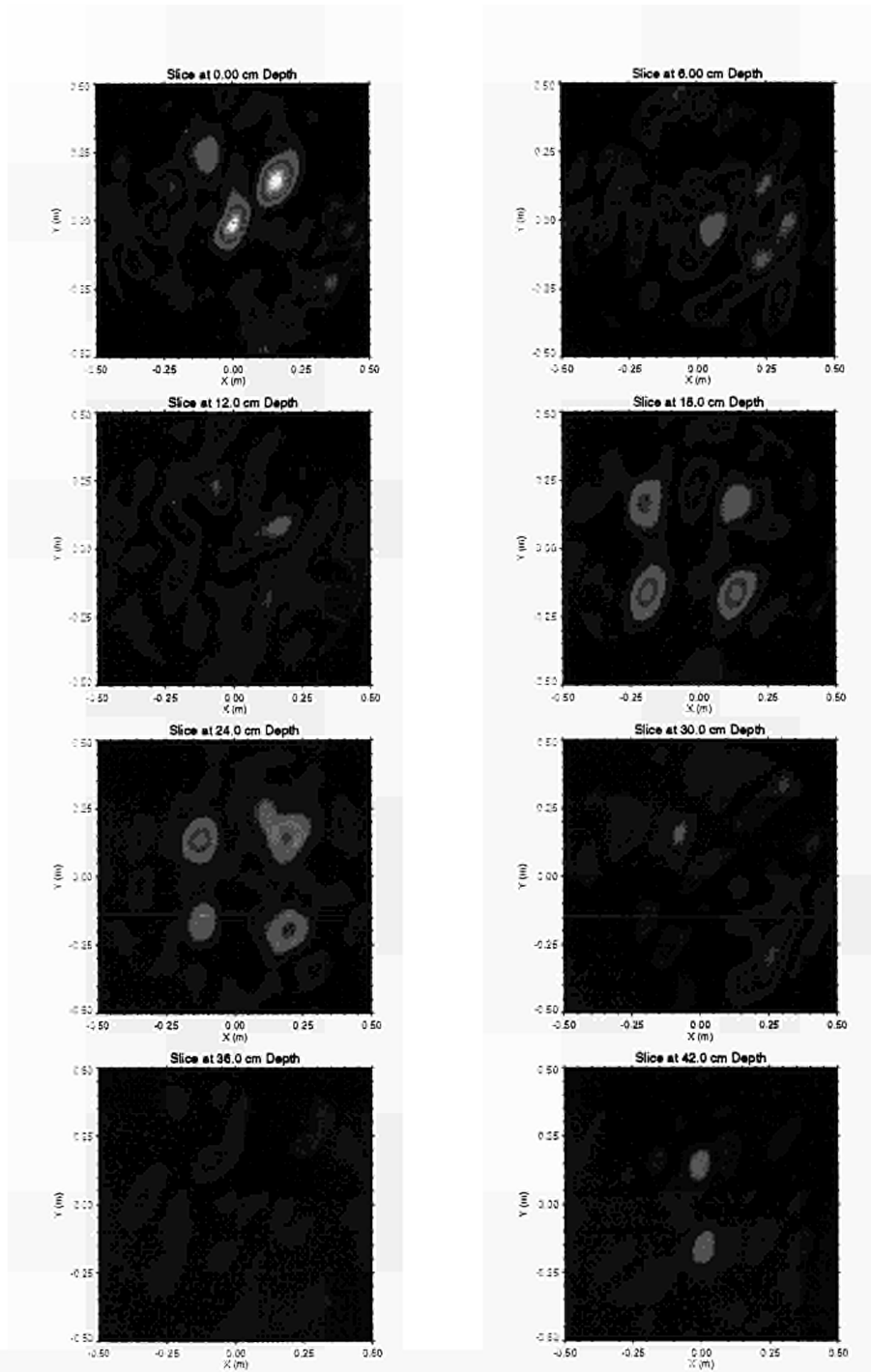


Figure 4: Horizontal slices from the 3-D ISAR image with the eight metallic spheres underground

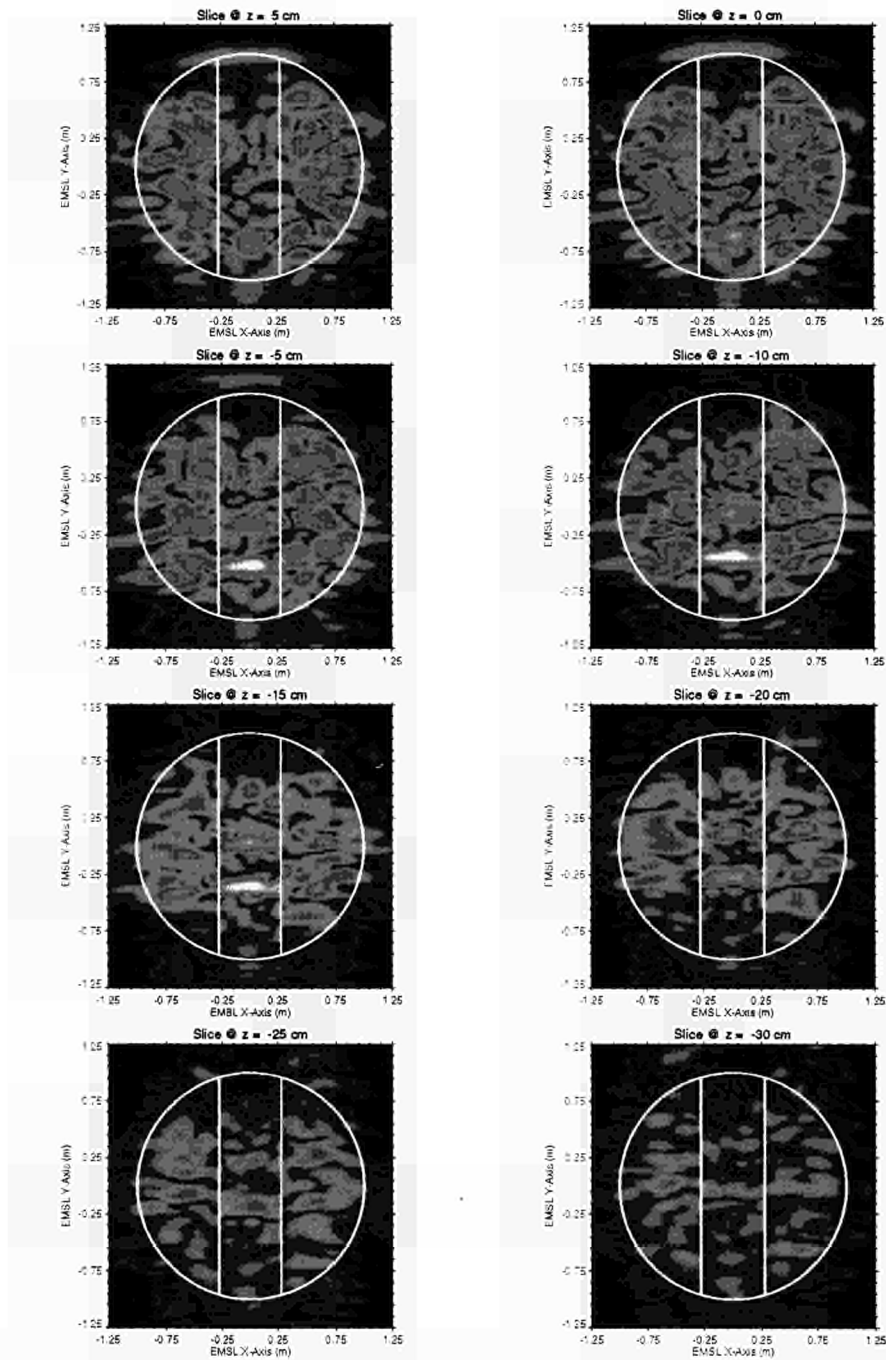


Figure 6: Horizontal slices from the 3-D ISAR image with the nine metallic dihedrals underground

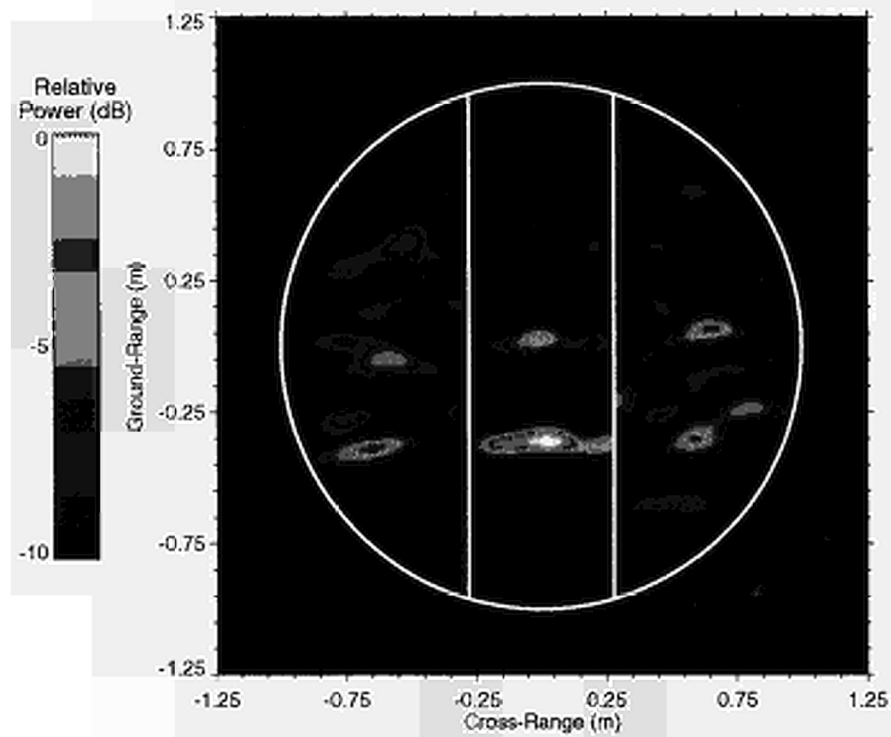


Figure 7: Horizontal slice at 15 cm depth showing the nine metallic dihedrals underground

THE ROCOCO PROJECT: A COOPERATION BETWEEN EMSL AND DAIMLER-BENZ

Hans RUDOLF
*Research Engineer, Signal Processing Group F3M/IV
Daimler-Benz AG, Research and Technology, Ulm, Germany*

Eggert OHLMER
*Scientific Referent, Head of EMSL Operation
Space Applications Institute, JRC Ispra, Italy*

ABSTRACT. RoCoCo is a cooperative study project between an industrial partner, -a research team from Daimler-Benz -, and the European Microwave Signature Laboratory. The aim was to measure radar backscatter from asphalt road surfaces in different ambient conditions in this laboratory. The experimental data are needed for the development of new technologies for improved safety systems in automobiles.

Introduction

RoCoCo stands for *Road Condition and Control*, a collaborative study project between the Daimler-Benz Research Centre at Ulm and the Space Applications Institute SAI of the Joint Research Center in Ispra. The study started in 1995 with the aim of determining the radar backscatter characteristics of typical asphalt road surfaces in well-defined ambient test conditions. Daimler-Benz will then use the data in its research projects addressing safety technology developments for automobiles. The SAI offers its expertise in radar signature research and the related research facility EMSL, the European Microwave Signature Laboratory.

1. The Industrial Partner

The industrial partner in the project is Daimler-Benz, with the Signal Processing Group of the Research Centre at Ulm. Current research comprises microelectronics, materials, production, energy and information technology. Products of information technology include not only signal processing tools and software but also electronic and microwave hardware.

Experts predict that tomorrow's automobile will contain more than 25 % of electronics, in terms of expenditures. Daimler-Benz is thus already investigating advanced millimetre-wave sensors for various car applications. For instance millimetre-wave devices for speed control, distance keeping, side-impact warning or road pricing could become standard automobile equipment in the near future. With technological developments these sensors will become consumer products. As a consequence a spin-off for other potential and current users of millimetre-wave equipment can be expected.

Within these development perspectives the Daimler-Benz Research Centre in Ulm partnered up with the SAI in Ispra to act jointly in related radar signature research projects such as the present RoCoCo study. This specifically addresses the risks encountered by automobiles driven on roads in adverse ambient conditions: aqua-planing, slipperiness due to rime or glazed frost are dangers all too familiar to drivers. In specific terms, if the actual frictional index between car tire and road surface could be known at each moment or even in advance to the driver on-road, measures could be designed to improve driving safety substantially.

2. The RoCoCo project

This project was inspired by current work by the Signal Processing Group to determine the friction behaviour of road surfaces by means of a polarimetric radar system. Suitable experimental data were needed to develop and validate a theoretical model of backscattering of asphalt surfaces. This data had to be obtained from precise radar measurements on road

automatic measurement operation feature and its technical expertise in radar target realisations offers this experimental condition. The facility can set up the required test conditions for the different road samples, including the techniques to create water and ice layers of determined thickness on the targets. It was important to obtain these test conditions in a defined and reproducible manner and that they remain stable for several days during the experiments.

The RoCoCo experiments were designed and performed at the EMSL in collaboration with their research counterparts from Daimler-Benz. A series of tests have been defined with comprehensive radar measurements in the EMSL facility on different types of realistic asphalt road targets. The surface roughness in combination with the ambient conditions seemed the most important parameter. The tests had therefore to simulate different road surface conditions reflecting typical weather: dry and wet asphalt, surfaces with water films of different thickness or with rime and ice layers.

Different radar systems had to be used with measurements in various sensor-target configurations. Here, frequency range and viewing angle are the main parameters for the intensity and polarisation behaviour of the backscatter. Bistatic backscatter measurements as well as tests with a mobile system moving over the road targets at simulated car speeds were included.

In view of the considerable efforts involved in this type of experiment and following a general policy of the EMSL, the tests were designed to provide, with the measurements, as much experimental information as possible on the research topic as a whole. Thus the experimental radar backscatter data of the road targets generated by the tests, for instance with respect to frequency, angular positions, bistatic aspects and such, covered broader areas than were actually needed for the industrial system at present under development. The EMSL experiments are considered to provide reference data for the topic under investigation, and as such are generated in comprehensive ranges and archived for future application needs.

3. Experimental Set-Up

3.1 ASPHALT ROAD TARGETS

Three road samples were investigated: the standard asphalt surface found, for example, on highways, a coarser and a finer grained asphalt. From these samples 17 cm thick road targets were built up as 2 x 2 metre square platforms. The targets must mimic as closely as possible realistic road conditions with respect to structure, compactness and surface. They were made by a road-building firm, using the same materials and procedures as for real roads.

The platforms have a cooling pipe system built into the bottom. The pipes are fed by a freezer unit with special cooling liquid at temperatures down to -40°C . This means the road samples can be cooled down to frost temperatures, for instance with stable -5°C on the surface. This provides controlled test conditions for rime deposits or ice layers on the surface. Water films, or even ice layers, are applied by spraying specific amounts of water onto the surface. A radiant heater is available to dry the road surface targets.

The road sample platforms were mounted on the target positioner of the EMSL facility for measurements in the absorber chamber, see **Figure 1**. For the outdoor tests with the mobile sensor arrangement they were put on the ground outside the facility.

3.2 RADAR INSTRUMENTATION

Two measurement systems were used for the tests in the EMSL dome: the standard microwave instrumentation of the facility and radar instrumentation from Daimler-Benz. Antennas of both systems were mounted together on the mobile antenna sled units. Using the sleds the different viewing angles to the target surface were then adjusted for the measurements. This way both antenna systems always had the same test configuration so the measurements are fully comparable.

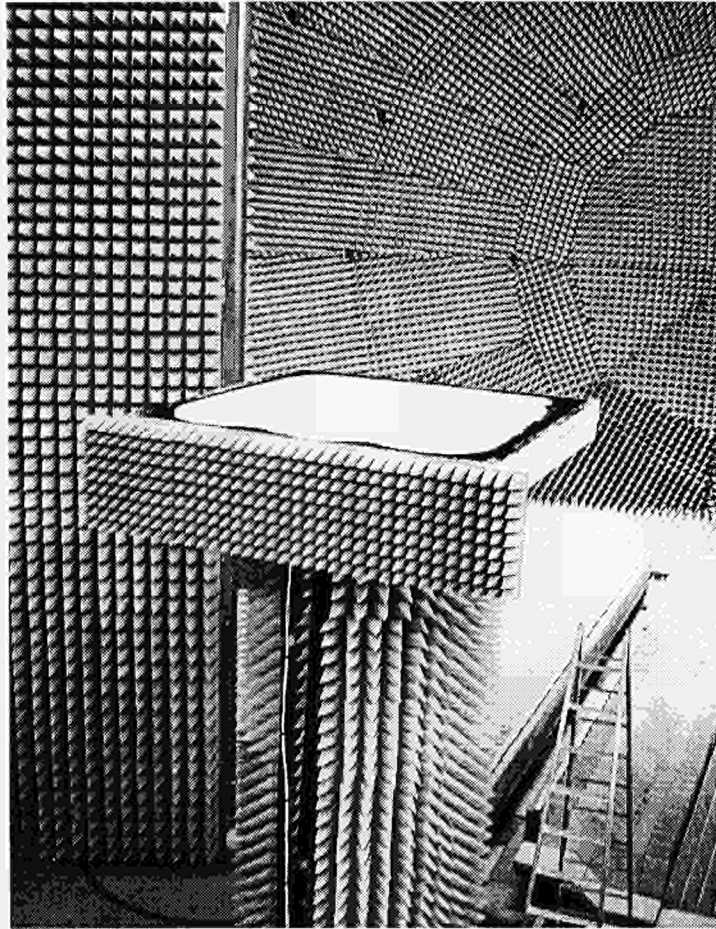


Figure 1. Road asphalt target mounted for the radar measurements in the EMSL. The road surface was prepared with a rime cover for this test.

The standard EMSL antenna units were used in the frequency range 20 to 24 GHz. They were operated in the continuous wave mode at stepped frequencies providing full-polarimetric measurements in the mono- and bistatic mode.

The Daimler-Benz radar system is based on a vector network analyzer and makes fully polarimetric and bistatic measurements in real time. It works in the millimetre wave range, i.e. at around 75 GHz, providing continuous wave or pulsed measurements. The basic frequencies generated by the synthesizer are quadrupled in the antenna front end. Broad-band antennas of the corrugated horn type with an aperture of 4 degrees cover the range from 70 to 80 GHz. A hardware range gate unit achieves a resolution up to 7 ns, or about 1 meter in range. By additional use of software gating, a maximum range resolution of 1.5 cm can be obtained. Another feature is the possibility of tuning for Doppler measurements up to velocities of 128 m/s, though this feature was not required for the RoCoCo study. This test equipment can be mounted in a van for measurements while driving. The complete system was controlled for the measurements through a UNIX workstation by means of a user-friendly interface guaranteeing consistent system settings, the synchronisation of all measurement activities and the data management.

3.3 MOVING SENSOR ARRANGEMENT

These measurements were made with different radar sensors for mobile applications. A sensor moving on a car over the road will "see" the road condition in the form of random signal

sequences. The relevant information must be derived on-line by an adaptive signal analysis program following stochastic parameter schemes identifying typical road conditions. Such analysis algorithms must be checked and validated with real signal data sequences measured in typical well-defined road conditions. An ideal test arrangement for this gave the RoCoCo asphalt targets, for which the radar backscatter behaviour has been determined precisely and in a variety of test conditions.

The test set-up in this case involved a special linear sled arrangement moving the sensors at certain typical car speeds over the road targets, see **Figure 2**. The road samples were placed on the ground outside the EMSL facility. The surface conditions of the asphalt targets were adjusted identically for both test series, those in the EMSL chamber and those outside.

4. Tests already completed

A preliminary series of measurements started at the end of 1995 gave initial promising radar results, showing that the conditioning techniques to adjust the road surface states for the test requirements were working as expected. The tests continued early in 1996 with systematic measurement sequences to investigate all the specified experimental parameter.

The radar measurements were made in the polarimetric mode at frequencies 20 - 24 GHz and in parallel in the W-band at 70 - 80 GHz. Two types of measurements were made:

- monostatic backscattering at 44 different incidence angles,
- quasi-specular bistatic scattering at five incidence angles: For each incidence the scattering was measured in five positions in a range of 15° around the specular reflection angle.

In all cases measurements were repeated with the road target turned at different azimuth aspect angles in order to generate a number of independent data samples.

The influence of the road roughness was investigated with the three different asphalt samples under dry surface conditions. The influence of the ambient condition was measured only with the 'standard' road sample. For these measurements the road target was prepared to obtain defined conditions like wet or humid (with or without water layer), or with rime or ice layers on the surface. Figure 3 shows an example of the target prepared with a rime cover.

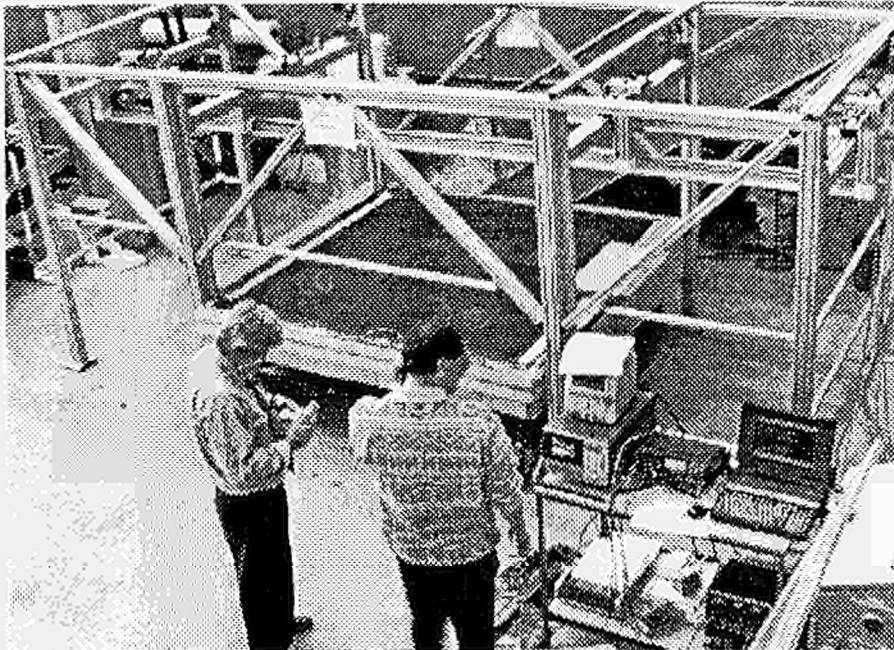


Figure 2. Test arrangement with mobile radar sensors for measurements on the road asphalt targets

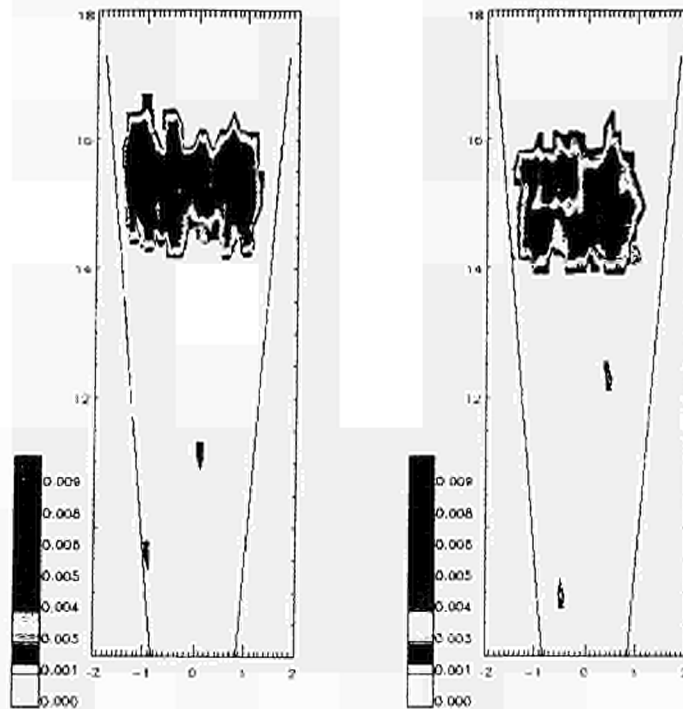


Figure 3. Radar backscatter from an asphalt road in different ambient conditions; imaging presentation of RCS data (76 GHz) measured with a dry (left) and icy (right) road target surface.

All these tests were completed by related calibration measurements for the radar instrumentation and for the 'empty room' influence of the measurement chamber. For EMSL tests it is standard practice to generate the experimental data in corrected and calibrated form (Nesti 1993). With the raw data these are kept available in the EMSL data archive.

5. Some Results

The radar data generated by the RoCoCo experiments is now being analysed by the research teams. The first results seem very promising. Of course, at the present stage and conditions only a few typical examples can be published.

Figure 3 shows radar cross section data (RCS) of the road surface in dry and icy situations with significant differences. Of course, this is not the type of presentation suitable for car driver on-road information. In a more detailed analysis Figure 4 shows some polarimetric properties from the same surface conditions.

These results suggest that classification of the different road situations, and therefore also monitoring is possible. Some typical and unequivocal recognition parameters are needed based on the radar data for each road situation. These parameters could eventually be used in the automobiles of the future to enhance road safety either by active control of the car electronics, as with ABS or ASD, or by passive driver assistance in the form of a warning system. Another application might be to improve driving comfort, for example by control of electronic suspension systems in relation to the road situation.

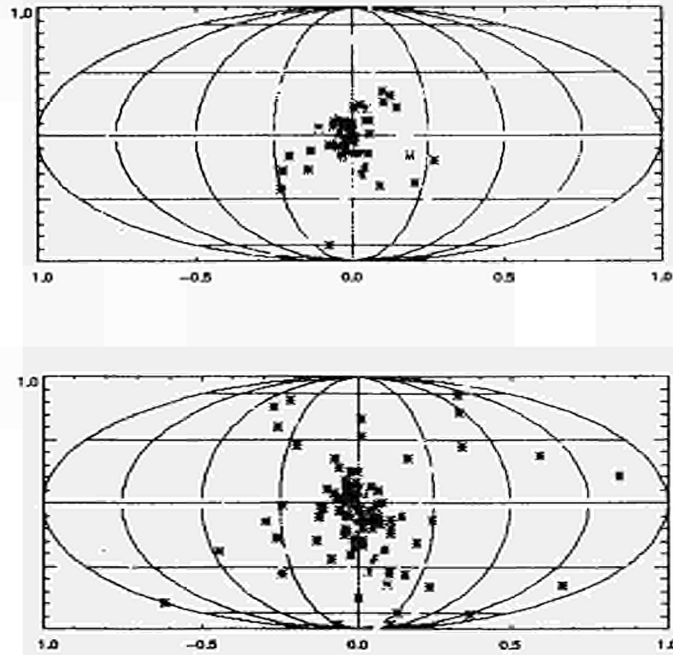


Figure 4. Polarimetric properties of radar backscatter data in Poincaré sphere presentation; same test conditions as in Figure 5 with a dry (above) and icy (below) road target surface.

6. Conclusion

The experimental part of the RoCoCo study was concluded in April 1996. The experimental data generated is now being analysed. The preliminary results are very encouraging and promising with respect to the objectives.

This cooperative study, drawing on the complementary skills of both research teams, has turned out to be very fruitful for both partners. Expertise gained from research in support of remote sensing applications could be advantageously inserted in industrial research for the development of new technologies, for instance in "car-of-tomorrow" projects.

References:

Nesti G. and E. Ohlmer, 1993, Il Laboratorio Europeo di Misure a Microonde, *Proceedings of 94a Riunione Annuale AEI*, Ancona/Italy

SAR FOCUSING AND INTERFEROMETRY EXPERIMENTS WITH EMSL DATA

P. Pasquali, C. Prati, F. Rocca

Dipartimento di Elettronica e Informazione del Politecnico di Milano - Italy

Abstract The anechoic chamber of the Electromagnetic Signature Lab (EMSL) at JRC has been utilized for validating SAR focusing algorithms and interferometry techniques and applications. Controlled experiments have been made with parameters, like bandwidth and antenna aperture, not yet available with airborne and satellite SAR systems. Moreover a tuned interferogram has been generated thus validating the wavenumber shift principle. Finally, an experiment on the use of multi-baseline SAR images for a 3-D target reconstruction has been carried out. The volume of the target has been reconstructed from the 3-D measures of its spectrum and has been visualized as horizontal slices at different depths.

1 Introduction

The availability of SAR data with large frequency, bandwidth and azimuth scan can be of great interest for testing the performance of different SAR focusing algorithms. SAR data with such parameters are not yet available in present airborne and satellite systems. However, indoor SAR imaging offers the possibility to carry out controlled experiments with higher flexibility and well known geometries. In this scenario, the possibility of controlled experiments offered by the EMSL anechoic chamber [1] plays a major role in studying present and future SAR interferometry applications. With such a purpose a number of SAR measurements have been carried out in the frequency band 8 – 12 GHz, and with an azimuth scan in the order of 20 degrees. This paper describes the results of different experiments specifically designed to validate the $\omega - k$ focusing technique (and its phase preserving capability) and interferometric applications.

2 The strip map focusing experiment

The first experiment has been devoted to the validation of focusing algorithms. Here, two identical spheres of diameter 30.5 cm have been placed parallel to the ground, aligned along the range direction at a relative distance of about 1 meter with their center of mass close to the center of the chamber ($\simeq 10$ meters from the antenna).

A strip map data set has been acquired by shifting the target in steps of 2cm along the azimuth direction with a 45 degrees looking angle and frequencies ranging from 8 to 12 GHz.

Raw data have been processed by means of the wave-domain processor ($\omega - k$) [2]. Due to the large relative bandwidth and antenna aperture, the required frequency resampling of the data (i.e. the Stolt interpolation) has been carried out without any approximation by using the Discrete Fourier Transform instead of the usual FFT algorithm. At the cost of a lower computation efficiency, DFT allows to compute the Fourier transform for all frequencies. The achieved resolution (3×4 cm) is comparable with the expected one. Raw

and focused images (with optimal parameters generated by autofocus) of the two spheres are shown in figures 1 and 2. A precise data focusing is fundamental to analyze the SAR interferometry results that will be shown in the following sections.

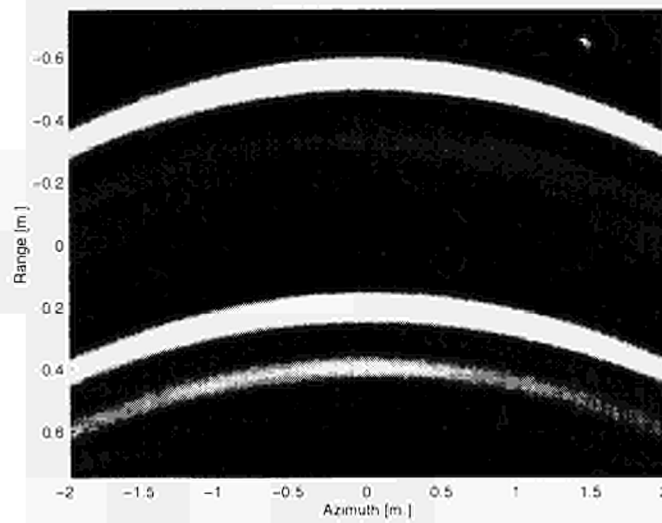


Figure 1: Range compressed images of the two metallic spheres. The gray scale is in dB from 0 (white) to -40 black.

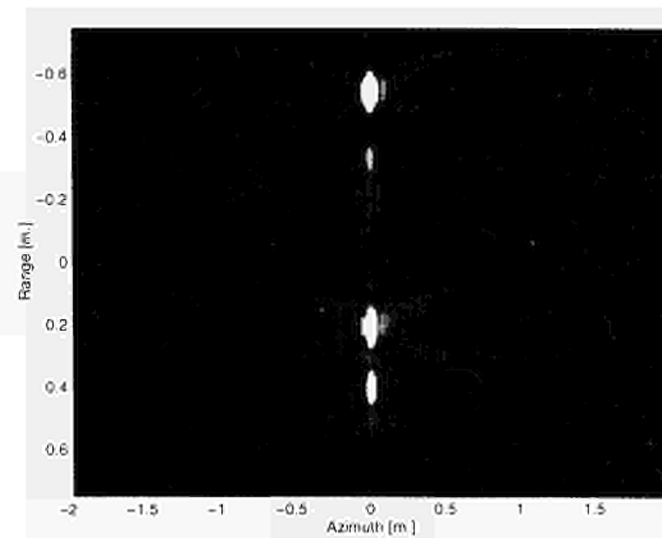


Figure 2: Azimuth focused images of the two spheres. Again the gray scale is in dB from 0 to -40.

3 The tuned SAR interferometry experiment

In [3] and [4], it has been shown that the spectra of two SAR images gathered from slightly different angles correspond to different bands of the ground reflectivity's spectrum. In general, an off-nadir angle difference $\Delta\theta$ generates a shift and a stretch of the imaged terrain spectra in the ground range direction. However, if the relative system bandwidth is small (as in most operative SAR systems), the stretch can be neglected and the following equation holds.

$$\Delta f = -\frac{f_o \Delta\theta}{\tan(\theta - \alpha)} \quad (1)$$

Here, θ is the off-nadir angle, α is the terrain slope in ground range and f_o the central radar frequency. Equation 1 does not state that by changing the off-nadir angle of the SAR survey the radar bandwidth is shifted by Δf . It just says that by changing the SAR off-nadir angle, the backscattered signal contains different spectral components of the ground reflectivity spectrum. In other words, if we look at the signals received by two SARs separated by an angle $\Delta\theta$, equation 1 states that the same spectral components of the first signal are found in the second spectrum shifted by Δf . Thus, a different band of the ground reflectivity spectrum is recovered by changing the off-nadir angle of the SAR survey. As a consequence of the finite system bandwidth, part of the spectrum of the two surveys (i.e. a band $|\Delta f|$) will be uncorrelated and phase noise would be added to the fringes (baseline decorrelation). On the other hand, as suggested by equation 1, the equivalent frequency shift induced by the off-nadir angle change $\Delta\theta$ could be compensated by shifting the transmitted central frequency during the second survey. In this way, the so called baseline decorrelation could be avoided at least for a chosen constant terrain slope. Coming to our experiment, we used a square target (2×2 m), divided into 5 stripes as shown in figure 3.

The four vertical stripes were filled with metallic spheres with different diameters (2.1, 3.5, 5 and 6.8 mm.). The horizontal stripe in far range was filled with gravel with average diameter of about 1cm (the use of different scatterers will be clear in the next section on volumetric effects). Two strip map data sets have been acquired by shifting the target in steps of 2cm along the azimuth direction with 46 (image 1) and 48 degrees (image 2) off-nadir angles and frequencies ranging from 8 to 12 GHz in steps of 5MHz. After wave

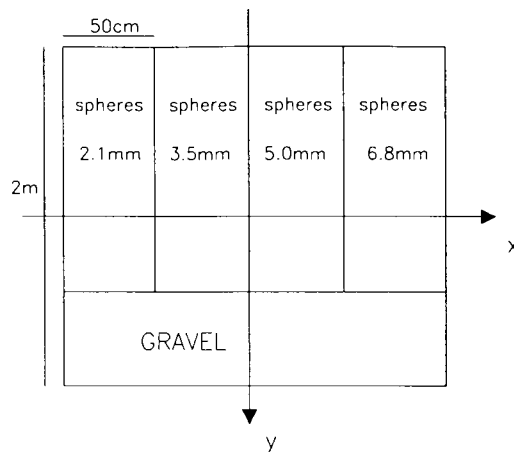


Figure 3: Target used for the SAR interferometry experiment.

equation focusing (see one of the detected images in figure 4), fringes have been generated by means of the usual complex cross-multiplication of the images. They are shown in figure 5.

Even if the fringes look noisy, the measured coherence is not so low as one would expect. The reason is that detected images show many values close to zero. Here the system noise (thermal) is dominant and the interferometric phase is random. In the coherence computation, however, complex numbers are averaged and small amplitudes do not affect greatly the result. As an example, the coherence computed in the far range stripe (horizontal) of the target is $\gamma = 0.867$. It should be noted that the expected geometric decorrelation in our case would give an higher coherence value ($\gamma = 0.935$). The main reason of this discrepancy is the volumetric scattering contribution to the coherence loss that is proportional to the spheres diameter. Nonetheless, following the spectral shift idea, the coherence is expected to increase if the off-nadir angle change is compensated by tuning the radar frequency to

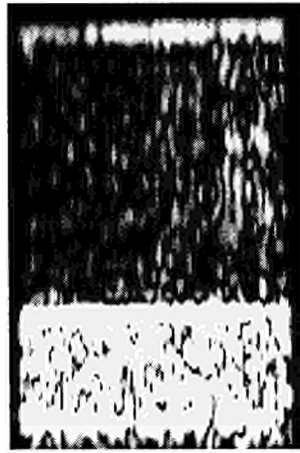


Figure 4: Detected image of the target shown in 3.

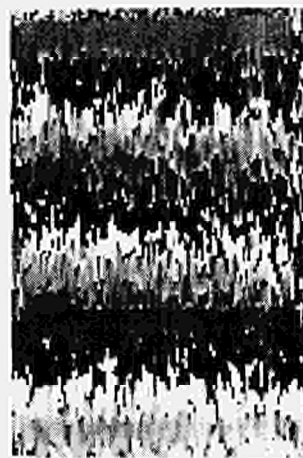


Figure 5: Interferometric phase of the target shown in 3 imaged with an angular separation of $\Delta\theta = 2^\circ$.

$f_o + \Delta f$. However, the small bandwidth approximation is not valid in the case of EMSL data and the spectral stretch cannot be ignored. As an example, the spectral shift computed for $\delta\theta = 2$ degrees and $\theta = 47$ degrees is about -260MHz and -390MHz in correspondence to the lower (8GHz) and upper (12GHz) limits of the system band. Thus, a third strip map data set (image 3) has been acquired again at 48 degrees, but with frequencies ranging from 7.74 to 11.61 GHz in steps of 4.83735MHz. As shown in figure 6 the quality of the fringes generated from images 1 and 3 does not look so different from that shown in figure 5 (apart from the removal of the flat terrain component). However, coherence measured in the far range stripe (horizontal) is now $\gamma = 0.893$ (not 1 due to volumetric scattering effects).

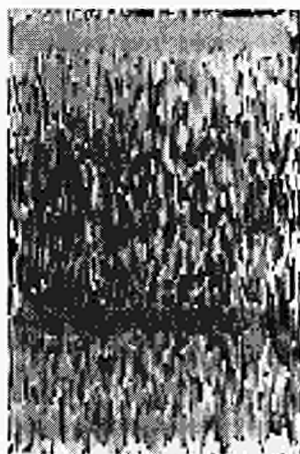


Figure 6: Interferometric fringes the target shown in 3 generated with images tuned to the computed wavenumber shift.

4 Volumetric scattering

Up to now, we have considered only surface scattering, neglecting the effect of volume scattering [6, 7]. However, when backscattering comes from targets with different elevation z within the resolution cell, volume effects cannot be ignored. This case is shown in figure 7: the scatterers are contained in a box with dimensions $(\Delta y, \Delta z)$, (the problem can be assumed to be invariant with respect to the azimuth direction). The radar return is function of the complex reflectivity $a(y, z)$, the radio frequency $\omega = 2\pi f$, and the off-nadir angle, θ :

$$A(\omega, \theta) = \iint a(y, z) \cdot \exp\left(-j\frac{2\omega}{c}(y \sin \theta - z \cos \theta)\right) dydz \quad (2)$$

We consider the medium as semitransparent, in the usual first Born approximation, so that the scattered signal is a linear superposition. Wavenumbers in ground range k_y and in elevation too k_z have the following form:

$$\begin{aligned} |k_y| &= \frac{2\omega}{c} \sin \theta \\ |k_z| &= \frac{2\omega}{c} \cos \theta \end{aligned} \quad (3)$$

- stripe 2 (3.5mm): measured $\gamma = 0.9183$
- stripe 3 (5mm): measured $\gamma = 0.8206$
- stripe 4 (6.8mm): measured $\gamma = 0.7756$

Notice that the measured coherence decreases for larger spheres size. However, it is much lower than that expected from the model. The vertical dispersions Δz that would explain the measured coherences (through equation 5) are 3.2, 3.6, 5 and 6cm for the four stripes. A possible explanation of these very first results is that spheres and gravel are not at a constant elevation within the region used for coherence estimation thus increasing the actual vertical dimension of the box. Another possibility is that multiple reflections among spheres amplify the volumetric scattering effects. Moreover, it is expected that multiple reflections increase with the spheres size. If this is the case, one would expect that images auto-correlation (in range) shows larger dispersion around the peak for larger spheres size. Images auto-correlation ('biased') of the first (i.e. diameter: 2.1mm) and third (i.e. diameter: 5.0mm) stripes are shown in figure 8. Those plots confirm the hypothesis, at least from a qualitative point of view.

5 The 3-D reconstruction experiment

In usual strip map SAR systems the target spectrum is regularly sampled in two dimensions: azimuth and slant range wavenumbers. In order to get 3-D images the missing dimension is found in the baseline of interferometric SAR images. An experiment on the use of multi-baseline SAR images for a 3-D target reconstruction has been carried out.

Strip map broad side SAR images are regularly sampled in two dimensions: azimuth and slant range (i.e. time). Slant range sampling generates a well known unwanted geometric deformation of the observed 3-D scene (i.e. foreshortening and layover). Moreover, since microwaves penetrate the target (especially when low frequencies as P band are used), a SAR image is the representation of a backscattering volume rather than a backscattering surface (as in optical remote sensing systems). Thus, a more realistic picture of the scene imaged by SAR is a volume of scatterers that cluster along a surface in the 3-D space (i.e. the topography). The actual situation is sketched in figure 9. There, the azimuth dimension

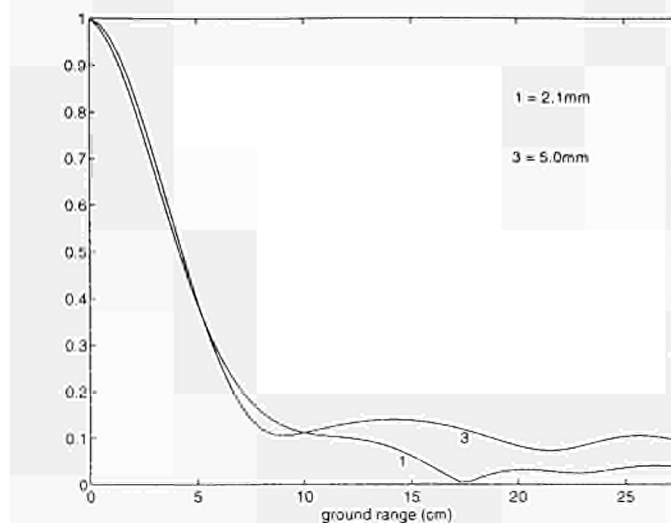


Figure 8: Auto-correlations of the stripes 1 (2.1mm) and 3 (5.0mm) shown in figure 3.

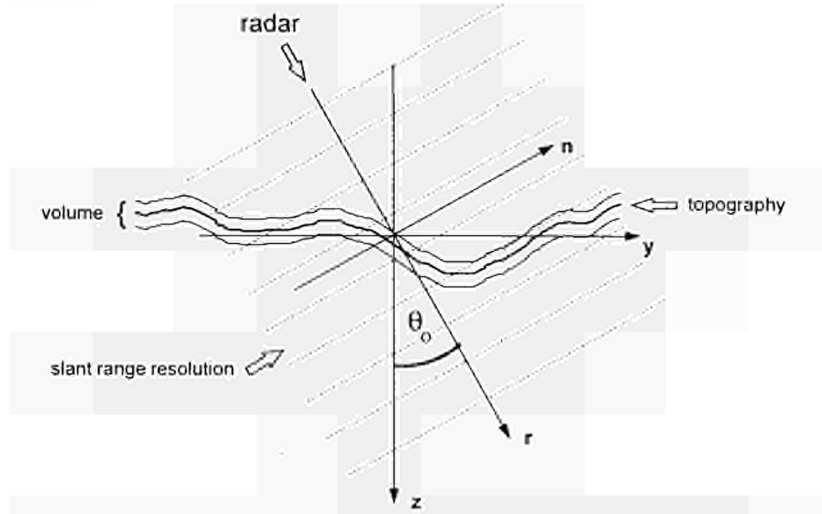


Figure 9: Description of the target imaged by a SAR system.

is orthogonal to the sheet. It will be neglected in the following discussion since the problem can be considered invariant along that dimension with no loss of generality. At a given azimuth, the target can be described in 2-D with different coordinates systems including ground range y and elevation z (independent of the SAR looking angle θ), and slant range r and its normal n (dependent on the SAR looking angle).

5.1 The measured target spectrum

The received SAR signal $y(t)$ given the Fourier transforms of the transmitted signal $X(\omega)$ and of the target reflectivity $V(k_r, k_n)$ has the following expression [8].

$$y(t) = \frac{1}{2\pi} \int_{\omega_0 - W/2}^{\omega_0 + W/2} X(\omega) V\left(\frac{2\omega}{c}, 0\right) e^{j\omega t} d\omega \quad (6)$$

The SAR central frequency is indicated with ω_0 and its bandwidth with W . As a first approximation, the transmitted spectrum $X(\omega)$ can be neglected since it is almost constant within the system bandwidth. Equation 6 suggests that the measured band of the 2-D target spectrum is a part of the k_r axis (i.e. $k_n = 0$) as shown in figure 10. Here the ground range and elevation wavenumber axes (k_y and k_z) are used as the reference system since they do not depend on the SAR looking angle. Let us now suppose to get more SAR images of the same target with different looking angles within the range $\theta_0 - \frac{\Delta\theta}{2}$ and $\theta_0 + \frac{\Delta\theta}{2}$. The measured target spectrum is shown in figure 11. From that figure it can be seen that a 2-D band of the target spectrum is now recovered. Thus both target components along the slant range r and its normal n can be recovered by means of a 2-D inverse Fourier transform.

5.2 Resolution and alias

The measured bandwidth W_n along the normal wavenumber axis k_n depends on the largest angle variation $\Delta\theta$.

$$W_n = \omega_0 \Delta\theta \quad (7)$$

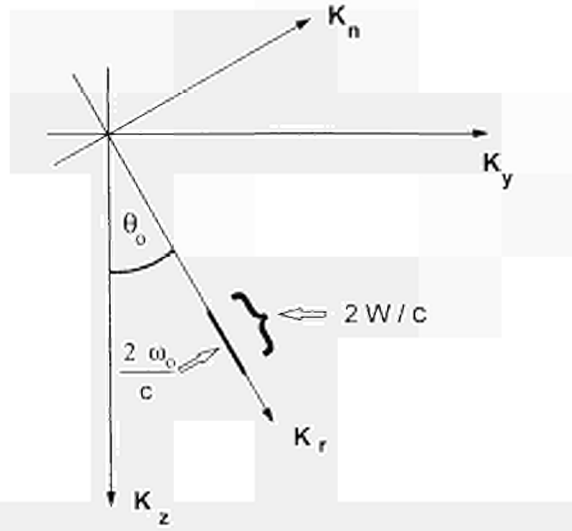


Figure 10: Measured target spectrum by a SAR with looking angle θ_0 , transmitted frequency ω_0 and bandwidth W . The imaged part of the 2-D target spectrum is shown with a bold segment.

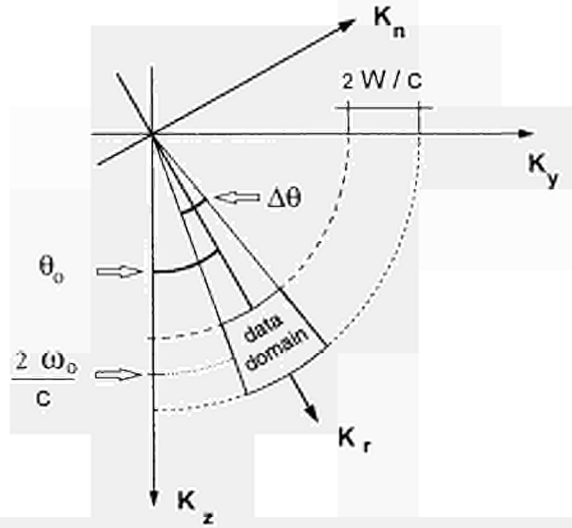


Figure 11: Multiple angles SAR surveys. The imaged target spectrum is shown in gray.

The spatial resolution in the normal direction has the following expression:

$$\rho_n = \frac{c}{2W_n} \quad (8)$$

As far as the spatial aliasing is concerned, it is well known that, whenever a signal is sampled in one domain (e.g. time), the signal in the conjugate domain (e.g. frequency) is periodic with a period proportional to the inverse of the sampling interval. In our case, the target spectrum is sampled both along the k_r and k_n axes. However an important difference between the two axes should be emphasized. As a matter of fact, the received SAR signal is down converted, low-pass filtered and sampled in slant range (i.e. obviously there is no alias in the slant range domain), thus generating a periodic Fourier transform with no alias

(at least in principle). On the other hand the SAR signal is directly sampled in the normal wavenumber domain (i.e. angular sampling) thus generating a periodic signal in the space domain with possible alias.

We suppose that the angular sampling is regular from $\theta_o - \frac{\Delta\theta}{2}$ to $\theta_o + \frac{\Delta\theta}{2}$ with a $\delta\theta$ sampling interval (equivalent to a $\delta k_n = 2\omega_o\delta\theta/c$ sampling interval in the k_n wavenumber domain). The spatial period Δn of the reconstructed signal along the normal axis "n" has the following expression:

$$\Delta n = \frac{\pi c}{\omega_o \delta\theta} = \frac{\lambda}{2\delta\theta} \quad (9)$$

Thus, the target dimension along the normal axis should be smaller than Δn in order to avoid spatial aliasing.

5.3 EMSL SAR images

In the EMSL experiment 8 strip map SAR images have been generated with different incident angles from 41.5 to 48.5 degrees. A 4GHz signal bandwidth centered around 10GHz has been used. A two layers target has been generated with a "semitransparent" upper layer formed by several stripes of plumb spheres along range at different spacing and a bottom layer formed by several stripes of plumb spheres along range. The vertical separation of the layers is about 7cm. A single SAR image of the target is shown in figure 12.

The 3-D radar image of the target reconstructed from the multibaseline data set is presented as horizontal slices of the target at different depths. A few of them are shown in figures 13, 14 and 15. From those slices it can be seen that the upper layer of the target (figure 13 right) has been clearly isolated from the rest of the volume as well as the dielectric edges of the target (figure 14 left) that lie at the lower layer level. The resolution and the maximum depth that can be explored without ambiguity can be derived from equations 8 and 9 respectively. In our case a vertical resolution of about 8.5cm and an ambiguity of 60cm is obtained as expected; the horizontal resolution being 3×5 cm. Multiple reflections within the metallic spheres appear as volumetric contribution.

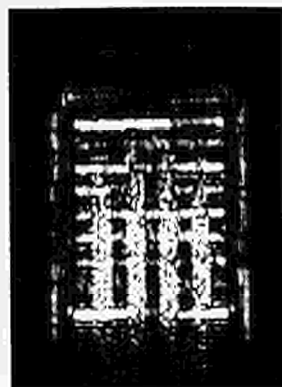


Figure 12: Detected SAR image of the two layers target.

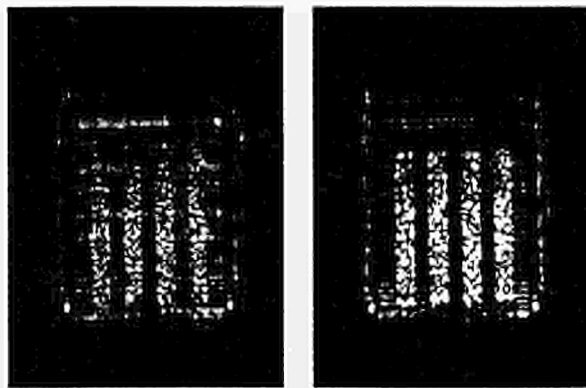


Figure 13: Detected SAR image of the two layers target: slices at -50cm (left) and -53cm (right) from the center of the chamber.

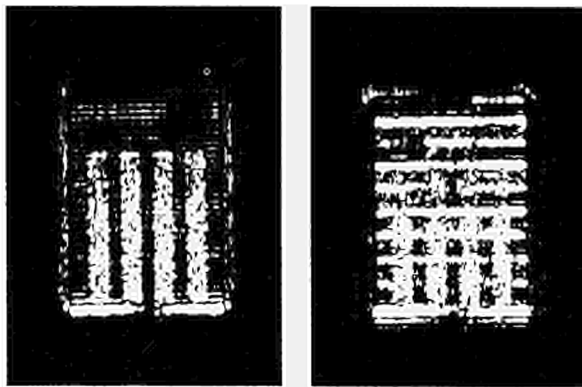


Figure 14: Detected SAR image of the two layers target: slice at -58cm (left) and -65cm (right) from the center of the chamber.

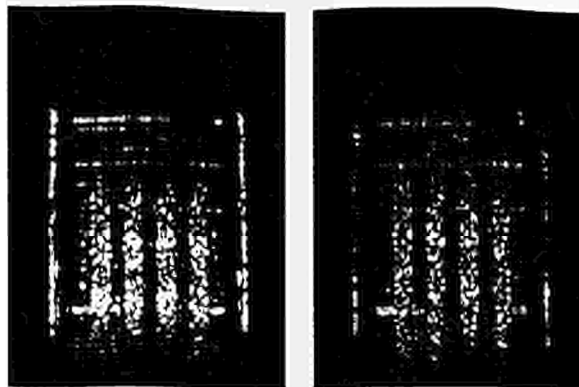


Figure 15: Detected SAR image of the two layers target: slice at -80cm (left) and -95cm (right) from the center of the chamber.

6 Conclusions

Strip map SAR data generated in the JRC-EMSL anechoic chamber have been used to check the possibility of exploiting the chamber for SAR interferometry studies. The results presented here show that the system can be used for interferogram generation. However, due to the different scale with respect to satellite and airborne SAR systems (e.g. in the shown experiment the resolution cell has the wavelength dimension), the usual geometrical optic approximation should be verified and new targets should be studied. On the other hand, EMSL is an unique tool to check new ideas since it allows to generate data in a large variety of geometries and antennas configuration.

References

- [1] A. J. Sieber, 1993, *The European Microwave Signature Laboratory*, EARSel Advances in Remote Sensing, Vol. 2, No. 1, January 1993, pp. 195-204.
- [2] C. Cafforio, C. Prati, F. Rocca, 1991, *SAR data focusing using seismic migration techniques*, IEEE Transactions on AES, Vol.27-2, pp.194-207.
- [3] C. Prati, F. Rocca, 1993, *Improving slant range resolution of stationary objects with multiple SAR surveys*, IEEE Transactions on AES, Vol. 29, No.1, 135-144
- [4] C. Prati, F. Rocca, *Range resolution enhancement with multiple SAR surveys combination*, Proceedings of IGARSS'92, Houston, May 1992.
- [5] F. Gatelli, A. Monti Guarnieri, F. Parizzi, P. Pasquali, C. Prati, F. Rocca, *The wavenumber shift in SAR interferometry*, IEEE Transactions on Geoscience and Remote Sensing, Vol. 32 , No 4, July 1994, pp.855-865.
- [6] E. Rodriguez, J.M. Martin, 1992, *Theory and design of interferometric synthetic aperture radars*, IEE Proceedings-F, Vol.139, No.2, pp.147-159.
- [7] P. Piau, J-C. Cael, M. Deschaux, A. Lopes, *Analysis of the resolution of multi temporal SAR systems*, Proceedings of IGARSS'93, Tokyo, August 1993, pp. 1196-1199.
- [8] P. Pasquali, C. Prati, F. Rocca, M. Seymour, J. Fortuny, E. Ohlmer, A. Sieber *A 3-D SAR experiment with EMSL data*, IGARSS'95, Firenze, pp.784-786.

LABORATORY EXPERIMENTS FOR THE INTERPRETATION OF PHASE SHIFT IN SAR INTERFEROGRAMS

Jean-Paul Rudant 1, Ali Bédidi 2, Rodolphe Calonne 2, Didier Massonnet 3, Giuseppe Nesti 4, Dario Tarchi 4.

1- UMLV & UPMC, tel: 33 1 44275087, fax: 33 1 44275085, Email: jpr @ Igs.jussieu.fr

2- UMV (Université de Marne La Vallée)

3- CNES, OTIS, 18 ave Edouard Belin, Toulouse

4- EMSL / SAI / JRC Ispra, Italy

Abstract:

Purpose: Interpretation of SAR interferograms (ERS1) in the light of phase shift laboratory measurements obtained as a result of moisture changes.

Results: We show that surface phase changes can be a contribution of both geometric and dielectric effects. The geometric effect result of soil swelling or settling. In our experiments, the dielectric effect is always equivalent to a subsidence when moisture increases and we interpret particular observation made on interferograms as a swelling of the most humid low area.

I. INTRODUCTION

Interferometric data (amplitude, coherence, phase difference) may be used for general or thematic cartographic purposes. They provide information on surface state and surface changes that occur between different dates of view. Coherence and phase difference images bring on these points original information that usually used amplitude images do not necessary contain (change of superficial geometry at the wavelength scale, phase effects of dielectric origin, measure of weak amplitude subsidence of mining exploitation, etc ..). In particular, rotations of phase observed in the interferograms take their origin all both in the displacement of the surface and in changes of dielectric properties that occur between different dates of view.

In this study, we attempt to evaluate the various contributions by confronting measures of phase rotation undertaken in the laboratory to interpretations of interferograms obtained on the globally stable site of Naizin in Brittany.

II. TEST SITE

The **test site** is the Naizin area in South Brittany, France (size 50km * 50km, Lat 48°N Long 3°W). Present day, the Naizin area is aseismic, without active deformation, in a standard agricultural area.

Fig 1 give also the rain periods over the Naizin basin situated in centre of the study area. The distribution of the rain events is not exactly know for the entire test site and it is expected that the Naizin basin is representative of the entire test site. This hypothesis seems reasonable for this kind of climate, devoided of local microclimate.

III. INSAR PRODUCTS

The **ERS 1 images used** were acquired during phase B (3 day repeat orbit) during February and March 1992 from ascending orbits. Out of 12 available images, 6 are in interferometric conditions. The corresponding acquisition dates are the following: 6, 9, 12, 15 February, 13 and 16 March, in a winter period where there is no variation in vegetal cover.

For each pair, we have two amplitude images, a coherence image and a phase difference image. All these products were corrected for the effects of distance and of known relief (ref 1).

Sign convention for phase differences:

The difference provided is algebraic, coded in 8 bits. The interval (0..255) corresponds to a complete 360° phase rotation and the result of the processing in CNES is given by:

$$(3.1) \quad \text{DIF-PHA1}_2 = ((2 / \lambda_0) * (\text{optical path 2} - \text{optical path 1}) * 256) + 128 + \\ (\varphi_1 - \varphi_2)_{\text{reflection}} * 256 / 360 + \text{Geometric corrections}) \quad \underline{\text{all modulo 256}}$$

where **1** indicate the master image and **2** the slave one.

The optical path is a one way antenna to target journey, λ_0 the wavelength in vacuum, φ the phase effect introduced by ground reflection.

The purpose of the geometric corrections is to remove all the predictable effects on the phase (i.e. topography and orbits) from the interferogram.

The choice of $(\varphi_1 - \varphi_2)$ follows from the use of the $e^{j\omega t}$ convention in the formula for a progressive wave:

$$e^{j(\omega t - \mathbf{k} \cdot \mathbf{r} + \varphi)}, \quad \text{with } \mathbf{k} = (2\pi/\lambda_0) * n * \mathbf{u} \quad (3.2)$$

where n is the optical index (complex value) and \mathbf{u} unitar vector in propagation direction.

It results from (3.1) and (3.2) that, with this convention, a negative φ is equivalent to an increasing of the optical path. An area raised by a few mm between the two image acquisitions, for example, would look darker than its surroundings on the phase image (for black and white phase scale).

IV. INTERPRETATIONS OF THE PHASE IMAGES

In summary, the phase image would be completely uniform if the following conditions were fulfilled:

- exact geometric corrections,
- the atmospheres at the two image acquisition dates have no propagation inhomogeneities (they need not be identical since the differences are to within a constant),
- surface conditions unchanged or subject to a uniform movement or dielectric change.

In practice, the phase difference images show effects with different origins, related either to the preprocessing, or to changes in the conditions of the surface and the atmosphere.

Artefacts related to the precision of the DEM used

The correction performed to bring the phase differences to altitude zero takes into account the altitude provided by the DEM used. The imprecisions of the DEM have an impact on the values of the unwrapped phase according to the following algebraic relationship:

$$\text{Signed phase error} / 360 = - \text{DEM error} / H_a \quad (4.1)$$

where H_a represents ambiguity in altitude .

This results in certain systematic artefacts, in particular for the low points, since the resampling of the DEM used at 40 m smoothes the thalwegs and makes them seem higher than they really are. An example of the preceding phenomenon is shown in **Fig 2** for phase image PHA-10, corresponding to an altitude of ambiguity of + 21 meters. The lowest points in the network stand out in several places by a negative contrast that corresponds to an error in the DEM that is positive by several meters for the thalwegs.

Modifications of atmospheric states, dielectric changes in surface states, global displacements

The corresponding effects do not depend on the altitude ambiguity.

Atmospheric effects are linked with the variability of temperature, pressure and humidity in the air, and dielectric effects are linked with humidity, temperature of the soil and its vegetal cover.

?A vertical surface displacement $+d$ will induce a negative change in phase that is inversely proportional to the wavelength used, equal to

- $360 * 2 * d * \cos(\alpha) / \lambda$ where α is the beam incidence angle.

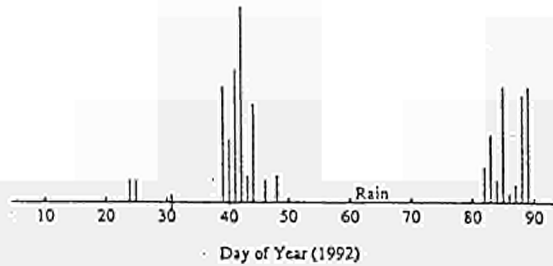


Fig 1: Rainy periods over the Naizin basin in February-March 1992 .

day 37, 6 February; day 40, 9 February
 day 43, 12 February; day 46, 15 February
 day 73, 13 March; day 76, 16 March

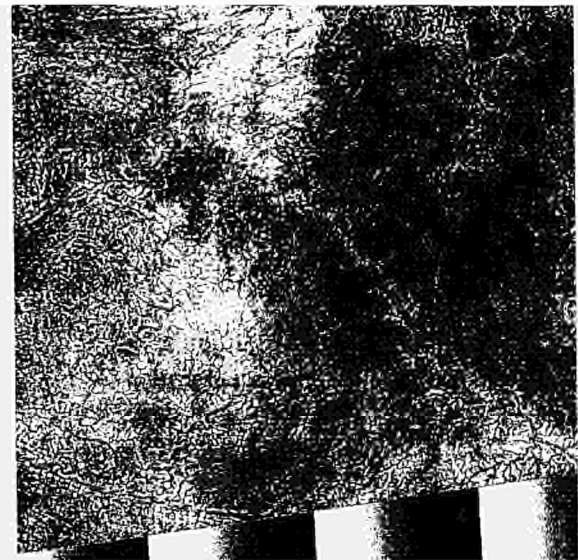
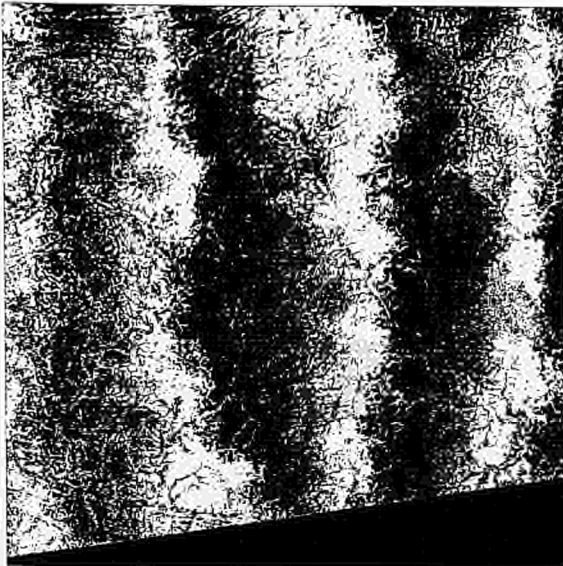
On the interferograms considered here several remarkable effects can be noted:

1- A general variability of 30-40° amplitude, which is neither systematic nor structured either by the relief or by man-made structures (fields, networks, urban areas), typically extending around 10 km, seems to be due to atmospheric effects (for example Fig 2). This type of effect is found on all the images with variable amplitudes.

2- Structured phase changes highlighting certain fields, in particular when the humidity conditions have changed between two acquisitions. (Fig 3).

When the contrast in humidity conditions is smaller (dry period or uniformly wet period), the phase change associated with the fields disappears (see for example Fig 2).

There may be various reasons for such positive or negative differentiation between the fields and their environment:



Figs 2: Phase differences obtained for an altitude of ambiguity of +21m, before and after unwrapping and after a simple model. Before unwrapping, a poor estimation of the altitude of ambiguity provoked fringes parallel to the satellite's direction of motion. The hydrographical network correspond to a negative contrast since, because of the smoothing performed on the DEM, the thalwegs appear higher than they actually are and the phase correction due to the relief is too large. The thalwegs would correspond to a positive contrast for a negative altitude of ambiguity.

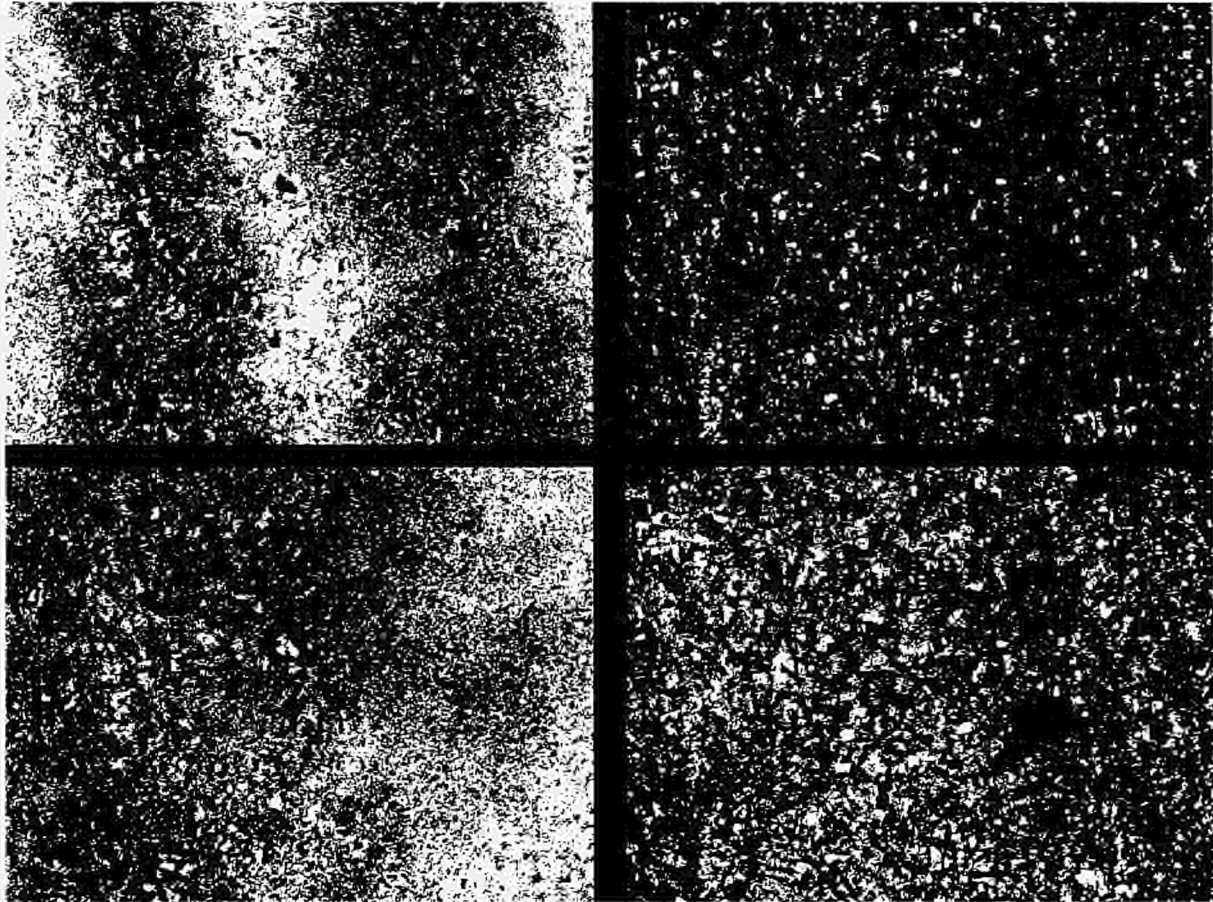


Figure 3 : Specific effects due to the presence of fields

Zoom (30km*20km) on phase difference image PHA-2 and amplitude images (6 and 12 February,). Phase is given before (1) and after (2) unwrapping, the geometric structures corresponding to the fields are very clear. These effects are more tenuous in the absence of a contrast in humidity. Bare rough soils are visible on the amplitude images, (3) 6 february and (4) 12 february. No important specific phase shifts are associated to this bare surface.

- a uniform elevation of the backscattering surface that leads to a shortening of the optical path and therefore a negative phase change (darker area).

- an increase in the mean value of the dielectric constant of the vegetation due to humidification, leading to a variation in the optical path and to a positive phase change if the dominant contribution in backscattering is given by the reflexion on the ground. Note that it is unlikely that cutting vegetation would increase the path, because this would make the speckle and the phases incoherent, since the basic reflectors would have changed.

Also note that fields probably corresponding to very rough bare soils, wich are characterized by their high radiometry (Fig 3), do not have a specific signature in the interferograms. The contrasts in phase with their environment are in general lower than 10° .

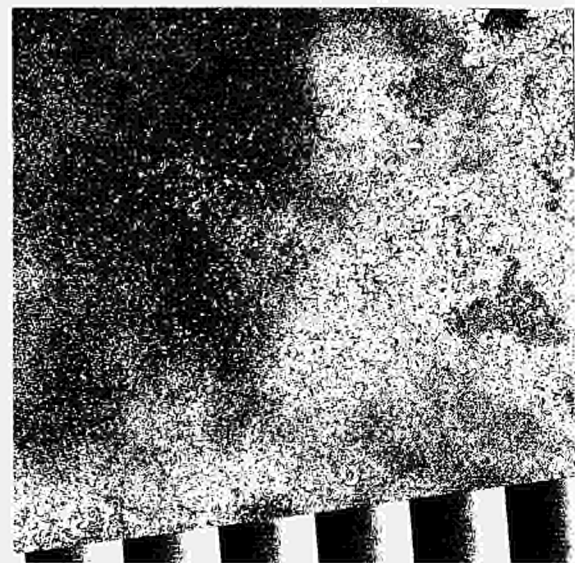
Note that for all the fields mentioned above, the phase noise is low and the coherence level high.

3- Phase changes on a scale of several kilometers correlated with the general shape of the observed relief when the climatic conditions change from a dry period to a wet one (see fig 1 for rainy events).

Comparing the digital terrain model with the unwrapped phases PHA-1 and PHA-2 (6 (dry) and 9 (wet) February on the one hand and 6 and 12 February on the other) (Figs 4, 5) shows that



Figure 4: Representation in grey levels of the topography; lower values at 20 meters (dark) and highest values at 309 meters (white).



Figures 5a and 5b: Phase changes structured by the hydrographical network.

Fig. 5a: Phase image PHA-1 (6 and 9 February) shows the phase changes structured by the network in the center and to the east (The darkening is equivalent to a reduction in the antenna to ground distance). The fact that such structuring is not found on all the data and is not linked to the altitude of ambiguity excludes an artefact related to DEM imprecisions.

Fig. 5b: Phase image PHA-2 (6 and 12 February) shows, less clearly, the same type of effects that are seen in Fig. 5a.

the low areas react in a differentiated way, with phase difference DIFF-PHA, (see equation 3.1) of the order of (-80°), with respect to their surroundings (equivalent to moving the backscattering surface closer). This effect is equivalent to a reduction in the optical path, and the possible origins of the phenomenon are: dielectric effect related to humidification (phase rotation equivalent to a reduction in the optical path between the second and the first date, with $\varphi_2 - \varphi_1 = +80^\circ$ (eq 3.1), ground swelling, localized atmospheric effect. Experimental study on the Naizin site (ref 2) shows that the level of humidity depends on the relative elevation with respect to the river and that the contrasts between low and high areas is larger for a wet period than for a dry period. It thus seems plausible that for the second date used for interferograms PHA1 and PHA2, the low points in the soil have a higher humidity level, and in consequence the air also.

V. LABORATORY EXPERIMENTS

First, let consider what phase rotation the Fresnel formula gives at normal incidence as result of the humidification of a flat homogeneous soil.

5.1. Phase rotation in Fresnel reflection coefficient

The Fresnel reflection coefficient for an incident wave normal to the interface plane of two homogeneous media is given by:

$$Re^{i\varphi} = (1 - nr) / (1 + nr)$$

where nr is the relative index of the 2nd medium with respect to the first and φ is the phase rotation associated with the reflection of the wave. This formula can be used for a greatly simplified initial quantitative evaluation of the effect of dielectric changes. We show in (ref 3) that the variation is always bounded to 90° and for typical values of dielectric constant is lower than 30° .

The evolution of the real and imaginary values of the dielectric constant as a function of the humidity leads, for example, to the following results:

Starting from a dry insulated medium (tropical soil) with dielectric constant $\epsilon = 4.8$ (real index $m=2.2$), subject to great humidification, we obtain:

- for dry ground, a phase rotation $\varphi = -180^\circ$ for all frequencies
- after humidification,

in X-band; $\epsilon = 15 - j * 9$, $nr = 4.03 - j * 1.11$ (sign - for the imaginary part in accordance with formula 3-2), $\varphi = -187.8^\circ$,

in L-band; $\epsilon = 24 - j * 4$, $nr = 4.91 - j * 0.4$, $\varphi = -182^\circ$,

i.e. phase changes of respectively -7.8° and -2° ; the - sign corresponds to a phase rotation equivalent to an increase in the optical path travelled by the wave, in accordance with the formulae 3-2, when this phase rotation is interpreted in terms of time delay.

This result shows among other things a lower sensitivity to the effects of humidity when the frequency decreases but in general that a pure dielectric effect at reflection level is always very small and this is in agreement with the observations on the interferograms where for "bare soils" there is not very much differentiation. However, the speckle effect can produce larger variations as pointed out in the above mentioned report.

5.2. Experimental measurements

Several experiments have been carried out in the laboratory (at ESIEE and JRC Ispra) in order to approach the preceding interferograms quantitatively.

5.2.1. Experiments at ESIEE

At ESIEE, experiments were conducted in order to study moisture effects on the backscattering and phase shift of microwaves by different kind of soil. An HP 8510A spectrum analyser and two X-band antennas were used to perform the measurements. experiments were limited to X-band waves because of the physical constraints due to the sample size (ref 4). These experiments provided useful orders of magnitude and helped to formulate, in a better way, the questions related to the phenomena under study.

A first experiment consisted in the measurement of the phase rotation of two samples, sand and humus, at different moisture states. The results show that for sand sample (fig 6) the phase rotation is equivalent to an increase of the distance between the sand and the antennas, the real displacement (sinking) contributes for one third to the equivalent displacement and the dielectric effect for two third. For humus sample (fig 7), an important surface swelling can be observed but the pure dielectric effect is, as for sand sample, equivalent to the surface moving away (increase of the distance sample-antenna). These measurement have been conducted at normal incidence.

In a second experiment, the samples were covered by vegetation to study the phase shift undergone by the wave upon its transmission through vegetation. The vegetation, dry or wet, consists of numerous thin stems, forming a dense and homogenous (at the wavelength scale) medium. The results show that the humidification of the leaves induce an attenuation of the amplitude of the backscattered wave and a phase rotation of -20° . An increase of the density of the vegetation (number of shoots) is also followed by a negative phase rotation. (sign - equivalent to an increasing of the optical path).

Humidification, like the increase in density, leads therefore on the one hand to attenuation and on the other to a phase rotation equivalent to an increase in the optical path. The magnitude of this results are to be compared with the phase changes observed over fields after rainy periods and allows them to be interpreted when the amplitude decreases and when the phase change corresponds to an increase in the path (positive contrast on the interferograms).

5.2.2. Experiment at the EMSL

Measurements (monostatic, polarimetric) have been performed on two samples ($1.0 \times 0.7 \text{ m}^2$) of sand in the frequency range 2 -12 GHz and for three incidence angles (18° , 23° , 28°). Progressive humidification of the samples has been performed by gently sprinkling water on the surface, from dry to saturated moist conditions. The experimental procedure and the data analysis is described in (ref 5).

The experimental results can be summarised as follows :

- In spite of the expected large increase of the backscattered sample, the signal remains generally well correlated. The phase shift is clearly dependent on the moisture level of the upper soil layer (few centimeters). In fact, a saturation level is reached very quickly, when the layer interested by the infiltration is still smaller than 10 cm.
- The humidification of the first sample (with a sinusoidal shape perpendicular to the beam, period 10 cm, amplitude 0.5 cm) leads to a phase shift of the backscattered signal at an

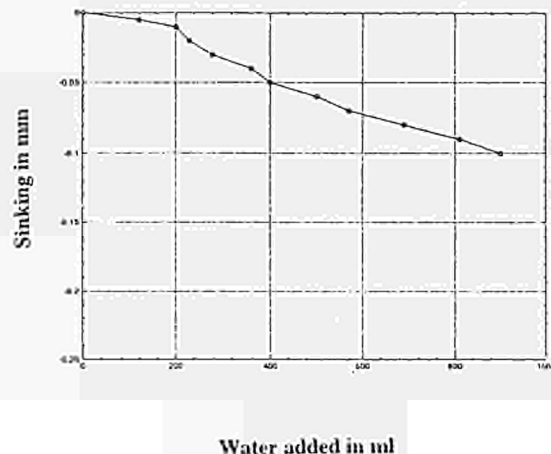
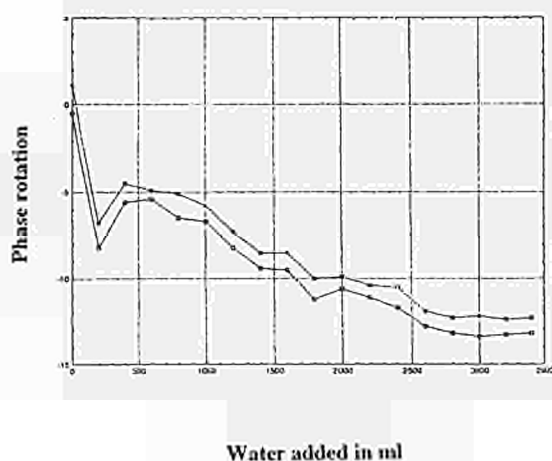


Figure 6: Reflection phase rotation and surface displacement observed for sand (ESIEE, X-VV band). The phase rotation is equivalent to the surface moving away. The sinking of the surface contributes one third.

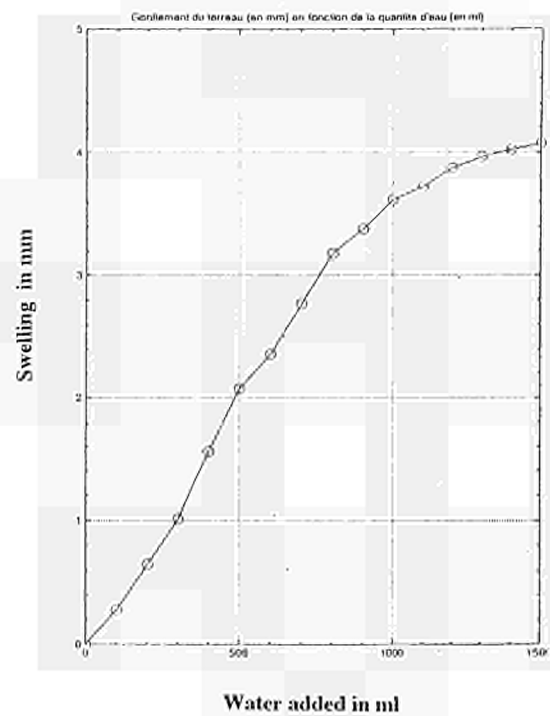
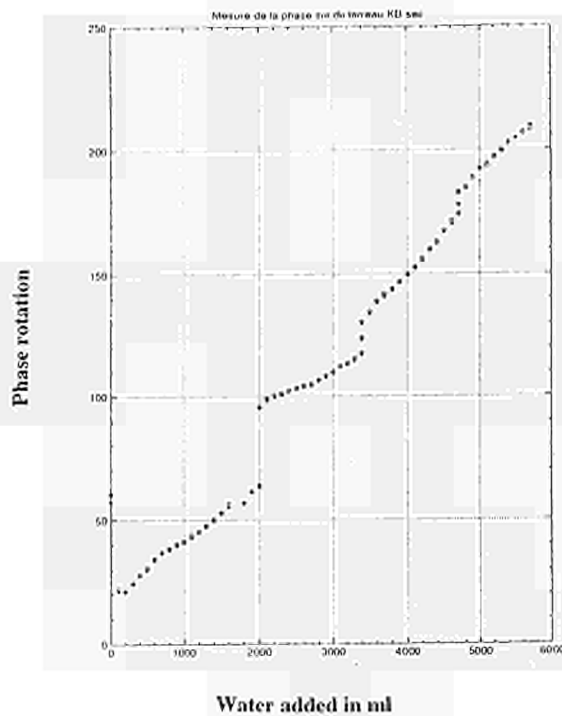


Figure 7: Reflection phase rotation and surface displacement observed for humus (ESIEE, X-VV band) The phase change is mainly due to the swelling of the surface. The purely dielectric effect is equivalent to the surface moving away.

incidence angle of 18° , reaching -35° in X-VV band and -20° in C-VV band. (**Fig 8.a**). The jumps in the curves corresponds to repeated measurements after an interval of 12 hours without adding water.

- The influence of the geometry of the reflecting soil is very important (**Fig 8.b**): the linear dependence on frequency for the first sample could suggest that a real sinking of the surface has occurred (-2.5 mm). However, this hypothesis is not confirmed by the data on the second profile (period 20 cm, amplitude 2.5 cm), where a sort of oscillation is present with an excursion in the positive range ($+15^\circ$ at 4 GHz). This effect shows that in certain configurations the dielectric effect is modulated by the geometry in such a way to result in an apparent swelling of the surface.

VI- CONCLUSIONS

The experimental approach employed allows us to appreciate quantitatively some of the causes of the variability in differential interferograms. The main points are recalled below:

- For soil, the purely dielectric effects are in general superposed on the geometric effects of sinking or swelling that depend on the nature of the soil. The humidification of sand induces sinking by a fraction of a millimeter while that of topsoil can lead to swelling of several millimeters. In addition, also the effect of surface geometry, needs to be considered.

- In most of the experiments carried out, the purely dielectric effect associated with humidification is equivalent to the backscattering surface moving away. In the only case where the opposite observation was made, the phase rotation obtained was limited to 15° . We would mention that neither the -35° neither the $+15^\circ$ can be explained by pure dielectric surface effects. Maybe a volumetric interaction takes place even if I can not image any volumetric mechanism when the whole soil layer is saturated of water.

References

1. Discriminating geophysical Phenomena in Satellite Radar interferograms
D.Massonnet, K. Feigl
Geophys. Res. Lett., 22, 1537-1540, 1995.
2. Effect of saturated areas on backscattering coefficient of the ERS 1 synthetic aperture radar: first result,
Merot P., Crave A., Gascuel-Oudoux C., Louahala S.
Water Resources Research , vol 30, (2), p 175-179, 1994.
3. Mesure au laboratoire d'effets de phase liés à des changements dielectriques d'états de surface: integration à l'échelle du pixel sol.
Rudant J.P.
Rapport 92 / CNES / 0421, 1992
4. Caractérisation d'un sol par la rotation de phase d'une onde centimétrique ,
Calonne R., Arnaud V
Mémoire d'Ecole d'Ingénieur, ESIEE, March 1995
5. Decorrelation of Backscattered Signal due to soil moisture changes
Nesti G., Tarchi D., Rudant J.P
IGARSS 95, pp 2026-2028

This work was founded by CNES and PNTS, and the ERS1 data given by ESA for the scientific project AO F 07 (Responsable Jean Chorowicz). Thanks to Patrick Gigord for offering technical assistance.

MICROWAVE SCATTERING FROM RANDOMLY ROUGH SURFACES: ELECTROMAGNETIC MODELS AND EXPERIMENTAL DATA

P. COPPO
*Centro di Telerilevamento a Microonde,
Via Panciatichi, 64
50127 Florence, Italy*

P. PAMPALONI
*IROE-CNR,
Via Panciatichi, 64
50127 Florence, Italy*

S.LOLLI
*Dipartimento di Fisica,
Università di Firenze,
Via S.Marta, Florence, Italy*

ABSTRACT. Backscattering data on artificial dielectric rough surfaces, acquired at the EMSL of Ispra (I), over a large frequency range (0.4-18 GHz), have been compared with surface scattering model simulations. The results show that theory and experiments are in agreement within the limits of experimental errors (less than 1 dB).

1. Introduction

Active microwave remote sensing is a very suitable approach for observations of large areas with high spatial (about meters) and temporal (about days) resolution in every weather conditions. From these observations it is possible to obtain important parameters of soil (water and vegetation contents, surface roughness). In fact the backscattering coefficient measured with SAR or scatterometers is a function of the geophysical and the observation parameters like frequency, observation angle and polarization state, while it is independent of other instrumental characteristics.

The physical models help us in better understanding the interaction between natural surfaces and electromagnetic fields, for the development of inversion algorithms for soil moisture and roughness retrieval from remote sensing data [1].

2. Electromagnetic models

The remote sensing parameters (the backscattering coefficient and the emissivity) can be calculated from the bistatic scattering coefficient, which is defined as the scattered power (in β polarization) of an equivalent isotropic scatterer along the direction defined from the solid angle Ω_s and the product between the incidence density power (in polarization α) in the direction defined from the solid angle Ω_i and the illuminated area. The backscattering coefficient is the bistatic scattering coefficient defined in the backward direction.

It's well-known that the effect of surface roughness on microwave backscattering depends on the observation wavelength, and a suitable analytical model valid in a large frequency and roughness range is the Integral Equation Model (IEM) [1]. This model approximates results of

the Small Perturbation Model (SPM) at the lower frequencies whilst it well reproduces the models based on Geometrical Optics (GO) and the Physical Optics (PO) at the higher frequencies.

IEM analytical solutions have been obtained calculating the surface current through an iterative method as approximations of the Kirchhoff's solutions. Two different solutions have been obtained either for low or high roughness and frequency values in the single and the multiple scattering conditions. For metallic surfaces there is a large validity range, while for the dielectric surfaces one must evaluate the product between the heights standard deviations (HSTD) and the autocorrelation length (ACL) (both normalized to the wavelength), that must be less than $1.2\sqrt{\epsilon}/4\pi^2$ (ϵ is the dielectric constant) for gaussian correlation function (1.6 than 1.2 in the other cases), or the product between the wavenumber and the correlation length, that must be greater than 5 [1]. Such validity ranges can be applied to a large number of experimental data acquired on natural surfaces.

A theoretical validation of the analytical models was carried out only in the 1D-case (surfaces generated by means of the same random profile) by using exact numerical methods (Monte-Carlo and Method of Moment) [1]; but for the 2D-case the calculation time for these numerical methods is too large. On the other hand real surfaces may not well represent the approximations introduced by the models. So a first step for a validation with experimental data is that of measuring the scattering coefficient of an experimental model, composed by a dielectric surface with well defined roughness parameters, similar to those of natural surfaces and identical to those used in the theoretical models. Indoor experiments have been carried out using EMSL and controlling both the statistical and the dielectric properties of the target.

3. Experimental work

In this paper we describe the experiments performed at the European Microwave Signature Laboratory (EMSL) (JRC-Ispra (Italy)), a large anechoic chamber (20 meter of diameter) which allows one to perform microwave monostatic and bistatic polarimetric measurements of large samples (2 meter of diameter) over a wide frequency range (0.4-18 GHz) with small steps (less than 11 MHz) [2].

A full polarimetric calibration were applied in the monostatic case, while for the bistatic case was applied a simple correction "Response & Isolation". A filter in the time domain has been applied in order to separate the scattered response of the target from the other residual responses.

Although the antenna beamwidth is a function of frequency, the illuminated area (calculated from the footprint at 3dB) is always greater than the target dimensions at all frequencies. So the convolution of the antenna beam with the target was performed and a corrective term was applied to data to compensate for the antenna gain variations with the frequency [2].

The target, contained in a cylinder 2m in diameter and 0.4m deep, has been situated in the facility focal point. Two types of azimuthal isotropic surfaces with average permittivity equal to $6.5 + j1.5$ and characterized by a gaussian correlation function have been realized [3]: a) smooth with HSTD = 0.4cm and ACL = 6cm and b) very rough with HSTD = 2.5cm and ACL = 6cm. A laser profilometer was used for testing the roughness surface parameters accuracy. A stable mixture composed by ethanadiol, water and sand was carried out to simulate a real soil with absorption relative to a certain degree of moisture content. The dielectric constant of the mixture was measured with an open coaxial probe and a network analyzer HP and through reflection measurements in the anechoic chamber, varying the frequency at an observation angle close to nadir. The measurements were carried out on a smooth thin (0.8 cm) sample (50 cm*50 cm of dimensions) composed of the same material used for the rough surfaces, and placed over a metallic plate to measure significant multiple reflections.

Independent scatterometric measurements were carried out, for a fixed frequency and observation angle, by means of azimuthal rotations (step 5°) and using many frequency samples with a step (300 MHz) greater than the frequency correlation length (the statistical error is about 0.4 dB) [2]. All scattering measurements were carried out at different incidence angles (respect to nadir) with a step of 10° in the range from 10° to 50° .

Fig 1a, b show the backscattering coefficient (pol. HH), calculated with the IEM model as a function of frequency, compared with the experimental data acquired on the smooth (**fig. 1a**) and the very rough (**fig. 1b**) surface.

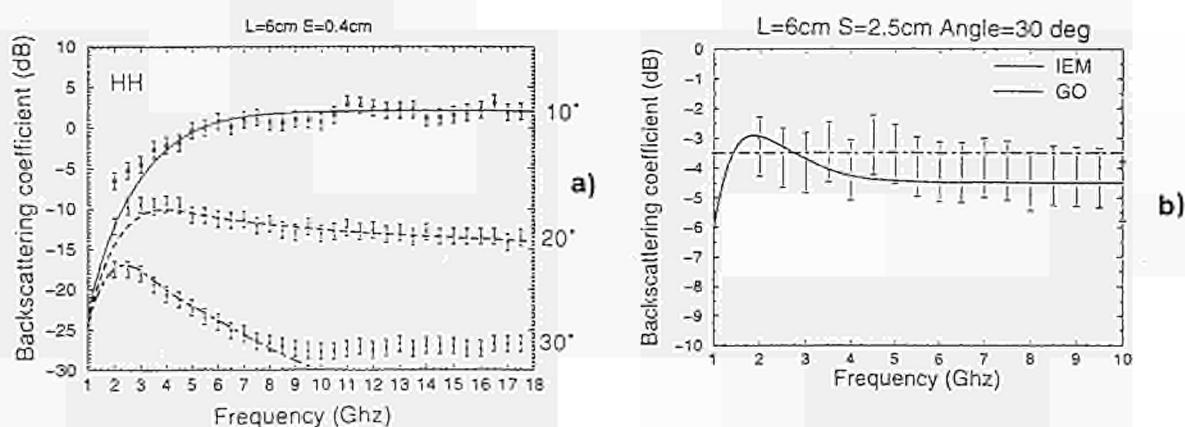


Fig.1: Backscattering coefficient (HH pol.), calculated from IEM model (continuous lines), and measured at the EMSL (points) on the smooth (a) and the very rough (b) surface, as a function of frequency at different nadir observation angles (experimental errors are less than 1 dB). Simulations realized with the Geometrical Optics Model (GO) are shown (dashed line) in the case of the very rough surface (b).

4. Conclusions

Multifrequency backscattering measurements on two experimental models with different roughness parameters have been compared with simulations performed by means of electromagnetic approximate models. The results have shown that theory and experiments are in good agreement up to a frequency of 10 GHz. On the contrary significant deviations exist at large incidence angles (greater than 30°) as the frequency increases above 10 GHz.

5. References

- [1] A.K. Fung, Microwave Scattering and Emission Models and Their Applications, Artech House, Inc., Boston 1994.
- [2] G. Nesti, P. Pampaloni, P. Coppo, M. Hallikainen, M. Mancini, P. Troch, M. Von Schonermark, "Experimental Research at the EMSL on Scattering Properties of Non Vegetated Terrains", Proc. of IGARRSS 95, 10-14 July 1995, Florence (Italy), Vol. III, pg.2020-2022, 1995.
- [3] P. Coppo, D. Tarchi, M. Weinberger, " An Experimental Model for Surface Scattering Model Validation at the EMSL", Proc. of IGARRSS 95, 10-14 July 1995, Florence (Italy), Vol. III, pg. 930-932, 1995.
- [4] P. Coppo, S. Lolli, G. Nesti, P. Pampaloni, D. Tarchi, "Microwave Surface Scattering Models Validation on Artificial Dielectric Surfaces at the EMSL", Proc. of PIERS 96, 8-12 July, Innsbruck, pg. 293, 1996.

ESTIMATING MICROWAVE OBSERVATION DEPTH IN BARE SOIL THROUGH MULTI-FREQUENCY SCATTEROMETRY

P.A. TROCH, F. VANDERSTEENE, Z. SU, and R. HOEBEN

Laboratory for Hydrology and Water Management

University of Gent

Coupure Links 653

9000 Gent

Belgium

M. WUETHRICH

Department of Geography

University of Basel

Spalenring 145

4055 Basel

Switzerland

ABSTRACT. This paper introduces a technique, based on multi-frequency microwave scatterometric measurements, to determine the depth of observation in a bare soil with given moisture profile. The data used here were collected during the B-NVT20 experiment held at the European Microwave Signature Laboratory (EMSL), Ispra (Italy) [Mancini *et al.*, 1995; Mancini and Troch, 1995]. It is hypothesized that multi-frequency microwave scatterometric measurements in the range 1-10 GHz allow the estimation of the observation depth of radar signals in bare soil. The analysis of the data is based on the assumption that the radar backscattering is a superposition of scattering from the surface and volume scattering, due to a discontinuity in the dielectric properties of the target. Therefore, the backscattering function (σ^0 as a function of observation frequency) exhibits an oscillation around the theoretical surface backscattering function. This oscillation is explained as amplitude amplification due to a phase shift in the return signal from the discontinuous layer in the soil. Non-steady series analysis, based on the Hilbert transform, is used to derive a simple expression that relates soil observation depth to observation frequency and soil moisture content.

1. Observation Depth

An expression for the depth of penetration (δ_p) can be given by considering a wave incident from air upon a soil surface in the z direction. Part of its power is scattered back into the air and the remainder is transferred into the soil medium across the boundary. If the transmitted power at a point just beneath surface ($z = 0_+$) is $P(0_+)$, the power at a given depth z is given by Ulaby *et al.* [1982] :

$$P(z) = P(0_+) \exp\left(-\int_0^z \kappa_e(z') dz'\right) \quad (1)$$

where $\kappa_e(z)$ is the extension coefficient of the soil medium at depth z . The penetration depth is defined as the depth $z = \delta_p$ for which the power equals $1/e$ of the transmitted power just below the surface:

$$\frac{P(\delta_p)}{P(0_+)} = \frac{1}{e} \quad (2)$$

In the following analysis of multi-frequency microwave signals the term observation depth (d) is introduced. This quantity, with a dimension of length, should not be interpreted as the above mentioned penetration depth. A formal definition of d is given in equations 6 and 7.

2. Surface And Volume Scattering

In principle, both surface and volume scattering are present in scattering or emission from terrain [Ulaby *et al.*, 1982]. In surface scattering, the scattering strength is proportional to the relative complex dielectric constant of the surface $\epsilon = \epsilon' + i\epsilon''$, and its angular scattering pattern is governed by the surface roughness. In volume scattering, the scattering strength is proportional to the dielectric discontinuities inside the medium (below the boundary surface) and the density of the embedded inhomogeneities, and its angular scattering pattern is determined by the roughness of the boundary surface, the average dielectric constant of the medium, and the geometric size of the inhomogeneities relative to the incident wavelength. Since volume scattering is caused mainly by dielectric discontinuities within a volume, and, in general, the spatial locations of discontinuities are random, the scattered waves within the volume are in all directions.

To determine the presence of volume scattering, we need to know (1) if the medium is inhomogeneous and (2) what its effective depth of observation is. Usually, (1) is known from physical properties and (2) can be estimated from the dielectric properties of the medium. For materials with $\epsilon''/\epsilon' < 0.1$, such as mineral soils, an approximate formula for the penetration depth, δ_p , is given by:

$$\delta_p = \frac{\lambda\sqrt{\epsilon'}}{2\pi\epsilon''} \quad (3)$$

where λ is the wavelength. It should be noted that the values for δ_p obtained from Equation 3 are somewhat larger than those for real soil conditions, because Equation 3 does not take account of losses due to scattering in the soil medium.

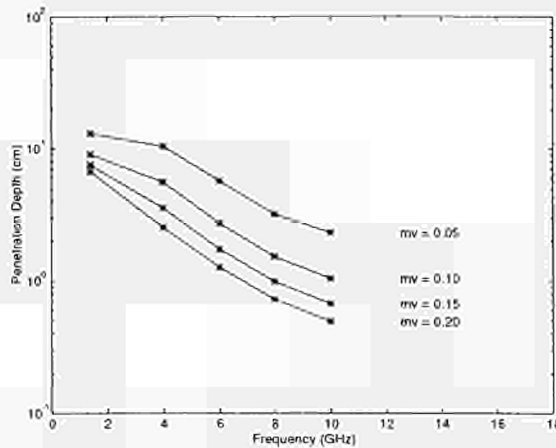


Figure 1: Depth of penetration in a sandy-loam soil at different moisture contents and for different observation frequencies.

3. Microwave Dielectric Behavior Of Wet Soils

In order to apply Equation 3 to determine the depth of observation of microwaves in soils, we need to know the dielectric behavior of wet soils in the microwave frequency range. Wet soil is a mixture of soil particles, air, bound and free water. The complex dielectric constants of bound and free water, at constant temperature and salinity, are each function of the electromagnetic frequency, f . Therefore, the dielectric constant of the soil mixture at constant temperature and salinity is a function of frequency, the total volumetric moisture content, m_v , and the soil texture.

Hallikainen *et al.* [1985] have performed dielectric constant measurements for five different soil types at frequencies between 1.4 and 18 GHz. They found that soil texture has a pronounced effect on dielectric behavior, especially at frequencies below 5 GHz. Based on these measurements, Hallikainen *et al.* [1985] derived separate polynomial expressions, relating the real and imaginary part of ϵ to the volumetric moisture content, m_v , and the percentage of sand and clay. These polynomial expressions are of the following form:

$$\epsilon'(\text{or } \epsilon'') = (a_0 + a_1S + a_2C) + (b_0 + b_1S + b_2C)m_v + (c_0 + c_1S + c_2C)m_v^2 \quad (4)$$

where S is percentage (by weight) of sand, C is percentage of clay, and a_i, b_i, c_i are coefficients which depend on frequency. Table II in Hallikainen *et al.* [1985] gives the numerical values for these coefficients for different frequencies.

Knowing the volumetric moisture content and the sand and clay content for the soil under study, we can now use Equation 4 to estimate the real and imaginary part of the dielectric constant of the soil at the given observation frequency. Figure 1 shows the depth of penetration in a sandy-loam soil ($S = 63.8\%$; $C = 8.5\%$) at different moisture contents and for different observation frequencies, as computed from Equation 3 using Equation 4.

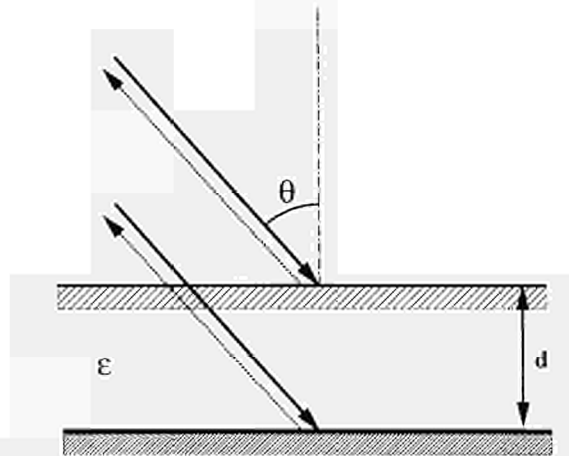


Figure 2: Surface and volume scattering from a bare soil. Part of the radar signal is backscattered directly from the surface, part of it is backscattered after penetration to a depth d where the soil shows a discontinuity in the dielectric properties.

4. Multi-Frequency Scatterometry

Figure 2 shows schematically the experimental set-up used in the B-NVT20 experiment (for more information, we refer to Mancini *et al.* [1995]). The target consists of a cylindrical container with bare soil with relative dielectric constant $\epsilon = \epsilon' + i\epsilon''$ and given surface roughness characteristics. Imagine an electromagnetic wave with given frequency f reaching the target at an incidence angle θ . The return signal to the radar antenna is a superposition of a surface scattering term and a volume scattering term. The volume scattering term can be thought of as the backscattered wave after having penetrated in layer 1 to a vertical distance d (location of assumed discontinuity in dielectric properties). For a given observation frequency f the phase shift between the surface and the volume backscattering wave is given by:

$$\phi = \frac{4\pi R}{\lambda} = 4\pi R \frac{f}{c} \quad (5)$$

where ϕ is the phase shift, λ is the wavelength, c is the propagation velocity of light in dielectricum 1, and $R = d/\cos\theta$. We can now compute the shift in observation frequency which is needed to obtain a maximum phase shift ($\phi = 2\pi$):

$$\Delta f = \frac{c \cos\theta}{2d} \quad (6)$$

Since $c = c_0/\sqrt{\epsilon}$, with c_0 the propagation velocity in vacuum, we can write:

$$\Delta f = \frac{c_0 \cos\theta}{2d\sqrt{\epsilon}} \quad (7)$$

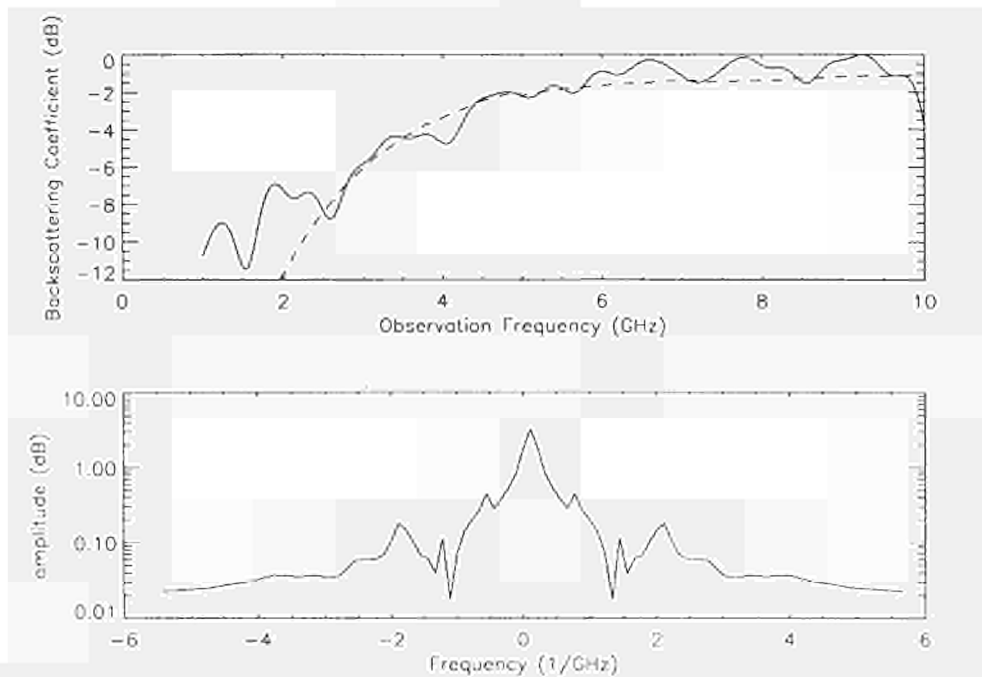


Figure 3: Up: multi-frequency (1-10 GHz; HH polarization) scatterometric measurements of bare soil with uniform moisture profile ($m_v = 9\%$) at an incidence angle $\theta = 11$ deg; Down: Fourier spectrum of backscattering function

From Equation 7 we see that the observation frequency shift, Δf , increases with decreasing observation depth. Equation 7 will produce oscillations in the backscattering function when multi-frequency observations are performed. The dominant frequencies of the oscillations in the backscattering function should decrease with increasing observation frequency.

The upper part of Figure 3 shows the backscattering function for one of the scatterometric experiments during B-NVT20. The incidence angle is 11 deg and the volumetric moisture content is 9 % (TDR measurements, [Mancini *et al.*, 1995]). During the radar measurements, the soil had an almost uniform moisture profile in the upper 20 cm layer. Also shown is the prediction of the surface backscattering function, based on the *Integral Equation Model* (IEM, [Fung *et al.*, 1992]). It is clear from this figure that the general trend of the backscattering function in the frequency range 2.5-10 GHz is well explained by this model, but that the oscillations in the empirical data are not explained. We put forward the hypothesis that these oscillations are due to amplitude amplification from volume scattering through the mechanism discussed above. If this hypothesis holds we can estimate Δf in Equation 7 directly from multi-frequency scatterometry measurements and compute d . Because Δf is observation frequency dependent, the final result of this analysis will be a relationship of the form:

$$d = \text{fct}(f) \quad (8)$$

Equation 8 is an alternative expression to compute the depth of observation when multi-frequency scatterometric observations are available.

5. Power Spectrum And The Hilbert Transform

The lower part of Figure 3 shows the Fourier spectrum of the scatterometric data. Besides the DC component at 0 frequency, we can observe 3 dominant frequencies (one at 0.64 GHz^{-1} , one at 1.3 GHz^{-1} , and one at 2 GHz^{-1}). From Equation 7, and using the real part of the relative dielectric constant measured by the TDR technique for this soil ($\epsilon' = 4.83$), which is close to the value obtained from Equation 4, the corresponding observation depths are 4 cm, 9 cm, and 13 cm, resp. Unfortunately, the Fourier spectrum yields information only about the global rather than the local properties of the signal. When we want to investigate the observation frequency dependence of the phase shift, we need to analyse the local properties of the signal. Recently, a technique based on the Hilbert transformation has been developed for non-steady series analysis [Huang *et al.*, 1992; Long *et al.*, 1995]. We refer to Long *et al.* [1995] for a full description of the Hilbert techniques.

These techniques are based on the Hilbert transformation. For any real observation series, $\zeta(t)$, its Hilbert transform, $\xi(t)$, is:

$$\xi(t) = \frac{1}{\pi} P \int_{-\infty}^{+\infty} \frac{\zeta(\tau)}{\tau - t} d\tau \quad (9)$$

where P indicates the principal value, and t is the independent variable against which the observations are made (e.g. time or, in our case, observation frequency). Now we can define the analytic signal, $Z(t)$, based on the real observation series:

$$Z(t) = \zeta(t) + i\xi(t) = a(t) \exp i\chi(t) \quad (10)$$

where $a(t)$ is the amplitude, and $\chi(t)$ is the phase function:

$$\begin{aligned} a(t) &= \sqrt{\zeta(t)^2 + \xi(t)^2} \\ \chi(t) &= \tan^{-1} \frac{\xi(t)}{\zeta(t)} \end{aligned} \quad (11)$$

By definition, the local frequency is given by:

$$\omega(t) = -\frac{d\chi}{dt} \quad (12)$$

So, we now have an expression of frequency as function of t .

This analysis is used here to detect the dominant frequencies in the oscillations of the backscattering function. As discussed above, the apparent oscillations in Figure 3 are due to volume scattering, and their dominant periods (here in GHz units!) are observation frequency dependent. Figure 4 shows the backscattering function in the frequency range 2.5-10 GHz, after removal of the surface scattering term by subtracting the IEM predicted backscattering coefficients. From Equation 9 and 11 we then compute the phase as a function of observation frequency (Figure 5).

Here, the slope is, by definition, the local frequency. Due to numerical inaccuracy and measurement noise, the curve in Figure 5 is not easily differentiable. We therefore propose to use only the general trend in the phase plot by curve fitting a hyperbolic function to the data. Differentiating this smooth function with respect to observation frequency now yields the local frequency. This local frequency represents the reciprocal value of Δf in Equation 7.

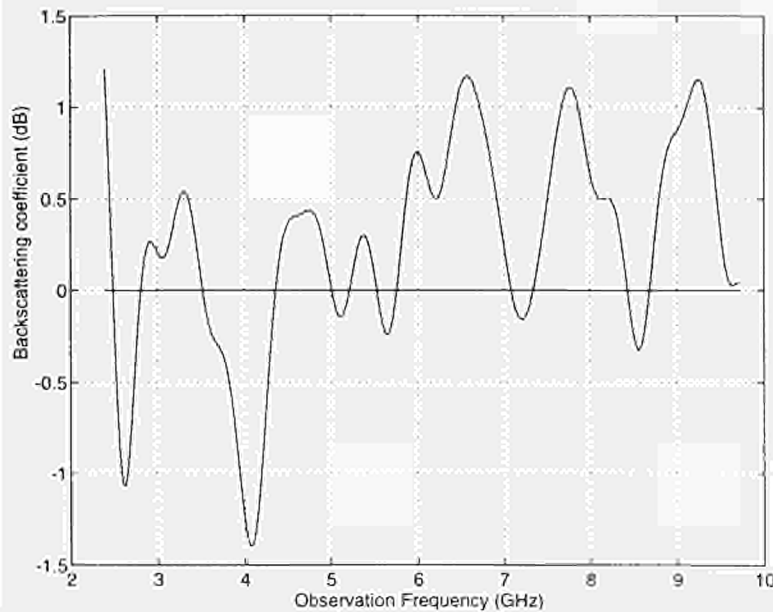


Figure 4: Backscattering function of the sandy-loam soil with $m_v = 9\%$ in the frequency range 2-10 GHz and after removing the surface backscattering.

Figure 6 gives the local periodicity of the oscillations in the backscattering function. Introducing this result in Equation 7 allows us to present Equation 8 graphically (Figure 7). We have used only ϵ' in Equation 7 because in our case $\epsilon'' \ll \epsilon'$. We see that the depth of observation decreases with increasing observation frequency. The values of d computed based on the Fourier spectrum are preserved, but the Hilbert transformation technique additionally allows to estimate the variation of d over the entire range of microwave frequencies.

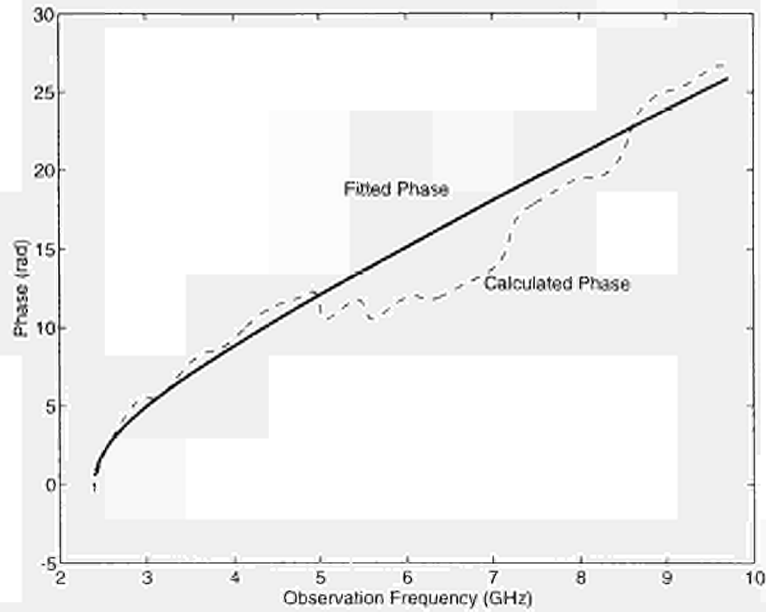


Figure 5: Phase, as defined by Equation 11, as a function of observation frequency. The solid line is a hyperbolic function fitted to the data.

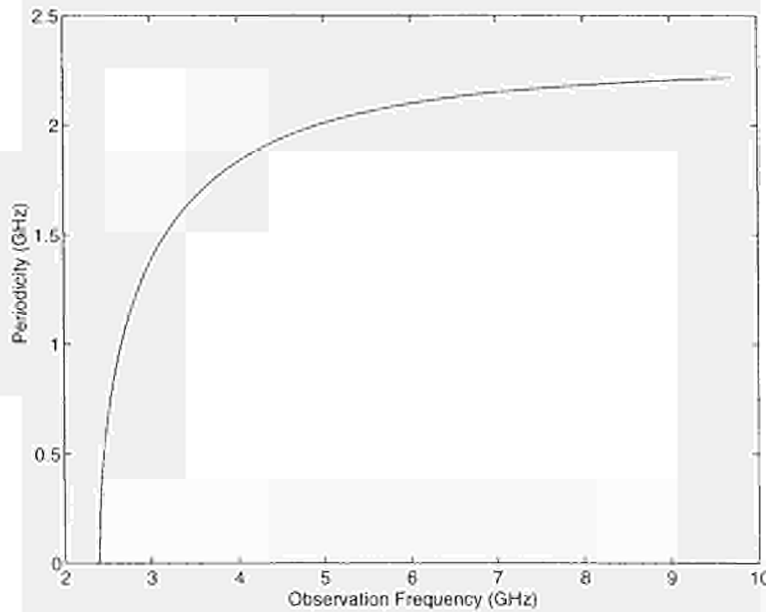


Figure 6: Observation frequency shift (periodicity) as a function of observation frequency.

Also shown in Figure 7 is the estimated depth of penetration based on Equation 3. As seen from this figure, the order of magnitude of both methods is the same, but the variation with frequency is different. The method suggested by Ulaby *et al.* [1982] yields a function which decays less rapidly compared to the predictions based on multi-frequency scatterometry. This could be an artefact of the curve fitting procedure used to compute the phase plot. More research is needed here.

6. Conclusions

This paper attempts to explain the observed oscillations in the backscattering function of a bare soil with given moisture content and given roughness characteristics. It is hypothesized that these oscillations are the result of amplitude amplification due to surface and volume scattering. If this is true the dominant periods of these oscillations should be observation frequency dependent. Moreover, these dominant periods can be related to the depth of observation of the microwave signal. Therefore we have used the Hilbert transformation to analyse the signal, since this technique yields information about the local properties of a non-steady state signal. For the data set under study, we have found that the depth of observation for volume scattering decreases rapidly with observation frequency. This behavior is similar to the behavior predicted by Ulaby *et al.* [1982].

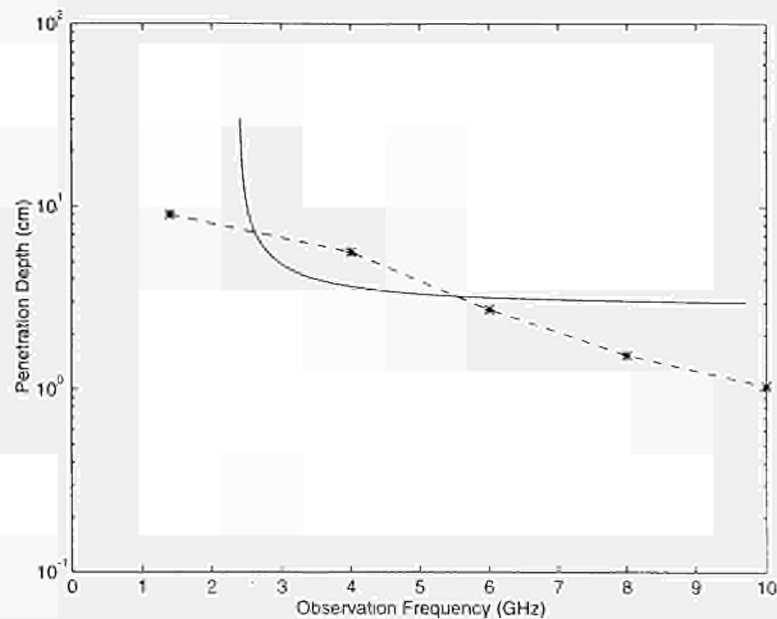


Figure 7: Depth of observation as a function of observation frequency, as derived from Figure 5 and Equation 7 (solid line) and derived from Equation 3 (dashed line).

References

- Fung, A. K., Lee, Z., and Chen, K. S. (1992). Backscattering from a randomly rough dielectric surface. *IEEE Trans. Geosci. Remote Sensing*, 30(2), 356–369.
- Hallikainen, M. T., Ulaby, F. T., Dobson, M. C., El-Rayes, M. A., and Wu, L.-K. (1985). Microwave dielectric behavior of wet soil, Part I: Empirical models and experimental observations. *IEEE Trans. Geosci. Remote Sensing*, 23(1), 25–34.
- Huang, N. E., Long, S. R., Tung, C.-C., Donelan, M. A., Yuan, Y., and Lai, R. J. (1992). The local properties of ocean surface waves by the phase-time method. *Geo. Res. Letters*, 19, 685–688.
- Long, S. R., Huang, N. E., Tung, C.-C., Wu, M.-L. C., Lin, R.-Q., Mollo-Christensen, E., and Yuan, Y. (1995). The Hilbert techniques: An alternate approach for non-steady time series analysis. *IEEE Geo. Remote Sensing Soc. Newsletter*, March, 6–11.
- Mancini, M., and Troch, P. A. (1995). Experimental setup for soil moisture profile determination using multi-frequency backscattering data. *EMSL Newsletter*, 1(5), 6–8.
- Mancini, M., Vandersteene, F., Troch, P. A., Bolognani, O., Terzaghi, G., D'Urso, G., and Wüthrich, M. (1995). Experimental setup at the EMSL for the retrieval of soil moisture profiles. In *Proc. International Geoscience and Remote Sensing Symposium (IGARSS)* (pp. 2023–2025). Firenze, Italy.
- Ulaby, F. T., Moore, R. K., and Fung, A. K. (1982). *Microwave remote sensing, active and passive, Volume II: Radar remote sensing and surface scattering and emission theory*. Norwood, MA: Artech House, Inc.

Part 2
New ideas for potential
use of EMSL

A Circular Synthetic Aperture Radar System for Ground-Based Applications

Authors : A. Broquetas, R. De Porrata, Ll. Sagués
Dpt. Teoria del Senyal i Comunicacions
Universitat Politècnica de Catalunya (UPC)
Campus Nord UPC, D3
08034, Barcelona
SPAIN

ABSTRACT.- This paper presents a SAR processor capable of obtaining radar images from measurements carried out with antennas that describe a circular trajectory. The analytical formulation of the processor is presented along with its ground range and azimuth resolutions. Some experimental results obtained in anechoic chamber are also shown.

1. Introduction

Most of the existing SAR systems are airborne or spaceborne radar systems. Ground-based SAR systems, however, are better suited for those applications where resolution in the order of cm or a very low-cost system are required. This is the case, for instance, of anti-personnel mine detection. In contrast to airborne and spaceborne SAR, wherein the whole platform describes a linear trajectory, in truck-mounted or tower-mounted SAR only the antennas move whereas the rest of the system remains static. The mechanical implementation of a linear trajectory for the antennas (L-SAR) becomes therefore problematic. The C-SAR algorithm here presented overcomes this problem by allowing the antennas to describe a circular trajectory. Furthermore, with this configuration a coherent ground-based scatterometer can be easily transformed into a radar imaging system without hardly any mechanical modification (fig.1).

The inputs of the C-SAR reconstruction algorithm are the coherent measurements of the scattered field as a function of frequency and azimuth angle. Because of the short distance between the illuminated area and the antennas, the plane-wave approximation is not valid. Thus, the C-SAR processor must be developed using spherical-wave formulation, which is based on the 2D spherical wave ISAR technique [1].

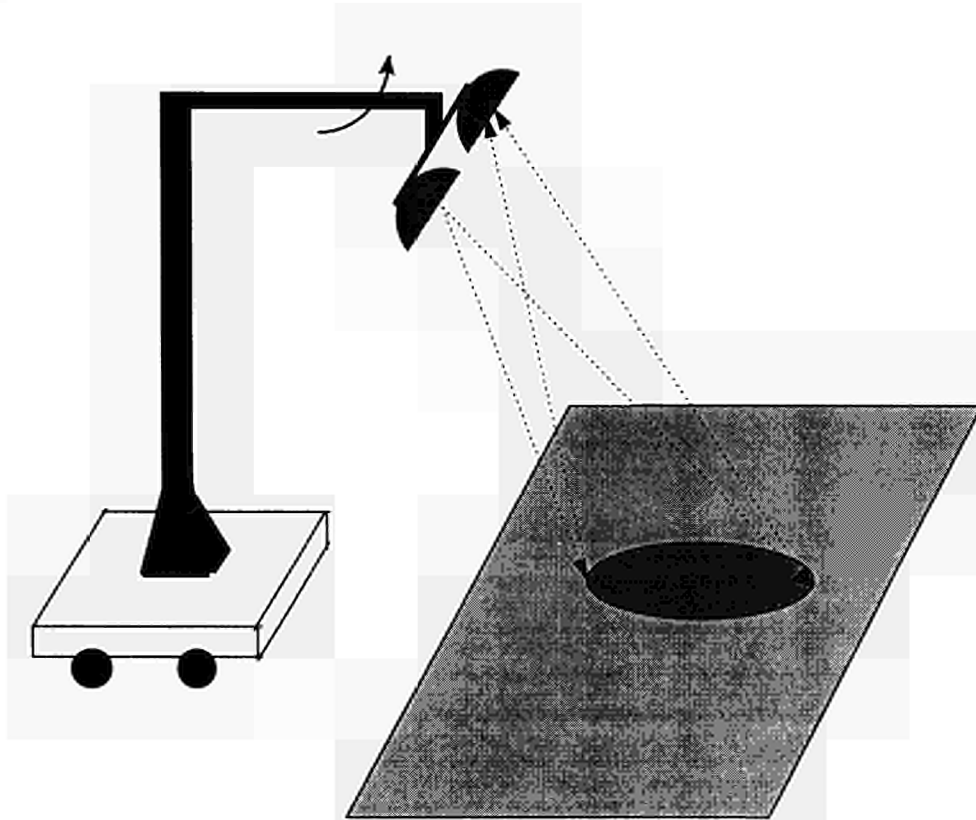


Fig.1.- Truck mounted C-SAR system.

2. C-SAR Processor

2.1 PROBLEM STATEMENT

The geometry of a C-SAR system is illustrated in fig. 2. The scatterer, located at point S, remains stationary at a position (ρ, ϕ) of the xy plane. The antennas are located at (R, ϕ_a, h) and point at I, the center of the illuminated area, with an off-nadir elevation angle of θ_{elev} . Assuming that the target is formed by a distribution of non-directional and independent scatterers of reflectivity $\psi(\rho, \phi)$, the complex value of the field scattered back to the receiver will be given by the coherent addition of the contributions associated with each scatterer:

$$E_s(f, \phi_a) = \int_0^{\infty} \int_0^{2\pi} E_{0s} \cdot \psi(\rho, \phi) \cdot \frac{e^{-j\frac{4\pi}{\lambda} d_{AS}}}{d_{AS}^2} \cdot \rho \, d\phi \, d\rho \quad (1)$$

where
$$d_{AS} = \sqrt{R^2 + \rho^2 - 2R\rho \cos(\phi - \phi_a) + h^2} \quad (2)$$

is the distance between the antennas and the scatterer, and E_{0s} is a constant that depends upon parameters of the system such as antenna gain and transmitted power among others. Since this constant will be removed by external calibration, it will not be considered henceforth.

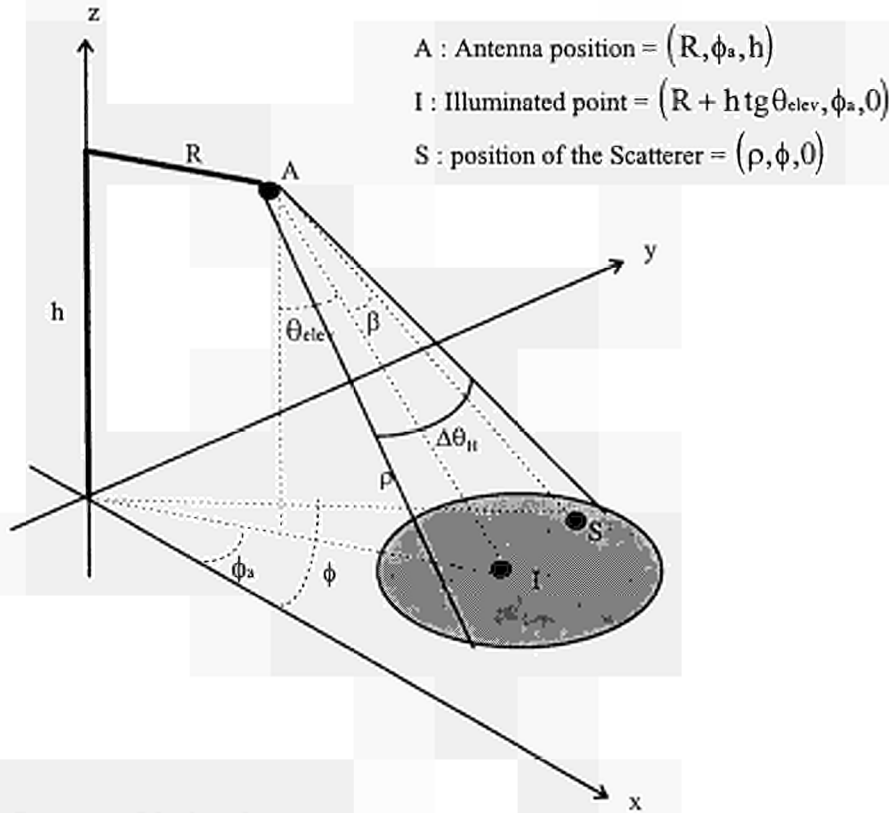


Fig. 2.- Geometry of the imaging system.

The objective of the imaging system will be the reconstruction of the reflectivity map from a set of measurements $E_s(f, \phi_a)$ at different frequencies and angles. That is to say, the inversion of equation (1).

In mathematical terms:

$$\hat{\psi}(\rho', \phi') = \int_0^{\infty} \int_0^{2\pi} E_s(f, \phi_a) \cdot \xi(f, \phi_a, \rho', \phi') \, d\phi_a \, df \quad (3)$$

where $\xi(f, \phi_a, \rho', \phi')$ is the kernel function to be found so that the image $\hat{\psi}(\rho', \phi') \cong \psi(\rho, \phi)$.

Although no simple inversion of (1) can be easily found, an exact inversion is neither strictly necessary nor even useful because not all samples of $E_s(f, \phi_a)$ will be available. Hence, the solution adopted is an inversion of the type Synthetic aperture adapted to the observation geometry.

For a given scene point (ρ', ϕ') , $\xi(f, \phi_a, \rho', \phi')$ should “focus” all the performed measurements on this point by generating the argument and amplitude that the wave has “lost” on its way to and back from the scatterer located at (ρ, ϕ) . The proposed solution is therefore:

$$\xi(f, \phi_a, \rho', \phi') = e^{j \frac{4\pi}{\lambda} \sqrt{R^2 + \rho'^2 - 2R\rho' \cos(\phi' - \phi_a) + h^2}} \cdot [R^2 + \rho'^2 - 2R\rho' \cos(\phi' - \phi_a) + h^2] \cdot f \quad (4)$$

which gives:

$$\hat{\psi}(\rho', \phi') = \int_0^{\infty} \int_0^{2\pi} E_s(f, \phi_a) e^{j \frac{4\pi}{\lambda} \sqrt{R^2 + \rho'^2 - 2R\rho' \cos(\phi' - \phi_a) + h^2}} \cdot [R^2 + \rho'^2 - 2R\rho' \cos(\phi' - \phi_a) + h^2] \cdot f \, d\phi_a \, df \quad (5)$$

The following step would be to compute the response $\hat{\psi}(\rho', \phi')$ to a known input. If this input is a single scatterer, the response is known as point-spread function (PSF). With the proposed inversion, what we have is “sensitivity space invariance” in cylindrical coordinates. That means that for a given scatterer a constant value is recovered in the reconstruction, wherever it is located. However, due to the circular geometry, in principle, we don't have shape invariance of the PSF, although can be considered approximately constant within the ranges of practical interest.

Fig. 3 and 4 show a radial (ρ) and azimuthal (ϕ) cut of the response to different scatterers obtained from a simulated reconstruction. As we can see in fig. 3 and 4 the processor presents good dynamic range, the sidelobe levels and resolution are similar to conventional ISAR [1], and besides, the PSF can be considered approximately space invariant both in range and in azimuth.

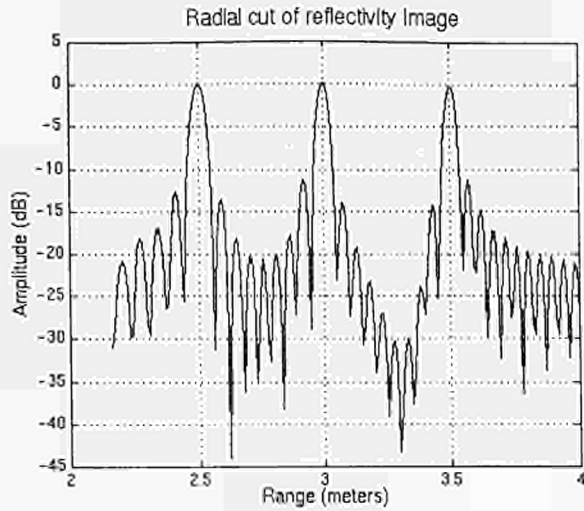


Fig. 3.- Different point spread functions at $\rho=2.5\text{m}$, $\rho=3\text{m}$, $\rho=3.5\text{m}$.
 $R=1\text{m}$, $h=2\text{m}$, $\theta_{\text{elev}}=45^\circ$, $\Delta\theta_H=30^\circ$.
 Frequency sweep from 12 to 16 GHz.

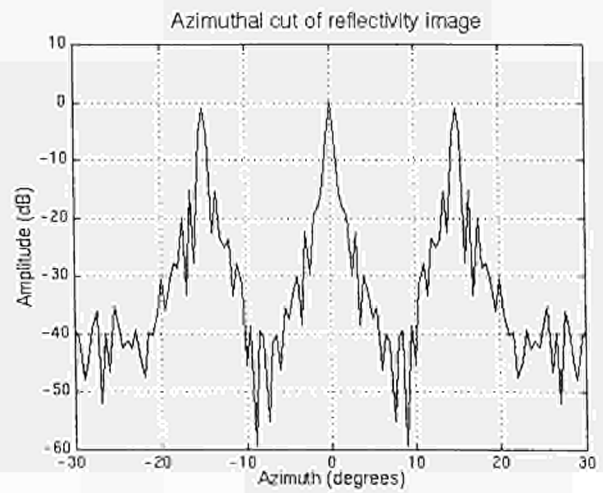


Fig. 4.- Different point spread functions at $\phi=-15^\circ$, $\phi=0^\circ$, $\phi=15^\circ$.
 $R=1\text{m}$, $h=2\text{m}$, $\theta_{\text{elev}}=45^\circ$, $\Delta\theta_H=30^\circ$.
 Frequency sweep from 12 to 16 GHz.

2.2 RADIATION DIAGRAM INTEGRATION

The effects of the radiation diagrams of both transmitter and receiver antennas $G_T(\beta)$ and $G_R(\beta)$ can be taken into account and corrected in the reconstruction by multiplying $\xi(f, \phi_a, \rho', \phi')$ by

$\frac{1}{(G_T(\beta) \cdot G_R(\beta))}$. The angle β is shown in Fig. 1 and can be expressed as a function of the

geometric parameters of the system:

$$\beta = \cos^{-1} \left[\frac{\cos(\theta_{\text{elev}})}{2hd_{AS}} \left(d_{AS}^2 - d_{SI}^2 + \frac{h^2}{\cos^2(\theta_{\text{elev}})} \right) \right] \quad (6)$$

$$\text{where } d_{SI} = \sqrt{(R + h \operatorname{tg} \theta_{\text{elev}})^2 + \rho^2 - 2\rho(R + h \operatorname{tg} \theta_{\text{elev}}) \cos(\phi - \phi_a)} \quad (7)$$

is the distance between the position of the scatterer and the illuminated point; For this purpose $G_T(\beta)$ and $G_R(\beta)$ can be modelled by using a gaussian or parabolic approximation.

In the reconstruction process, however, we can not use all of the samples because in non-illuminated areas the diagram correction would amplify noise to intolerable levels. Therefore, when applying the diagram correction only information which is limited to the swath created by the radiation diagram of the antennas should be considered.

2.3 IMAGE RESOLUTION

The range resolution ΔR depends on the time pulse resolution $\Delta \tau$, which is the inverse of the bandwidth system $B = f_{\text{max}} - f_{\text{min}}$ [2]. The resolution in slant range is given by:

$$\Delta R = \frac{c \cdot \Delta \tau}{2} = \frac{c}{2B} \quad (8)$$

which finally gives a ground range resolution of:

$$\Delta R_g = \frac{\Delta R}{\sin(\theta_{\text{elev}})} = \frac{c}{2B \sin(\theta_{\text{elev}})} \quad (9)$$

The azimuth resolution is different from the conventional linear SAR due to its circular geometry. In this sense, the azimuth resolution of the C-SAR system is defined as the ability to discriminate in angle two closed radar targets which are located at the same arc. Since far field approximations are not valid in the C-SAR geometry, the calculation of the resolution becomes more complex than the L-SAR case [2].

The azimuth resolution of the C-SAR system is:

$$\Delta S = \frac{c}{4f_{\text{max}}} \cdot \frac{\sqrt{R^2 + \rho^2 - 2R\rho \cos(\Delta\theta_H/2) + h^2}}{R \sin(\Delta\theta_H/2)} \quad (10)$$

where $\Delta\theta_H$ is the 3 dB beamwidth of the antennas.

If the antennas present a high directivity $\sin(\Delta\theta_H/2)$ can be aproximated by $\Delta\theta_H/2$ and $\cos(\Delta\theta_H/2)$ by 1. In consequence, the azimuth resolution can be aproximated by:

$$\Delta S \cong \frac{c}{2f_{\text{max}} \Delta\theta_H} \sqrt{\left(\frac{\rho}{R} - 1\right)^2 + \left(\frac{h}{R}\right)^2} \quad (11)$$

If the azimuth resolution is calculated at the illuminated point it can be finally expressed as:

$$\Delta S \cong \frac{c}{2f_{\text{max}}} \cdot \frac{h}{R} \cdot \frac{1}{\cos \theta_{\text{elev}}} \quad (12)$$

At Fig. 5 the ground range and azimuth resolutions are jointly represented as a function of the off-nadir elevation angle. As we can see in this figure, the best off-nadir elevation angle is that where both resolutions are equal, and it can be calculated equalling the expressions (9) i (12):

$$\theta_{\text{elevop}} = \text{tg}^{-1} \left[\frac{R}{h} \cdot \frac{f_{\text{max}}}{B} \cdot \Delta\theta_H \right] \quad (13)$$

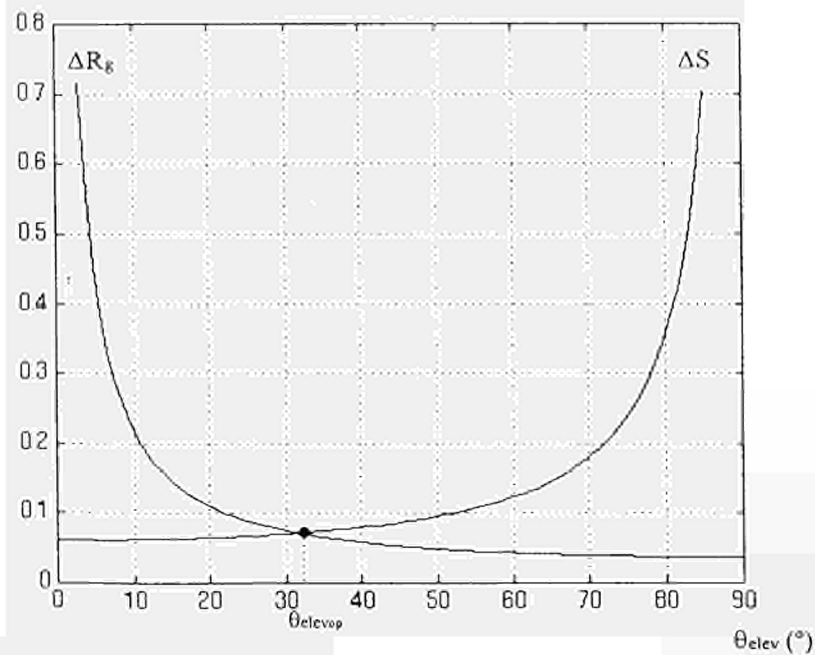


Fig. 5.- Ground range and azimuth resolutions.
 $R=1\text{m}$, $h=2\text{m}$, $\Delta\theta_H=20^\circ$.
 Frequency sweep from 12 to 16 GHz.

3. Measurements

Several multifrequency measurements have been undertaken in the X-band at the electromagnetic anechoic chamber of the Universitat Politècnica de Catalunya (U.P.C). The measurement system consists of an HP 8530A network analyzer and two antennas placed at the end of a 0.9 m metallic bar mounted on an azimuth positioner. A PC controlled the HP 8530A via the GPIB to perform a frequency sweep for each angular sample point. The transmit-receive antennas were two rectangular horns located at a height of 1.95 m, with an off-nadir elevation angle of 45° . For all measurements, the number of angular and frequency sampling points were selected to satisfy the Nyquist sampling criterion.

3.1 TRIHEDRAL SCATTERER MEASUREMENTS

Fig. 6 shows the reconstructed image for horizontally polarized copolar data sampled over 161 angular points measured from 12 to 16 GHz with a frequency interval of 10 MHz. This image correspond to five identical small trihedrals spread on the ground of the anechoic chamber. The quasi-space invariancy as well as the uniform sensitivity can be observed in this image.

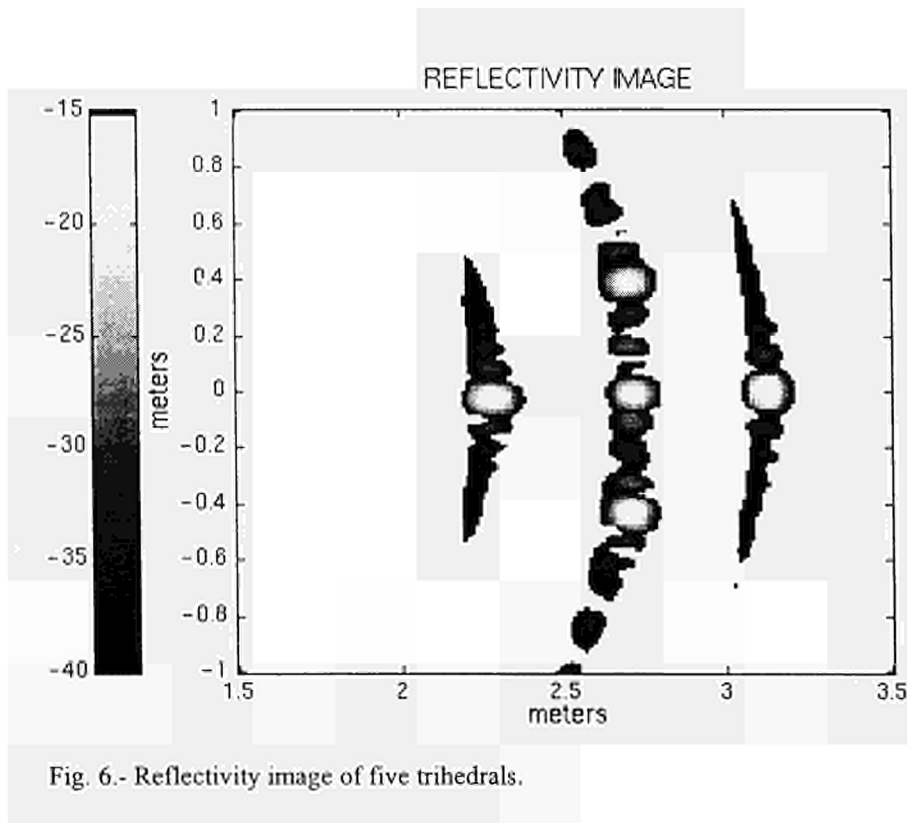


Fig. 6.- Reflectivity image of five trihedrals.

3.2 DISTRIBUTED SCATTERER MEASUREMENTS

An important real application of C-SAR system is anti-personnel mine detection. In this context, three plastic mines (5, 10, 20cm) and a small stone were spread over a large region of soil inside the anechoic chamber, (as it is shown at fig. 7). The measurement was carried out with HH polarization, 161 point in azimuth and from 12 to 18 GHz with frequency interval of 15 MHz. Fig. 8 shows the reconstructed SAR image.

As we can see, all three mines are detected and located at its exact position, and moreover, they can be discriminated from the little stone. However, the largest mine is focalized at two different points mainly due to its different height.

4. Conclusions

A Circular Synthetic Aperture Radar Processor has been presented and evaluated. This system has been designed in order to obtain radar images using a ground-based scatterometer, where only the antennas move describing a circular trajectory.

Although the formulation and implementation are more complicated than a conventional linear SAR, the experimental setup is considerably simplified and the C-SAR image resolution is higher. This is why small objects, like anti-personnel mines, can only be located by the C-SAR system. These results can be a start point for future activities in collaboration with the EMSL in mine detection applications.

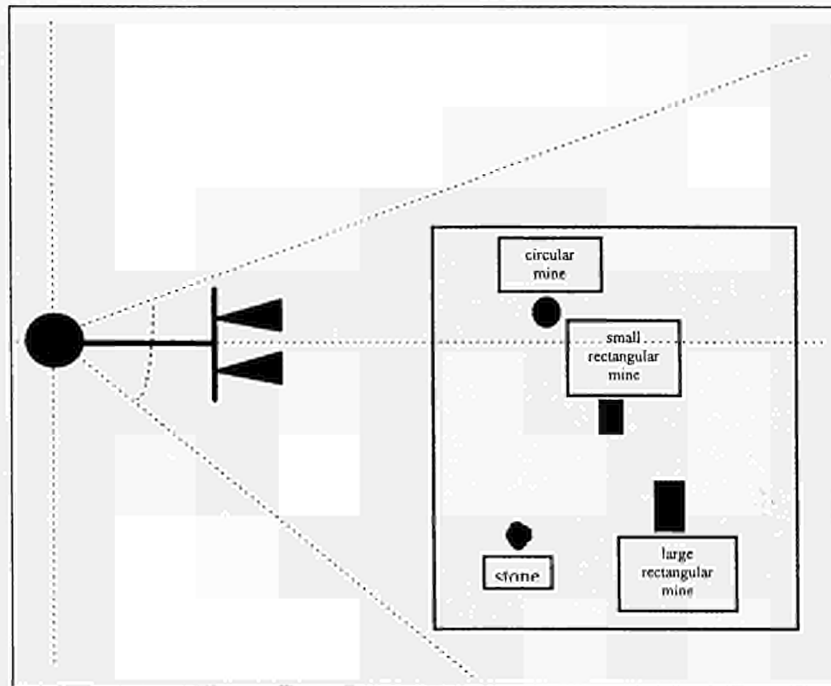


Fig. 7.- Localisation of three mines and a stone.

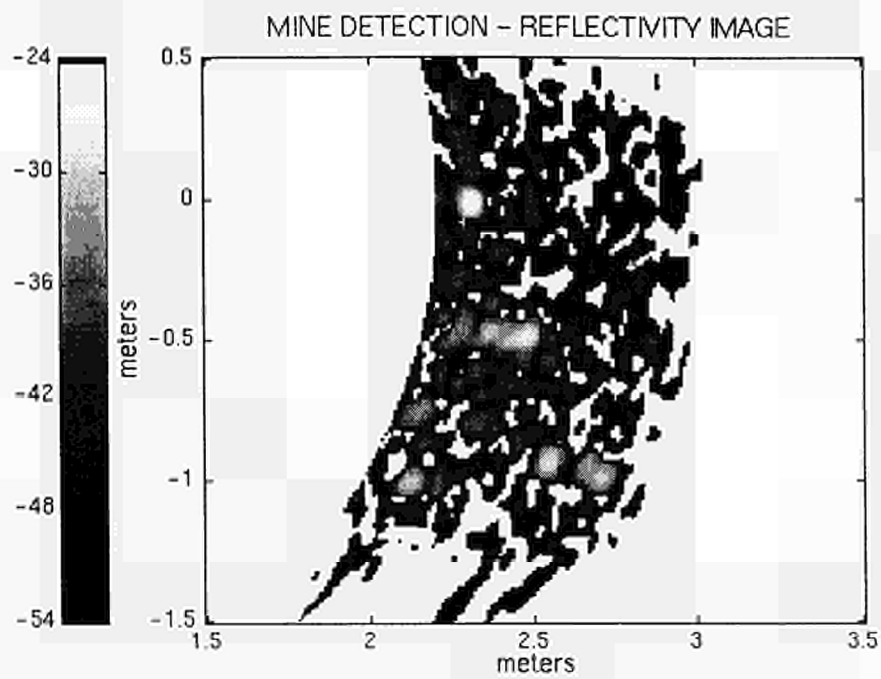


Fig. 8.- Reflectivity image of three mines and a stone placed over a soil region.

Acknowledgements

This work has been supported by the Spanish Commission for Science and Technology CICYT TIC 96-0879.

References

[1] A. Broquetas, L. Jofre, A. Cardama, "A near field Spherical Wave Inverse Synthetic Aperture Radar technique", Chicago 1992, IEEE Antennas and Propagation Society International Symposium, Volum Two, pp. 114-117.

[2] Charles Elachi, "Spaceborne radar remote sensing: Applications and techniques", 1988.

THE INVERSION OF OBJECTS BURIED IN A LAYERED EMBEDDING: THE OUTLINE OF A MULTI-PRONGED INVESTIGATION

D. LESSELIER and B. DUCHÊNE

Division Ondes

Laboratoire des Signaux et Systèmes (CNRS-SUPELEC)

Plateau de Moulon

91192 Gif-sur-Yvette Cedex

France

ABSTRACT

In this short paper investigations of wavefield inversion led by the authors and colleagues, are outlined, with strong emphasis upon frequency-diverse, aspect-limited configurations. In doing so, the interest of a cooperative framework providing the multi-expertise needed to attack these theoretically-, computationally- and experimentally-involved problems is emphasized while one concludes upon the need of carrying out reliable experiments in controlled conditions.

1. Introduction

The presentation given at the First EMSL Users' Workshop was focused on the development of methods of inversion of time-harmonic electromagnetic and acoustic wavefields in order to identify unknown geometrical and physical properties of passive objects (man-made or natural) which are found in a given plane- or cylindrically-stratified environment and which are interacting with primary wavefields generated by known active sources.

Of particular attention was the situation where the probing sources and the receivers are located in a medium different from the one which contains the probed object, and are separated from this object by one or more interfaces of the ambient layering. Thus, aspect-limited data are acquired in the measurement procedure, the object being "viewed" in part only, compensation for this lack of coverage being sought via frequency-diversity, i.e., by varying in a given band the frequency of the illuminating waves.

Here this written contribution —which is, so to speak, an extended summary of an investigation which has been going on now since more than 10 years at the Laboratoire des Signaux et Systèmes— is intended to remind the reader of a few key points of this development, without going deep into a mathematical exposé or providing numerical examples, a number of papers of easy availability—in archived journals, multi-authored books and edited proceedings save exception—by the authors and their colleagues being where detailed results should be found.

Notice that the *Review of Radio Science 1993-1996* published at the time of the 1996 URSI General Assembly incorporates one chapter by the authors—among the three granted to the Commission B "Fields and Waves"—which is devoted to a critical review of the state-of-the-art in the wavefield inversion of buried objects and to which one can be also referred [Lesselier and Duchêne, 1996].

2. The present-day cooperative framework

The above investigation is presently conducted within a broad multi-disciplinary cooperative research framework which provides us with a multiple high-level expertise and allows a

medium (the layer in which the object is assumed to be found) is retrieved by Fourier inversion from exact or approximate values of its Fourier transform in the wavenumber domain (the spectral or K -space). These values can be collected since they are proportional to those of the Fourier transform of the measurement data acquired on a line (2-D case) or a plane (3-D case) placed parallel to the interfaces of the layered environment in the same medium as the one containing the excitation sources —this is in effect a result of the so-called Fourier Diffraction Slice Theorem. Then, varying the frequency of the probing waves (this is the frequency-diversity mode of operation) or their position with respect to the object and/or the measurement line(s) or surface(s) (aspect-diversity) provides the multi-view coverage required to fill in the K -space —back-propagation concepts readily extend this technique of “coherent superimposition of holograms” to the case of non-linear or non-planar measurement zones.

The above analysis holds for lossless media and when first-order linearizing assumptions are made in the modeling of the field (save exception, the Born approximation is employed, the field u in the object domain being equated to the incident field u_{inc} existing in its absence). And increasing discrepancies therefore occur when such assumptions are less and less satisfied —typically due to attenuation in the materials investigated, multiple scattering between the object and its environment and between the constituting parts of the object themselves, electromagnetic wavefield depolarization in 3-D bounded objects, variations of density in fluid acoustics and mode conversion in elasticity [Lesselier *et al.*, 1987]. Indeed, the Fourier transform of the data set is now linked to the Fourier transform of the fictitious sources J (said to be) induced in the domain of the object and which as is well-known depend upon the object function C in a strongly nonlinear fashion.

Note also that, as is expected, lack of information in the K -space due to limited viewing of the object results in the distortion of the retrieved maps of the object function, and in the case of reflection mode data as considered here, we obtain at best a high-pass filtered version of the object geometry unless suitable priors yield the low-wavenumber spectrum.

Furthermore, note that what is done in this diffraction tomographic solution method is but to solve in an appropriate (Fast-)Fourier setting the so-called observation or data integral equation which links the unknown induced sources (reduced to the object function C times the incident field u_{inc} when linearizing assumptions are made) to the observed data. (We may refer to [Chew *et al.*, 1994] for a discussion of the inverse *source* problem of finding J as a possible first step towards the solution of the inverse *scattering* problem of finding C .)

The approach has been applied to many situations in both scalar cases (2-D TM electromagnetics, 2-D and 3-D fluid acoustics) and vector ones (3-D electromagnetics), and has been proved effective if one is careful enough to account for the fact that save in an idealistic low-contrast configuration the output is a qualitative representation of the unknown object. Computationally fast inversion algorithms are obtained in general, and a large amount of data can be handled due to the systematic use of FFT. As for robustness with respect to data and model errors, it is generally observed being fairly good, with somewhat better results obtained from experimental data when available than from synthetic ones.

Typical examples of such a reconstruction of buried objects are found in [Duchêne *et al.*, 1987, 1989] in fluid ultrasonics for 2-D objects whose dimensions are of the order of the wavelength in their embedding —the resonance domain— while we may also refer to an earlier study of microwave imaging by [Chommeloux *et al.*, 1986]. Both microwave and acoustic reconstructions of 2-D and 3-D bounded objects are discussed in [Tabbara *et al.*, 1988] (the results are given for a free-space and a half-space embedding, in a unified framework) and in [Chommeloux *et al.*, 1992] (the emphasis is on buried objects only). Attenuation-matched extensions of the previous schemes have been developed for the eddy current testing of damaged metal half-spaces in [Zorgati *et al.*, 1991] while tools that may allow us to overcome, via fictitious imaginary frequencies, the strongly penalizing skin effect in metal are studied in [de Oliveira Bohbot *et al.*, 1994].

Obviously when linearizing assumptions are enforced the resulting observation equation can be handled by other means. This has been mostly considered in eddy current testing. Generalized inversion techniques are discussed in [Zorgati *et al.*, 1992], the potential of fast Kalman filtering being particularly noted therein, and a panorama of advances in methods of solution is presented in [Brouaye *et al.*, 1995], with attention put mostly on binary objects, i.e., whose object function C only takes two values, say, 0 and 1, at any space point \underline{r} .

In this binary case, inversion by simulated annealing with incorporation of constraints of connectivity and size on the distribution of the black-and-white pixels which in effect are now representing the object is studied in detail in [de Oliveira Bohbot *et al.*, 1996]. Also the optimal inversion of the Fourier-Laplace transforms to which the observation equation can be reduced in eddy current testing is possible via eigenfunction expansions in the K -space and related means as is exemplified in [Litman *et al.*, 1995].

Furthermore, “new” approaches may reveal of interest in the case of the buried binary object. Preliminary investigations of wavelet-vaguelette decomposition and of neural network techniques did not seem as successful as it was hoped for, e.g., see [Brouaye *et al.*, 1995], due, respectively, to the non-dilational invariance of the integral operator and to the severe ill-posedness of the reconstruction. But the mathematically-involved level-set method (the boundary of the object is the level zero of a real-valued function $\phi(\underline{r}, t)$, and the hypersurface is made to evolve vs. t), presently under investigation, appears able to track down quite successfully the motion of the level curve when reducing the value of an error functional chosen to be characteristic of the fit of the solution to the data.

4. Nonlinearized schemes

As indicated before, linearizing assumptions reduce the problem at hand to the one of solving an observation equation. When they fail it is necessary to simultaneously consider this observation equation and the coupling or state integral equation which relates the field u in the object, via the induced sources J , to itself and to the object function C for a given u_{inc} .

The inversion problem is now nonlinear while ill-posedness obviously remains, or sharpens. (Notice that a thorough study of a fast numerical solution of the corresponding forward scattering problem is developed in [Lesselier and Duchêne, 1991].) Up until now most of our effort has been devoted to the nonlinearized iterative Modified Gradient Method (henceforth, MGM) and to extending it to the case of buried binary objects.

Detailed discussions of the binary MGM and many numerical examples are found in [Souriau *et al.*, 1996], three applications being dealt with therein from exact and noisy synthetic data: eddy current testing of defects in conductive materials, low frequency imaging of metal objects in water, ultrasonic reconstruction of inclusions in fluid media; while in [Kleinman *et al.*, 1997] the MGM and several of its variants and extensions are given a common framework and are illustrated in a number of specific realizations representing different physical situations, different priors on the object, and consequently different constraints imposed during its reconstruction.

Classically in the MGM method, one operates as follows once observed that in practice two (related) unknowns show up, the field u and the object function C . First, two residual errors are defined, one in satisfying the observation equation and the other in satisfying the coupling equation, for a given measurement configuration. Then, a weighted summation upon all such configurations (i.e., vs. frequency, incidence, etc.) of the norms of these residuals yields an error functional which is to be minimized with respect to the unknown field u and to the unknown object function C in a prescribed test domain. The minimization is carried out by iteratively constructing a sequence of approximations $\{C_m(\underline{r}), u_m(\underline{r})\}$ from a reasonable choice of starting functions (e.g., obtained by backpropagation of the data from the measurement line or surface onto the test domain).

This sequence is generated according to a somewhat simple update strategy which sees u_m and C_m separately updated in conjugate-gradient directions, the gradient of the error functional considered in this operation being either its gradient with respect to u_m , C_m being kept constant, or the converse. The updating parameters (the length of the displacement to the $(m + 1)$ th iterates along the updating directions that are calculated for the m th iterates) are then determined simultaneously so as to reach a local minimum of the error functional.

As for the effectiveness of the binary MGM, it is related to the appropriate introduction of a cooling parameter θ . This real-valued parameter is defined in order to transform the search of the binary object function $C(\underline{r})$ (in effect, a characteristic function valued at 0 or 1 at any given \underline{r}) into a search of a new object function $C(\tau)$ which is allowed to vary continuously between 0 and 1, the variable τ being a real-valued function of position \underline{r} .

Therefore, the functional derivatives with respect to the object function that are obviously needed in the MGM machinery now exist, and a standard MGM can be applied, the functions to update being the field u and the variable τ . When a stable result is reached in so doing, which can be seen as finding a map whose gray pixels are graded according to the value reached by τ , decreasing the θ parameter pushes the values of the object function either towards 0 at negative τ or towards 1 at positive τ . And the inversion is started again from the resulting “sharper” map, and so on until convergence.

Note that the map obtained when changing θ may not correspond to a lower value of the error functional but that in practice, once a few iterations are carried out, the error functional reached is generally of lesser magnitude. And as a matter of fact much sharper images of the object are retrieved with this method than with the standard MGM, the binary version providing us with a “more optimal” solution in the sense that among all possible solutions the “best solution” —associated with the least number of gray pixels— is sorted out.

The above studies have been starting from domain-integral formulations of the wavefield obtained by suitable application of the Green’s theorem and therefore, they are valid for inhomogeneous objects —so, in the case of a perfectly conducting object, this requires us to model the object boundary by a thin layer of strongly conductive cells whose thickness is of a few skin depths.

Similarly, application of the Green’s theorem in the case of homogeneous objects leads us to boundary-integral formulations of the wavefield, which reduces the inversion problem to a reconstruction of the contour (a line or a surface) of the unknown object, taking for granted that the contrast of this object with respect to its environment is prescribed beforehand (in effect, that the boundary condition, of the Dirichlet or Neumann kind for impenetrable objects, and transmission conditions for a penetrable object, is known).

Note that using contour integrals instead of domain integrals reduces the dimensionality of the forward-scattering problem (solving the coupling equation provides the wavefield on the contour from which the wavefield everywhere follows by contour integration). However, the solution of the inversion problem now requires an effective strategy (this is already the case with the previously introduced level-set method) in order to deal with the topological evolution of such a boundary —in particular the splitting of a given object into two disjoint parts is very challenging while it is not an issue at all when the wavefield is described via domain-integral formulations and the object is but a superimposition of pixels.

A good example of the pros and cons of such an investigation, led by means of a complete family method, is found in the case of the shape retrieval of an obstacle immersed in shallow water from near-field or far-field scattered data analyzed by [Rozier *et al.*, 1996, 1997]. Particular constraints occur due to the fact that modes are propagated in the resulting waveguiding structure and only finitely many modes are observed in the farfield, which, in turn, means that key mathematical questions as unicity of the solution are far from being solved yet. But fairly good results are obtained even in a noisy environment for a variety of object contours once it is assumed that an isolated star-shaped smooth object is sought; and it is hoped that applications of a similar method to the retrieval of an object buried in a half-space and illuminated/observed from the above half-space will be of interest.

5. Experiments

The need of reliable experimental data in controlled situations that are within the scope of the actual and forthcoming inversion schemes is evident. So far only two sets of experiments have been conducted and/or exploited.

The first ones, most of them carried out in the late 80's - early 90's, provided us with data for the purpose of testing diffraction tomographic algorithms in free-space and (much less frequently) in limited-space geometries, many examples of which are found in a series of papers where microwave, eddy current and ultrasonic wavefields are of concern [Duchêne *et al.*, 1988; Tabbara *et al.*, 1988; Chommeloux *et al.*, 1992, Grassin and Duchêne, 1992]. Experiments in the context of eddy current testing and attenuation-matched diffraction tomographic imaging of defects in a metal block have also been led [Zorgati *et al.*, 1991].

The second ones, in the mid 90's, provided us with data for the main purpose of testing nonlinearized algorithms, and we should emphasize the Ipswich database designed by the Rome Laboratory, Electromagnetics and Reliability Directorate, Hanscom Air Force Base.

The database has now been available to the inversion community since two years as is illustrated by the success of the so-called "real-data" special sessions of the 1995 and 1996 IEEE AP-S Symposia and URSI Meetings, and it is further developing in range, mutually fruitful arrangements being under discussion with EMSL at the time of this writing.

Examples of results obtained by the binary version of the modified gradient algorithm are given in [Duchêne and Lesselier, 1996] and in [Duchêne *et al.*, 1997] (in the latter paper a comparison with diffraction tomographic algorithms specialized to a circular geometry of probes in the farfield of the target is found).

However so far, only free-space objects are considered in the Ipswich database and so, it is clear that carrying out similar measurements for objects embedded in a half-space as needed to get on par with the most recent theoretical and computational developments [Souriau *et al.*, 1996] is but difficult; we obviously can restrict ourselves to the viewing of only a part of the target to be retrieved, as seen in [Duchêne and Lesselier, 1996] and by other variants of the modified gradient method in [Kleinman *et al.*, 1997]. Also, data that may indeed be available for buried objects, like those of EMSL (3-D objects in a realistic ground), may still be too complicated at the present level of development of the nonlinearized schemes.

Finally, let us emphasize that the situation where obstacles are embedded in a known layered environment and where both sources and probes are on the other side of an interface has been addressed in eddy current testing of metal tubes in heat generators of nuclear power plants: the defect is effecting the wall of a circular cylinder and a set of emitting and receiving coils is displaced along the axis of the tube. Results of experimental measurements (variations of impedance of the probing coils) have been successfully compared to those calculated by a 3-D Method-of-Moments code based on an exact dyadic integral formulation of the field [Monebhurrin *et al.*, 1996], but no attempts to inversion of such experimental data have been made yet.

6. References

- F. Brouaye *et al.* [1995], "Eddy current imaging of defects in a conductive half-space as an inverse wave scattering problem: recent algorithmic advances," in *Inverse Scattering and Potential Problems in Mathematical Physics*, R. E. Kleinman *et al.* Eds., Peter Lang, Frankfurt, 17-31.
- W. C. Chew *et al.* [1994], "On inverse source method of solving inverse scattering problems," *Inv. Prob.*, **10**, 547-553.
- L. Chommeloux *et al.* [1986], "Electromagnetic modeling for microwave imaging of cylindrical buried inhomogeneities," *IEEE Trans. Microwave Theory Tech.*, **MTT-34**, 1064-1076.
- L. Chommeloux *et al.* [1992], "On the microwave and ultrasonic imaging of buried targets by diffraction tomography," in *Direct and Inverse Methods in Radar Polarimetry*, W. M. Boerner *et al.* Eds., Kluwer, Dordrecht, 1083-1104.
- B. Duchêne and D. Lesselier [1996] "On modified gradient solution methods using the binary aspect of the unknown electromagnetic parameters and their application to the Ipswich data," *Antennas Propagat. Magazine*, **38**, 45-47.
- B. Duchêne *et al.* [1987], "Acoustical imaging of 2-D fluid targets buried in a half-space: a diffraction tomography approach," *IEEE Trans. Ultrason. Ferroelect. Freq. Control*, **UFFC-34**, 540-549.
- B. Duchêne *et al.* [1988], "Experimental investigation of a diffraction tomography technique in fluid ultrasonics," *IEEE Trans. Ultrason. Ferroelect. Freq. Control*, **UFFC-35**, 437-444.
- B. Duchêne *et al.* [1989], "Acoustical imaging of 2-D fluid targets buried in a half-space. A diffraction tomography approach using line-source insonification," in *Electromagnetic and Acoustic Scattering: Detection and Inverse Problem*, C. Bourrely *et al.* Eds., World Scientific, Singapore, 111-122.
- B. Duchêne *et al.* [1997], "Inversion of the 1996 Ipswich data using binary specializations of modified gradient methods," *Antennas Propagat. Magazine*, to appear.
- P. Grassin and B. Duchêne [1992], "On the solution of a scalar inverse scattering problem: qualitative and quantitative ultrasonic imaging in fluid media," in *Inverse Problems in Scattering and Imaging*, M. Fiddy Ed., Proc. SPIE **1767**, 208-219.
- R. Kleinman *et al.* [1997], "Location and reconstruction of objects using a modified gradient approach," *Proc. Conf. Inverse Prob. Wave Propagat. Diffraction (Aix-les-Bains, 1996)*, G. Chavent and P. C. Sabatier Eds., Springer, Berlin, to appear.
- D. Lesselier and B. Duchêne [1991], "Buried 2-D penetrable objects illuminated by line sources: FFT-based iterative computations of the anomalous field," in *Application of Conjugate Gradient Methods to Electromagnetics and Signal Analysis*, T. K. Sarkar Ed., Elsevier, New York, 400-438.
- D. Lesselier and B. Duchêne [1996], "Wavefield inversion of objects in stratified environments. From backpropagation schemes to full solutions," in *Review of Radio Science 1993-1996*, R. Stone Ed.-in-Chief, Oxford Univ. Press, Oxford, 235-268.
- D. Lesselier *et al.* [1987], "Imaging inhomogeneous media by diffraction tomography techniques. Critical examination and prospects," *Inverse Problems: an Interdisciplinary Study*, P. C. Sabatier Ed., Academic Press, London, 35-49.
- A. Litman *et al.* [1995], "Mapping 2-D defects in a conductive half-space by eigenfunction expansions in K -space of Fourier-Laplace transforms," in *Nondestructive Testing of Materials*, R. Collins *et al.* Eds., IOS Press, Amsterdam, 175-183.
- V. Monebhurrin *et al.* [1996], "On the 3-D eddy current nondestructive testing of metal tubes," in *Proc. 3rd Int. Workshop Elect. Magn. Fields*, Liege, May 1996, 465-470.

R. de Oliveira Bohbot *et al.* [1994], "A diffraction tomographic algorithm for eddy current imaging from anomalous fields at fictitious imaginary frequencies," *Inv. Prob.*, **10**, 109-127.

R. de Oliveira Bohbot *et al.* [1996], "Mapping voids in a conductive half-space by simulated annealing with connectivity and size as constraints," *J. Electromagn. Waves Applic.*, **10**, 983-1004.

C. Rozier *et al.* [1996], "Optimal shape reconstruction of a perfect target placed in shallow water," in *Underwater Acoustics*, J. S. Papadakis Ed., FORTH-IACM, Crete Univ. Press, Heraklion, **1**, 27-32.

C. Rozier *et al.* [1997], "Reconstruction of an impenetrable obstacle immersed in a shallow water acoustic waveguide," in *Proc. Conf. Inverse Prob. Wave Propagat. Diffraction* (Aix-les-Bains, 1996), G. Chavent and P. C. Sabatier Eds., Springer, Berlin to appear.

L. Souriau *et al.* [1996], "A modified gradient approach to inverse scattering for binary objects in stratified media," *Inv. Prob.*, **12**, 463-481.

W. Tabbara *et al.* [1988], "Diffraction tomography: contribution to the analysis of some applications in microwaves and ultrasonics," *Inv. Prob.*, **4**, 305-331.

R. Zorgati *et al.* [1991], "Eddy current testing of anomalies in conductive materials. Part I: Qualitative imaging via diffraction tomography techniques," *IEEE Trans. Magn.*, **MAG-27**, 4416-4437.

R. Zorgati *et al.* [1992], "Eddy current testing of anomalies in conductive materials. Part II: Quantitative imaging via generalized inverse techniques," *IEEE Trans. Magn.*, **MAG-28**, 1850-1862.

Inversion algorithms for microwave imaging using different modalities and for various applications

Ch. Pichot¹, P. Lobel², C. Dourthe³, L. Blanc-Féraud² and M. Barlaud²

¹*Laboratoire d'Electronique, Antennes et Télécommunications*

²*Laboratoire Informatique Signaux et Systèmes de Sophia Antipolis
CNRS / Université de Nice-Sophia Antipolis*

250 rue Albert Einstein, Sophia Antipolis, 06560 Valbonne, France

³*Centre d'Enseignement et de Recherche en Modélisation, Informatique et Calcul
Scientifique/INRIA, 2004 route des Lucioles, B.P. 93, 06902 Sophia Antipolis, France*

ABSTRACT. This paper deals with two different inversion algorithms for Microwave Imaging. The first one involves a quantitative imaging method with single frequency excitation and multiincidence illumination and the second one a qualitative method with synthetic pulse (multifrequency mode) or real pulse (impulse mode) excitation. Transmission and reflection imaging protocols are considered depending on aiming applications : microwave imaging in the air from far-field data for target identification, microwave imaging from near-field data for Non-Destructive Testing (NDT) and medical applications, microwave tomography of buried objects for mine detection and localization, civil engineering and geophysical applications. The methods are illustrated with synthetic and experimental data. With the quantitative imaging method, an edge-preserving regularization scheme leading to a significant enhancement in the reconstructions is also proposed.

1. Introduction

The development of reconstruction algorithms for Microwave Imaging with application in the domain of NDT has gained much interest in the past fifteen years. The success of a microwave imaging system depends, among several other factors, on the processing of the probing field resulting from the interaction between microwave beams and the structure to investigate. Taking into account and compensating for diffraction effects constitutes a prerequisite for structures having dimensions of the order of the wavelength.

The nature of the inverse scattering problem is strongly nonlinear and ill-posed when quantitative imaging is requested. During the past few years, intensive studies have concerned spatial iterative reconstruction algorithms able to give an efficient solution to quantitative imaging. From an exact integral representation of the EM field, the moment method is applied to generate matrix relations. Iterative methods such as Newton-Kantorovich (NK) [1, 2], Conjugate Gradient (CG) [3] and Modified Gradient (MG) [4–6] methods are used to minimize a cost functional. With the gradient method, several directions have been studied including a backpropagation direction, a gradient direction and a Polak-Ribière conjugate gradient direction. Different regularization schemes have also been investigated. Starting from the standard Tikhonov regularization with identity operator or with gradient operator in the NK or CG algorithm, a new regularization procedure has been derived using Edge-Preserving (EP) potential functions [7, 8]. This regularization scheme has been implemented in the CG method and the enhancement is illustrated throughout some examples with noisy synthetic and experimental data.

Qualitative imaging algorithms belong to the so-called spectral methods [9–12] and are based on Diffraction Tomography. Their main interest lies on quasi-real time reconstruction due to the use of Fast Fourier Transforms. For weak scatterers (Born approximation), they yield the complex permittivity distribution profile but, in the general case, the image is more or less related to the induced currents generated inside the inhomogeneities.

Two algorithms are proposed. The first one is developed for quantitative imaging using single frequency excitation and for transmission imaging protocol in multiincidence illumination. The second algorithm was developed for qualitative imaging methods, using synthetic pulse (multifrequency mode) or real pulse (impulse mode) excitation for reflection imaging protocol of buried objects.

Different configurations of practical interest have been studied for various applications of microwave imaging with the two qualitative and quantitative algorithms using synthetic data as well as experiments.

2. Non-buried object

Let assume a cylindrical object characterized by a relative complex permittivity $\epsilon(r)$ contained in a bounded region \mathcal{D} and illuminated successively by different incident TM plane waves e_l^I , $l \in [1, L]$. Depending on the aimed application, the receivers are located in the domain \mathcal{S} either in the near or far field region. For each excitation l , and for $r \in \mathcal{D}$, the forward scattering problem may be formulated as the following domain integral equation

$$\begin{aligned} e_l(r) &= e_l^I(r) + \int_{\mathcal{D}} k_0^2 c(r') e_l(r') G(r - r') dr', \quad r \in \mathcal{D} \\ &= e_l^I(r) + G^{\mathcal{D}} c e_l(r), \quad r \in \mathcal{D} \end{aligned} \quad (1)$$

and integral representation for the scattered field

$$\begin{aligned} e_l^S(s_{lm}) &= \int_{\mathcal{D}} k_0^2 c(r') e_l(r') G(s_{lm} - r') dr', \quad s_{lm} \in \mathcal{S} \\ &= G^{\mathcal{S}} c e_l(s_{lm}), \quad s_{lm} \in \mathcal{S} \end{aligned} \quad (2)$$

with complex contrast function $c(r) = \epsilon(r) - 1$ and k_0 is the wavenumber of background medium and where $G^{\mathcal{D}}$ and $G^{\mathcal{S}}$ are two integral operators mapping respectively $L^2(\mathcal{D})$ (square integrable functions in \mathcal{D}) into itself, and $L^2(\mathcal{D})$ into $L^2(\mathcal{S})$, and involving the 2D free space Green's function

$$G(r - r') = \frac{i}{4} H_0^{(1)}(k_0 |r - r'|) \quad (3)$$

The direct problem is solved using the moment method (MoM) with pulse basis functions and point matching, which transforms the integral equations (1) and (2), into matrix equations. The rectangular image (or test domain) containing the region \mathcal{D} is discretized into $N = N_{lin} \times N_{col}$ elementary square cells.

Solving the inverse scattering problem leads to reconstruct from the resulting matrix system, the complex contrast of the object, while the incident field, the scattered field, and the Green's matrices are known. We present in the following sections of this paper, three different iterative methods which allow to reconstruct the contrast.

2.1 CONJUGATE GRADIENT (CG) METHOD

2.1.1 General algorithm. In this method, we choose to minimize a unique functional, resulting from the discretized versions of (1) and (2). This functional is nonlinear and is written as

$$F(C) = \sum_{l=1}^L \|\rho_l(C)\|_S^2 \quad (4)$$

where $\rho_l(C) = E_l^S - G^S C \mathcal{L}(C) E_l^I$ and $\mathcal{L}(C) = (I - G^D C)^{-1}$.

We use the following iterative procedure on C ($N \times N$ diagonal matrix containing c) to minimize (4) :

$$C^{i+1} = C^i + \alpha^i D^i \quad (5)$$

D^i is the Polak-Ribière conjugate gradient direction and α^i a complex parameter as defined in [3].

2.1.2 Edge-Preserving (EP) regularization. For highly contrasted objects, and/or face with noisy corrupted data, the inverse scattering problem becomes more ill-posed. The introduction of some *a priori* informations in (4) is needed in order to reconstruct a regular solution. We choose to model the solution as a piecewise constant profile, and the cost functional (4) becomes :

$$F_{EP}(C) = F(C) + \sum_{p=1}^{N_{lin}} \sum_{q=1}^{N_{cot}} \lambda_R^2 \varphi \left(\frac{\|\text{Re}(\nabla c)_{p,q}\|}{\delta_R} \right) + \sum_{p=1}^{N_{lin}} \sum_{q=1}^{N_{cot}} \lambda_I^2 \varphi \left(\frac{\|\text{Im}(\nabla c)_{p,q}\|}{\delta_I} \right) \quad (6)$$

When dealing with the reconstruction of a complex matrix, we consider the real part and the imaginary part of the contrast as independent in the regularization scheme. As a matter of fact, there is no link between the real and the imaginary part of the permittivity, and the EP regularization is applied separately on the real and the imaginary part of the contrast. The weighting parameters λ_R and λ_I fix the influence of the regularization term versus the error matching the scattered field. The parameters δ_R and δ_I fix the level on the gradient norm above which a discontinuity is preserved, and under which it is smoothed. The regularizing function φ is real and defined on $[0, +\infty[$. We propose to use a class of φ functions like the ones shown in table I. They are defined to perform an isotropic smoothing in the homogeneous areas of the image (corresponding to small gradients), while preserving edges (corresponding to high gradients) [13–17]. Such a class of functions has been theoretically defined in [7, 16]. Basically, two main conditions must be satisfied :

- i)* φ must be quadratic when $t \rightarrow 0$ (in order to apply an isotropic smoothing on the homogeneous areas¹).
- ii)* φ must be linear² or underlinear³ when $t \rightarrow \infty$ (in order to preserve edges).

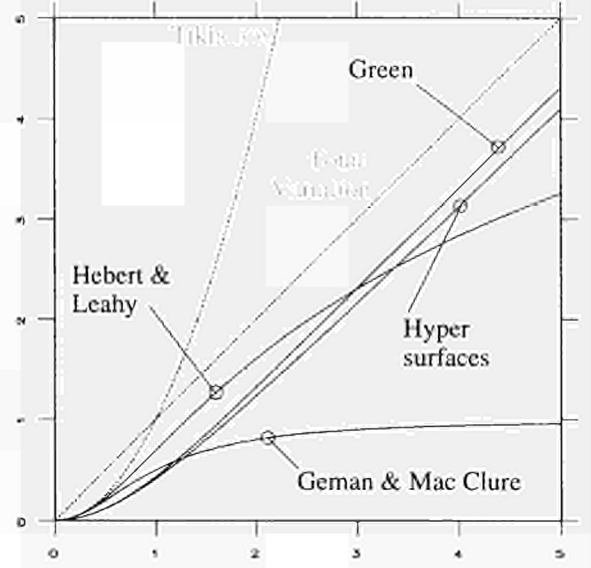
¹In this case, the regularization is a Tikhonov-like one.

²In this case, the regularization is a Total Variation-like one [18, 19].

³In this case, an edge-enhancement procedure is applied on the image [20].

TABLE I SUMMARY OF SOME φ FUNCTIONS

Name of the φ function	$\varphi(t)$
Geman & Mc. Clure	$\frac{t^2}{1+t^2}$
Hebert & Leahy	$\log(1+t^2)$
Green	$\log[\cosh(t)]$
Hyper surfaces	$\sqrt{1+t^2} - 1$



The regularization term in (6) is non quadratic with respect to c , and introduces an additional nonlinear problem in the resolution scheme. A fundamental property of the φ functions can be applied to reformulate $\text{Min}_C F_{EP}(C)$ into $\text{Min}_{C, b_R, b_I} F_{EP}^\dagger(C, b_R, b_I)$ defined by [7, 17] :

$$F_{EP}^\dagger(C, b_R, b_I) = F(C) + \lambda_R^2 \sum_{p=1}^{N_{ig}} \sum_{q=1}^{N_{col}} (b_R)_{p,q} \left\| \frac{\text{Re}(\nabla c)_{p,q}}{\delta_R} \right\|^2 + \psi((b_R)_{p,q}) + \lambda_I^2 \sum_{p=1}^{N_{ig}} \sum_{q=1}^{N_{col}} (b_I)_{p,q} \left\| \frac{\text{Im}(\nabla c)_{p,q}}{\delta_I} \right\|^2 + \psi((b_I)_{p,q}) \quad (7)$$

The variables b_R and b_I (each one belongs to $]0, 1[$) map respectively the discontinuities of the real and imaginary part of the object. Their value at the point (p, q) tends towards 0 if this point belongs to an edge of the image, and equals 1 if this point belongs to an homogeneous area. The function ψ is convex and analytically defined from the function φ . The non quadratic minimization of (6) with respect to c , is replaced by the half-quadratic minimization of (7) (quadratic in c when (b_R, b_I) is fixed) with respect to (c, b_R, b_I) . The following alternate minimization procedure is used :

- i)* when b_R and b_I are fixed, the regularization term is quadratic in c , and the basic minimization of (4) is not influenced by the regularization term. Of course, new values for the α parameter and for the gradient direction must be calculated [7, 21],
- ii)* when c is fixed, the minima \hat{b}_R and \hat{b}_I are unique and given for each point (p, q) by the analytical expressions [16] :

$$(\hat{b}_R)_{p,q} = \frac{\varphi' \left(\frac{1}{\delta_R} \|\text{Re}(\nabla c)_{p,q}\| \right)}{\frac{2}{\delta_R} \|\text{Re}(\nabla c)_{p,q}\|} \quad \text{and} \quad (\hat{b}_I)_{p,q} = \frac{\varphi' \left(\frac{1}{\delta_I} \|\text{Im}(\nabla c)_{p,q}\| \right)}{\frac{2}{\delta_I} \|\text{Im}(\nabla c)_{p,q}\|} \quad (8)$$

More details about the minimization procedure can be found in [7, 16, 21].

2.2 RECONSTRUCTIONS FROM SYNTHETIC AND EXPERIMENTAL DATA

2.2.1 Reconstruction from synthetic data. We proposed a reconstruction of the permittivity profile of the synthetic object proposed in [19]. The test domain \mathcal{D} is a square 3λ by 3λ , where λ is the wavelength in the background medium. The simulated object is discretized into 29×29 subsquares, and the surface \mathcal{S} enclosing \mathcal{D} is a circle of radius 9λ . A set of 29 transmitters-receivers is uniformly located on it, and while each transmitter, acting like a line source, illuminates the object, the whole set of receivers collect the scattered field ($L = M = 29$).

The object under investigation, is made by two distinct homogeneous square cylinders placed in free space, of diameter $\frac{1}{4}\lambda$, with $\frac{1}{4}\lambda$ separation and relative permittivity $\epsilon_r = 1.8$, ($\text{Im}(\epsilon_r) = 0$). We corrupt the simulated scattered data with an additive white Gaussian noise of about 10% of the maximum value of these data, and we try to reconstruct the original profile.

We show in Figure 1, a comparison between the results obtained without any regularization and with the new Edge-Preserving (EP) regularization scheme. We also show a result obtained after the well known Tikhonov regularization. All these results were obtained after 150 iterations. The enhancement is obvious : with the EP regularization, the two square cylinders are perfectly reconstructed while the noise peaks (which are visible in the reconstruction obtained without any regularization) completely disappear from the background medium. One can see that with the solution obtained after the Tikhonov regularization, even if the noise peaks also disappear, the result becomes too smoothed. For the EP regularization, we use the Geman and Mac Clure φ function, which fits very well for objects with sharp edges and allows edge enhancement (see [20]).

2.2.2 Reconstructions from experimental data. We present here the results obtained from the experimental Ipswich⁴ far-field data [3, 8]. The axis of the targets is oriented along the z-axis. The bistatic scattering measurements at 10.0 GHz were made in a plane perpendicular to this axis⁵. The scattered fields of the metallic cylinder (Figure 2) and strip (Figure 3) were collected for eight incident angles of $\{0^\circ, 5^\circ, 10^\circ, 15^\circ, 20^\circ, 45^\circ, 60^\circ, 90^\circ\}$, over the observation sector $0 \leq \theta_S < 360^\circ$, with a sample spacing $\Delta\theta_S = 0.5^\circ$, while the scattered fields for the dielectric object (Figure 4) were collected for six incident angles $\theta_I \in \{0^\circ, 60^\circ, 120^\circ, 180^\circ, 240^\circ, 300^\circ\}$, over an observation sector $\theta_I + 180^\circ \leq \theta_S \leq \theta_I + 375^\circ$, with a sample spacing $\Delta\theta_S = 0.5^\circ$.

The two metallic objects (cylinder and strip, Figures 2 and 3) are reconstructed after 20 and 30 iterations respectively. An initial guess based on a backpropagation scheme was used for the two reconstructions, as described in [3].

A comparative study for the polystyrene square cylinder has been made on results obtained at the same degree of convergence without any regularization, with a Tikhonov regularization and with our EP regularization scheme (Figure 4). In the different results, no initial guess were used i.e. the starting value is zero contrast. The reconstruction without regularization, shows a blurred profile with a coarse shape description. The use of a Tikhonov regularization smoothes the profile and the edges are not preserved. The new

⁴Measured data provided by Rome Laboratory, Electromagnetics & Reliability Directorate, 31 Grenier Street, Hanscom AFB, MA 01731-3010.

⁵The complete Ipswich Test Range system developed at *Rome Laboratory* is described in [22]

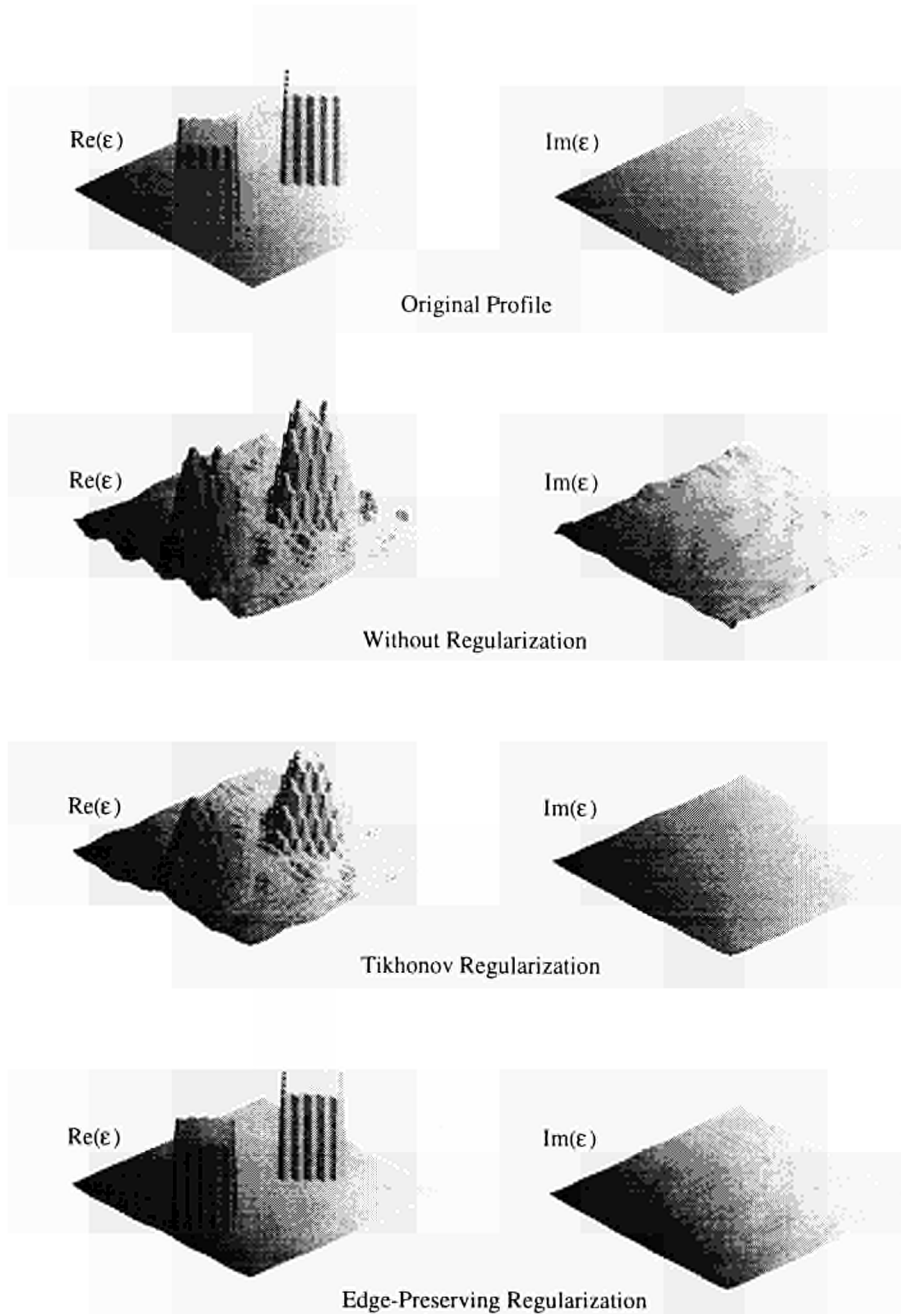


Fig. 1. Reconstructions of a synthetic dielectric object

regularization scheme improves the performance of the conjugate gradient algorithm : the edges are clearly preserved while the homogeneous areas are smoothed [8].

For all these results, we reconstructed objects divided into about 850 square cells, and the computation time on a DEC-Alpha workstation 3000 was of about 14 minutes for each iteration.

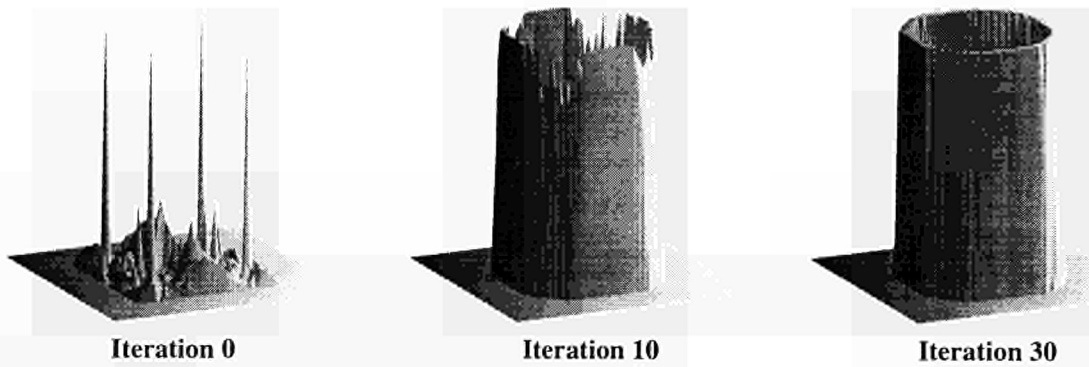


Fig. 2. Reconstruction of the metallic cylinder

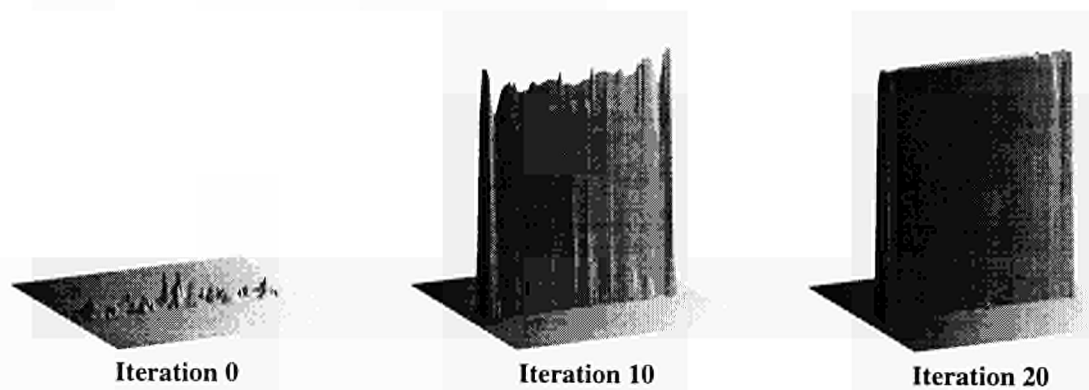


Fig. 3. Reconstruction of the metallic strip

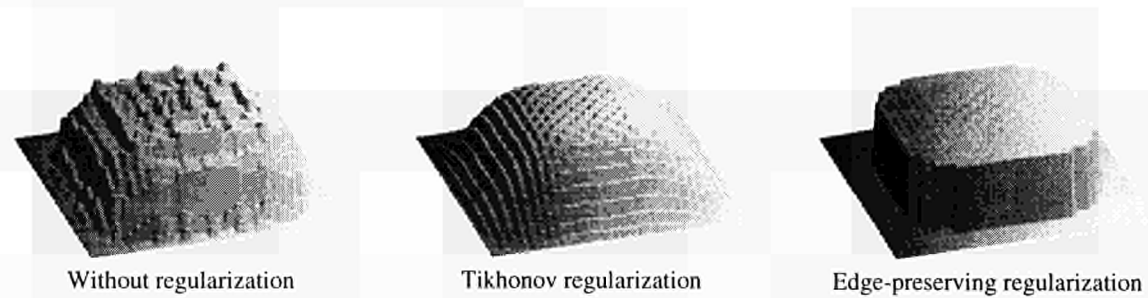


Fig. 4. Reconstructions of the polystyrene square cylinder

3. Buried object

3.1 DESCRIPTION OF THE ALGORITHM

The approach described here is based on Diffraction Tomography [23, 24]. This technique processes the backscattered field signal generated by the buried inhomogeneities and measured over a probing area for computing a tomographic image of the ground. The method originally developed for multifrequency and plane illumination (10) has been extended, recently, for time pulse illumination and for arbitrary spatial waveform of the emitting

antenna. The main advantages of such a method is the use of explicit formulas (based on the Fourier Diffraction theorem) for solving the imaging problem and to take profit of Fast Fourier transforms to implement the reconstruction algorithms on PC's allowing rapid image display. Presence of stratifications can be taken into account in the reconstruction algorithm when a *priori* information on them is available.

For instance, this imaging technique can use a synthetic pulse (multifrequency or swept frequency mode) as well as a real pulse (impulse mode) transmitted through a broadband antenna in a reflecting mode configuration. The backscattered electric field generated by the buried inhomogeneities is measured at various locations with a receiving antenna for different positions of the emitting antenna. For detecting various types of mines (anti-tank, anti-personnel...), the frequency used in the applications is from 500 MHz up to a few GHz.

A one-to-one relationship via Fourier transforms relates the scattered field \tilde{E}_z^D measured at various locations x_S and at a height y_1 above the interface air/soil to the object complex permittivity within the Born's approximation, using the so-called Fourier Diffraction theorem [24] which is a generalization of the Radon Projection theorem used in X-rays tomography. This relationship can be extended, for the general case, to the mean equivalent current distribution K inside the inhomogeneities [24]. For each angular frequency ω we can define

$$\begin{cases} \alpha = \nu - \eta \\ \beta = \frac{-1}{2\pi}(\tilde{\gamma}_3 + \tilde{\xi}_3) \\ \tilde{\gamma}_3 = \sqrt{\omega_3^2 \mu_0 \epsilon_3 - 4\pi^2 \nu^2} \\ \tilde{\xi}_3 = \sqrt{\omega_3^2 \mu_0 \epsilon_3 - 4\pi^2 \eta^2} \end{cases} \quad (9)$$

and then we obtain

$$\widehat{K}(\alpha, \beta) = \mathcal{F}(\nu, \eta, y_1) \widehat{\tilde{E}_z^D}(\nu, \eta, y_1) \quad (10)$$

where $\widehat{K}(\alpha, \beta)$ and $\widehat{\tilde{E}_z^D}(\nu, \eta, y_1)$ denote the 2D spatial Fourier transforms of $K(x, y)$ and $\tilde{E}_z^D(x, x_S, y_1)$, respectively, while \mathcal{F} represents a frequency domain filter depending directly on the plane wave spectrum $A_1(\eta, \omega)$ of the emitting antenna in the air and on the associated transmission coefficient $T_\perp(\eta, \omega)$ of each plane wave in the soil taking into account that the soil is a homogeneous or multilayer medium.

The reconstruction algorithm is based on this relationship (10) mapping the 2D Fourier transform of the measured backscattered field data onto arcs defined in the Fourier space by

$$(\alpha + \eta)^2 + \left(\beta + \frac{\tilde{\xi}_3}{2\pi}\right)^2 = \left(\frac{k_3}{2\pi}\right)^2 \quad (11)$$

where the spectral variables are satisfying the following conditions

$$\nu, \eta \in \left[-\frac{\text{Re}(k_1)}{2\pi}; \frac{\text{Re}(k_1)}{2\pi}\right] \quad \nu, \eta \text{ real} \quad (12)$$

Tomograms (2D slices of the ground) are obtained after taking a 2D spatial inverse Fourier transform (Figure 5). This method could be generalized to a surface probing of the backscattered field for displaying 3D images of the ground.

3.2 NUMERICAL RESULTS

Let us consider in Figure 6, a dielectric buried object (permittivity $\epsilon_r = 3$, conductivity $\sigma = 0 \text{ S.m}^{-1}$) of size $45 \times 28 \text{ cm}^2$ embedded in various soils at a depth of 30 cm. The working frequency band is $[0.5 - 2.5] \text{ GHz}$. Four different types of soil are considered :

- Dry sandy soil ($\epsilon_{r\text{ext}} = 3.7$ (a) and $\epsilon_{r\text{ext}} = 6$ (b); $\sigma_{\text{ext}} = 4.1 \cdot 10^{-3} \text{ S.m}^{-1}$).
- Medium soil ($\epsilon_{r\text{ext}} = 10$; $\sigma_{\text{ext}} = 7 \cdot 10^{-3} \text{ S.m}^{-1}$) (c).
- Wet clay soil ($\epsilon_{r\text{ext}} = 20$; $\sigma_{\text{ext}} = 4 \cdot 10^{-2} \text{ S.m}^{-1}$) (d).

We have used in these simulations a space and time Gaussian pulse for the incident wave (800 MHz for the center frequency). Contour plots of polarization currents induced in the buried objects are given in the reconstructed images. One can note a slight deterioration in the image reconstruction with a shift of the back side towards the front side of the buried object when the permittivity of the soil is increasing (from the dry sandy soil to the wet clay soil).

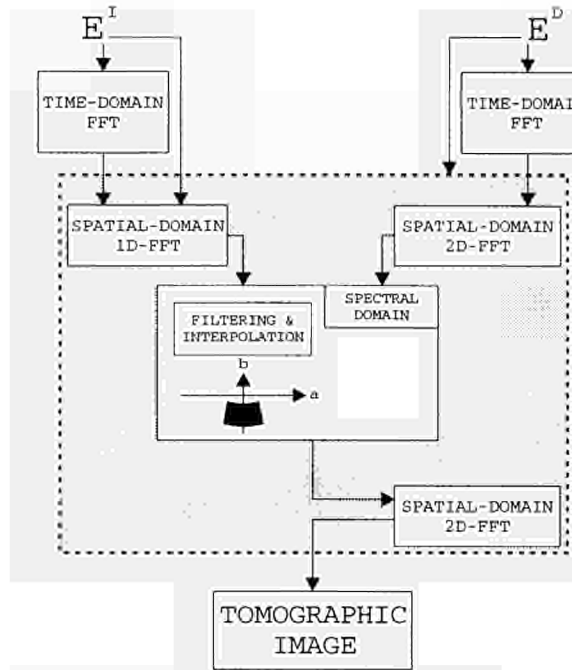


Fig. 5. Flow chart of imaging algorithm

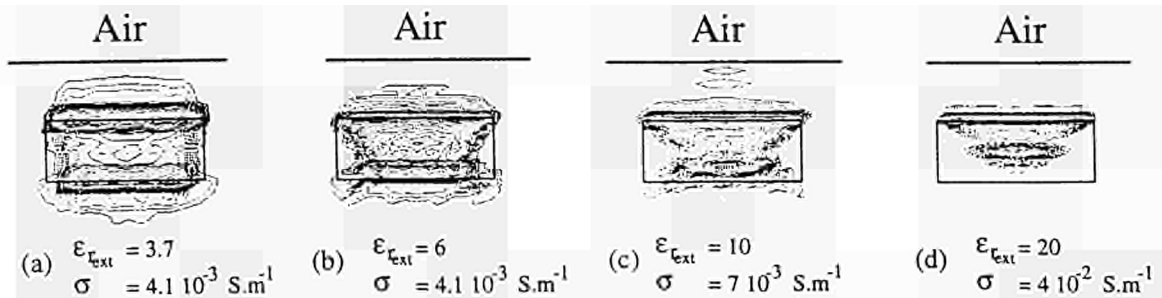


Fig. 6. Buried object reconstructions versus soil characteristics

- [6] R.E. Kleinman and P.M. van den Berg, "Two-dimensional location and shape reconstruction", *Radio Science*, vol. 29, pp. 1157–1169, 1994.
- [7] P. Lobel, L. Blanc-Féraud, Ch. Pichot, and M. Barlaud, "A new regularization scheme for inverse scattering," Research Note 95-72, Laboratoire Informatique Signaux et Systèmes de Sophia Antipolis, December 1995, Submitted to *Inverse Problems*.
- [8] P. Lobel, Ch. Pichot, L. Blanc-Féraud, and M. Barlaud, "Conjugate Gradient Algorithm With Edge-Preserving Regularization for Image Reconstruction from Experimental Data," in *IEEE AP-S/URSI International Symposium*, Baltimore, Maryland, USA, July 1996, vol. 1, pp. 644–647, Invited paper.
- [9] A.J. Devaney, "Geophysical diffraction tomography", *IEEE Trans. Geosci. Remote Sensing*, vol. GE-22, pp. 3–13, 1984.
- [10] Ch. Pichot, L. Jofre, G. Peronnet, and J. Ch. Bolomey, "Active microwave imaging of inhomogeneous bodies", *IEEE Transactions on Antennas and Propagation*, vol. AP-33, pp. 416–425, 1985.
- [11] W. Tabbara, B. Duchêne, Ch. Pichot, D. Lesselier, L. Chommeloux, and N. Joachimowicz, "Diffraction tomography: contribution of the analysis of some applications in microwaves and ultrasonics", *Inverse Problems*, vol. 4, pp. 305–331, 1988.
- [12] K.J. Langenberg, "Introduction to the special issue on inverse problems", *Wave Motion*, vol. 11, pp. 99–112, 1989.
- [13] S. Geman and D.E. Mc Clure, "Bayesian image analysis : an application to single photon emission tomography," in *Proc. Statist. Comput. Sect.*, Washington DC, 1985, Amer. Statist. Assoc., pp. 12–18.
- [14] T. Hebert and R. Leahy, "A generalized EM algorithm for 3-D Bayesian reconstruction from Poisson data using Gibbs priors", *IEEE Transactions on Medical Imaging*, vol. MI-8, no. 2, pp. 194–202, June 1989.
- [15] P. Perona and J. Malik, "Scale-space and edge detection using anisotropic diffusion", *IEEE Transactions on Pattern Analysis and Machine Intelligence*, vol. PAMI-12, no. 7, pp. 629–639, July 1990.
- [16] P. Charbonnier, L. Blanc-Féraud, G. Aubert, and M. Barlaud, "Deterministic Edge-Preserving Regularization in Computed Imaging", *IEEE Transactions on Image Processing*, vol. 5, no. 12, December 1996.
- [17] S. Geman and G. Reynolds, "Constrained restoration and the recovery of discontinuities", *IEEE Transactions on Pattern Analysis and Machine Intelligence*, vol. PAMI-14, no. 3, pp. 367–383, March 1992.
- [18] R. Acar and C.R. Vogel, "Analysis of bounded variation penalty methods for ill-posed problems", *Inverse Problems*, vol. 10, no. 6, pp. 1217–1229, December 1994.
- [19] P.M. van den Berg and R.E. Kleinman, "A total variation enhanced modified gradient algorithm for profile reconstruction", *Inverse Problems*, vol. 11, pp. L5–L10, 1995, Letter to the editor.
- [20] L. Blanc-Féraud, P. Charbonnier, G. Aubert, and M. Barlaud, "Nonlinear image processing : Modeling and fast algorithm for regularization with edge detection," in *Proc. IEEE-ICIP*, Washington, USA, October 1995, pp. 474–477.
- [21] P. Lobel, L. Blanc-Féraud, Ch. Pichot, and M. Barlaud, "Technical development for an edge-preserving regularization method in inverse scattering," Research Note 95-73, Laboratoire Informatique Signaux et Systèmes de Sophia Antipolis, December 1995.
- [22] M. G. Coté, "Automated Swept-Angle Bistatic Scattering Measurements Using Continuous Wave Radar", *IEEE Transactions on Instrumentation and Measurement*, vol. IM-41, no. 2, pp. 185–192, April 1992.
- [23] L. Chommeloux, Ch. Pichot, and J.Ch. Bolomey, "Electromagnetic modeling for microwave imaging of cylindrical buried inhomogeneities", *IEEE Transactions on Microwave Theory and Techniques*, vol. MTT-34, no. 10, pp. 1064–1076, 1986.
- [24] J.Ch. Bolomey and Ch. Pichot, "Microwave tomography: from theory to practical imaging systems", *Int. J. Imaging Syst. Technol.*, vol. 2, pp. 144–156, 1990.

LOCALISATION AND IDENTIFICATION OF ANTI-PERSONNEL MINES: THE JRC STUDY REPORT

A. J. SIEBER
Advanced Techniques Unit, SAI, JRC
21020 Ispra (VA)
Italy

ABSTRACT. This paper reports the results of a study on the state of knowledge for the localisation and identification of land mines which has included the organisation of a workshop attended by international experts, as groundwork for the study. On the basis of the workshop conclusions, literature survey and detailed technical discussions with qualified research institutes and companies in the EU countries, the investigation team has proposed a European R&D program aimed at developing a prototype system and demonstrating its functions and operation in a mine-infested area.

1. Introduction

The JRC study report on the state of knowledge for the localisation and identification of land mines has now been published [1]. The study was commissioned by the German Bundesministerium *BMBF*. One part of the commission entailed the organisation of a workshop attended by international experts, as groundwork for the study. Subsequently qualified research institutes and companies in the EU countries were visited for detailed technical discussions.

The findings of the study group's investigation are:

- The global problem of many countries infested with land mines urgently demands new technical solutions, with particular regard to the localisation and unequivocal identification of land mines, above all anti-personnel mines (APM).
- No commercial sensor at present available in EU countries meets the requirements.
- Research institutes and industry in EU countries have the basic technology for new sensor systems.
- Only a combination of different sensor systems can fulfil the requirements for the localisation and identification of land mines.
- The level of performance required for humanitarian de-mining activities can only be achieved in a short time through a consistent European R & D program.
- A European R & D program is proposed which will develop a prototype by 1998 and demonstrate its functions and operation in a mine-infested area.
- Throughout its duration this program will require not only close co-operation between expert groups in Europe, but also - and especially - on-site co-operation with local experts, de-mining specialists and relief organisations in the territory concerned.

2. Suitable Techniques

The study group has considered a variety of major aspects to assess and select suitable measurement techniques and sensor technologies for the localisation and classification of

land mines, particularly the APM. None of the sensors examined, irrespective of the development stage reached, will be able to fulfil the tasks alone.

The experts unanimously acknowledge that only a multi-sensor package can meet the requirements.

Furthermore, owing to the different local situations and actual tasks there will be a need for hand-held systems, for systems mounted on vehicles and for systems carried aboard aircraft or helicopters. Most probably, sniffer dogs will still be a solution especially in dwellings, thick forests, plantations and very inaccessible land. Airborne systems may play a primary role in surveying mine fields and defining their boundaries.

Bearing in mind the required "quantum leap in cost-effectiveness", only systems mounted on vehicles or carried aboard aircraft/helicopters will make this cost reduction possible while at the same time improving performance. Therefore it is recommended to focus on the development of an integrated system to be mounted on a vehicle. In line with future requirements, this will allow spin-offs in the form of hand-held and airborne systems.

3. The most promising sensor types

The study group has endeavoured to identify which characteristic parameters of the mines the sensors can measure and to consider their current development stage as an important factor. Hence, the following sensor types are considered the most promising and those with the best outlook:

- the 3-axis Induction-Gradiometer, one- or multi-frequency,
- the imaging polarimetric Surface Penetrating Radar,
- the imaging, polarisation-sensitive Infrared Sensor working in the middle- and/or thermal-infrared region.

However, to satisfy all the specifications fully only a combination of all three measurement techniques will solve the problem of the localisation and identification of mines and guarantee the necessary improvement over current methods.

In addition to these key technologies, the following sensor types were recognised to offer important supplementary information:

- biological sensors, i.e. the technical successor of sniffer dogs,
- polarimetric lidar instruments working in the blue region of the spectrum, which can penetrate water in rivers, flooded rice paddies, shores, etc.
- lidar instruments for measuring laser-induced fluorescence to distinguish natural and plastic objects (APM),
- short-wave microwave radiometry.

This second list summarises potential measuring systems not yet directly applicable but which ought to be interesting research topics with a view to proving their feasibility and technical realisation for field application.

Next to these first two sensor classes, which are the core techniques, of major interest, but still in the research stage, there is a series of complementary techniques for the determination of mine fields and mapping their boundaries, as well as for the essential exact mapping of topography, land use, transport routes and infrastructures:

- airborne polarimetric SAR systems,
- airborne interferometric SAR instruments,

- airborne imaging spectrometers,
- airborne infrared scanners,
- high-resolution optical panchromatic and multi-spectral sensors.

In the light of the discussions with experts and representatives of industry in EU member states, it seems that none of the key sensors today is ready for the required application. However, developments are so advanced that the basic techniques and methods already exist. A co-ordinated European R & D program is necessary in order to work on these individual basic sensors to develop an integrated system to solve the complex measurement tasks and adapt the sensor package to the different environmental conditions of the mine-infested regions.

4. The proposed R & D program

The purposes of a co-ordinated European R & D program are illustrated by some examples:

- Based on the existing GPR-profilometer, radar instruments are to be developed that produce 3-D images of objects on the surface or lying under thick vegetation or buried underground.
- Development of the existing induction-gradiometer into a multi-frequency, 3-D imaging instrument.
- Development of the existing infrared sensor into a polarimetric instrument that produces images in the middle- and thermal-infrared.
- Development of special hardware and software that fuse the signals and information resulting from the different sensor types and provide efficient detection information during operation.
- Development of real-time processors to handle large data volumes.
- Support for the systems through determination of the characteristic signature figures of the mines (fingerprint catalogues).
- Integration of all the elements in one comprehensive system.
- Support for developments to ensure the devices are robust, reliable and easy to use and maintain.

In the R&D program context, however, co-operation with present expert groups is recommended and access to existing developments must be ensured: for example in the field of multi-sensor data fusion or the development a of real-time processor for large data volumes.

5. Procedure proposal

Integration of the basic sensor technologies into a superior system for the localisation and identification of mines will require several achievements:

- For each of the three sensor groups, comprehensive and systematic signature measurements must be made on pertinent mine types in controlled environmental conditions to establish fingerprint catalogues. These catalogues are needed for mine detection and for development of identification techniques.
- The corresponding imaging techniques and search algorithms must be developed, tested and validated.

- Based on this laboratory work, the sensor fusion technique will be developed with a view to the needed detection and identification capability.

The laboratory equipment and measurement systems necessary for these tasks are available in EU member states. The corresponding activities can start right away. The environmental parameters such as soils, vegetation, weather, etc. can only be partially reconstructed in the laboratory. Therefore, complementary field tests are imperative in real conditions, meaning in authentic mine-infested regions, using already available measurement systems.

Along with these two sets of activities, the essential hardware and software components for each type of sensor must be identified and developed. The sensor parameters must be adapted and optimised according to mine signatures (laboratory measurements) and actual environmental parameters of the application region (field measurements).

The next step is to integrate the individual systems in one comprehensive system, including merging of information and actual information handling. The final step is the demonstration of the efficacy of the comprehensive system in the selected mine-infested area.

References

- [1] Alois J. Sieber, International Workshop and Study on the State of Knowledge for the Localisation and Identification of Anti-Personnel Mines, EUR 16329 EN, Ispra, August 1995.

REFERENCE TARGETS

P.CORONA, G.FERRARA
Ist. Teoria e Tecnica Onde Elettromagnetiche, I.U.N.
via Acton 38, 80133 Napoli
Italy

C.GENNARELLI, G.RICCIO
Dip. Ingegneria dell'Informazione ed Ingegneria Elettrica, Università di Salerno
via Ponte Don Melillo, 84084 Fisciano (Salerno)
Italy

ABSTRACT. In microwave remote sensing there is a well assessed use of corner reflectors for the calibration of Synthetic Aperture Radar (SAR) images. Physical Optics models, suitable to provide detailed informations concerning the electromagnetic field backscattered by such a kind of structure, are described. Explicit form solutions have been obtained for dihedrals and trihedrals with various faces geometries. They take into account the lighting of each face by the direct, reflected and diffracted rays. As a consequence, a very accurate amplitude and phase description of the backscattered field is obtained. Such results are of specific interest for the recently proposed utilisation of interferometric SAR procedures, which give rise to some questions about the phase behaviour of the Radar Cross Section of corners.

1. Introduction

Dihedral and trihedral corners consist of flat metal plates, mutually orthogonal. The faces can be arbitrarily shaped, but they are usually square or triangular. Such reflectors show a monostatic Radar Cross Section (RCS) large over a wide angular range. This allows their use in test ranges and mostly in anechoic chambers as reference for the experimental determination of RCS of other targets.

Corner reflectors have also been utilized in microwave remote sensing as calibrators for the Synthetic Aperture Radar (SAR) images in order to give accurate information on position and reflection levels. The calibration is usually restricted to the amplitude levels. The SAR interferometry as further capability of information handling, induces some concern about the phase stability (across the path) of the RCS of corner reflector calibrators. The use as phase calibrators of corner reflectors has to take into account such a behaviour, and the expected use of them in fixed position in permanent test sites, that will not allow their re-aiming, will further require the accurate phase knowledge. Possibility is also about to "correct" such a phase migration by introducing it in the computer codes used in interferometric SAR evaluations.

Such a practice need a near-perfect modelling of corners RCS: suitable mathematical models are described in the following, as well as their experimental validation. Furthermore the implemented codes are very fast, considering they are based on closed form integration, also suitable for small computers.

2. Dihedral corners

The 90° Dihedral Corner Reflector (DCR) is formed by two mutually orthogonal metal plates (see Fig. 1). It exhibits the important feature that rays, which enter DCR normally impinging

with respect to its wedge, are reflected from both the faces and return in the direction from which they came. As a consequence, it yields a large RCS over a wide angular range in a plane normal to its wedge. This peculiarity, the ease of positioning and the availability of an accurate model for the evaluation of its RCS [1] make it a practical reference target for RCS measurements [2],[3]. For this last use, it is convenient to perform the scanning in a plane containing the DCR wedge to obtain the wished ease of positioning. In fact, the backscattering return in the neighbourhood of the frontal symmetry condition is rapidly varying with respect to the angle between the incidence direction and the wedge, while it is not very sensitive to changes in the other aspect angle. Therefore the reference RCS value is practically obtained as the maximum return in the above mentioned scanning plane.

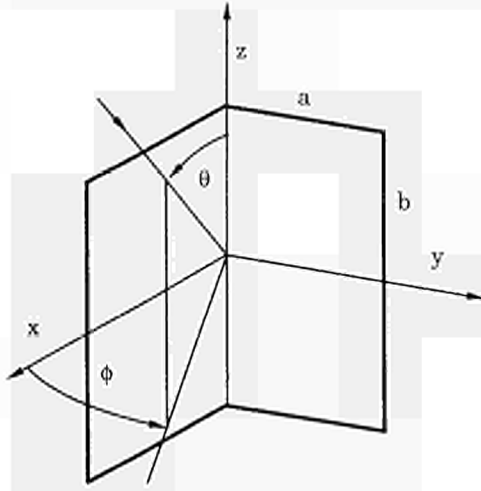


Fig. 1 - The dihedral corner reflector.

On the other hand, it is a very interesting target also from a theoretical point of view. Ray-optics terms of various order are always simultaneously present in every backscattering direction. In fact, for a composite structure of this type, the scattering contributions due to the interaction between its different parts can be significantly more relevant than those due to the direct scattering.

The interest on such a kind of structures is confirmed by the publication, in recent years, of several papers dealing with them. A detailed bibliography can be found in [1], where a very accurate model for the evaluation of the field backscattered by a perfectly conducting DCR in a plane normal to its wedge has been developed.

As it is well known, the RCS is defined as:

$$\sigma = \lim_{r \rightarrow \infty} 4\pi r^2 |\underline{E}^s|^2 / |\underline{E}^i|^2 \quad (1)$$

wherein \underline{E}^i is the incident electric field on the target and \underline{E}^s is the field backscattered at the observation point.

The spherical components of \underline{E}^s are given by

$$\underline{E}^s = \frac{-jkZ_0}{4\pi} \frac{e^{-jkr}}{r} \iint_S \underline{M} \cdot \underline{J}_s e^{jk\rho \cdot \hat{r}} dS \quad (2)$$

where k is the wavenumber, Z_0 is the free-space impedance, ρ is the vector from the origin to the integration point, \hat{r} is the unit vector in the observation direction, \underline{J}_s is the electric surface current density (whose components are in the cartesian coordinates system) and

$$\underline{M} = \begin{pmatrix} 0 & 0 & 0 \\ \cos\theta \cos\phi & \cos\theta \sin\phi & -\sin\theta \\ -\sin\phi & \cos\phi & 0 \end{pmatrix} \quad (3)$$

In the PO approximation the current distribution is simply related to the incident magnetic field \underline{H}_s^i by:

$$\underline{J}_s = 2(\hat{n} \times \underline{H}_s^i) \quad (4)$$

where \hat{n} is the unit vector normal to the target surface S .

In light of previous considerations, in the following the attention is focused on the backscattering by DCRs for $\theta = \pi/2$. In the basic PO model [4] the Geometrical Optics (GO) has been employed to describe the electromagnetic interaction between the DCR faces. As a consequence, for each plate, the integration in (2) has been performed over the patches directly lighted by the impinging rays and over those lighted by the reflected ones (see label i) and ii) in Fig.2, respectively).

To evaluate more accurately the field backscattered by DCRs an unusual PO model, referred as Improved Physical Optics (IPO) model, has been developed in [3] by using the Geometrical Theory of Diffraction (GTD) instead of GO. Besides to the lighting of the DCR faces by the direct and reflected rays, it takes into account the lighting by the rays diffracted from the edge of the other one (see label iii) in Fig. 2).

A further improvement to this last model has been achieved in [1] by taking into account also the rays diffracted from the faces edges parallel to the corner wedge and coming back directly to the observation point (see label iv) in Fig. 2). This has been done by adding the Physical Theory of Diffraction (PTD) correction term to the IPO model.

Many numerical and experimental tests have been carried out in order to evaluate the accuracy of the complete model and of the partial ones. A representative case, which refers to a DCR with $a/\lambda = 3.33$ and to an incident electric field normal to the incidence plane, is here reported. The measurements have been performed by the authors in the anechoic chamber of the Istituto Universitario Navale at Naples. The experimental set up is shown in Fig. 3. A standard horn has been employed as transmitting and receiving antenna and a magic T has been used to separate the

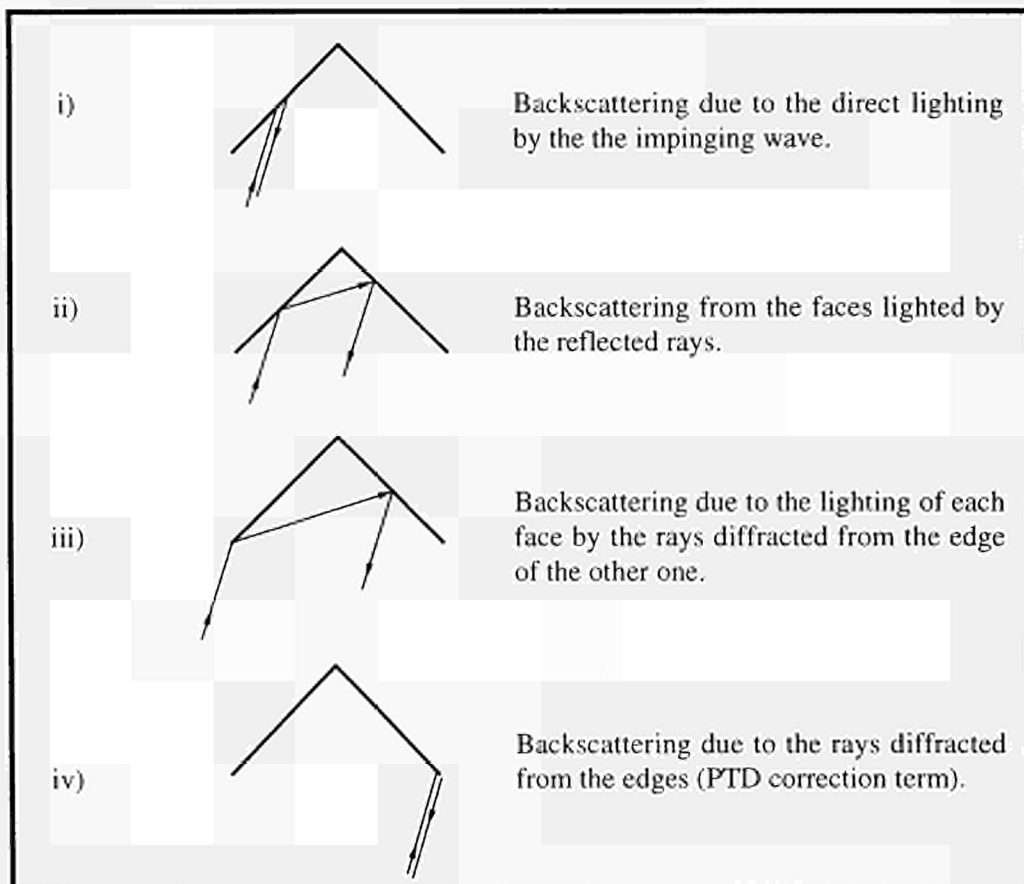


Fig. 2 - Relevant to backscattering contributions.

radiated and incident fields. Moreover, the use of the magic T in connection with a movable short and a variable attenuator allowed to compensate the background echo.

The graphs from Fig.4 to Fig.7 show the backscattered field (in dB), computed (crosses) with the different models and measured (solid line), versus the azimuthal angle ϕ .

The complete model fits almost perfectly the experimental results. Consequently, it can be considered as reference and the accuracy of the partial models can be estimated by computing the corresponding mean square errors. The results relevant to the complete angular range and to the partial one $40^\circ \leq \phi \leq 50^\circ$ are reported in Table I.

As a conclusion, it can be stated that the correction term included in the IPO model is the most meaningful one and that the relevance of the PTD correction term decreases on increasing the corner size [1].

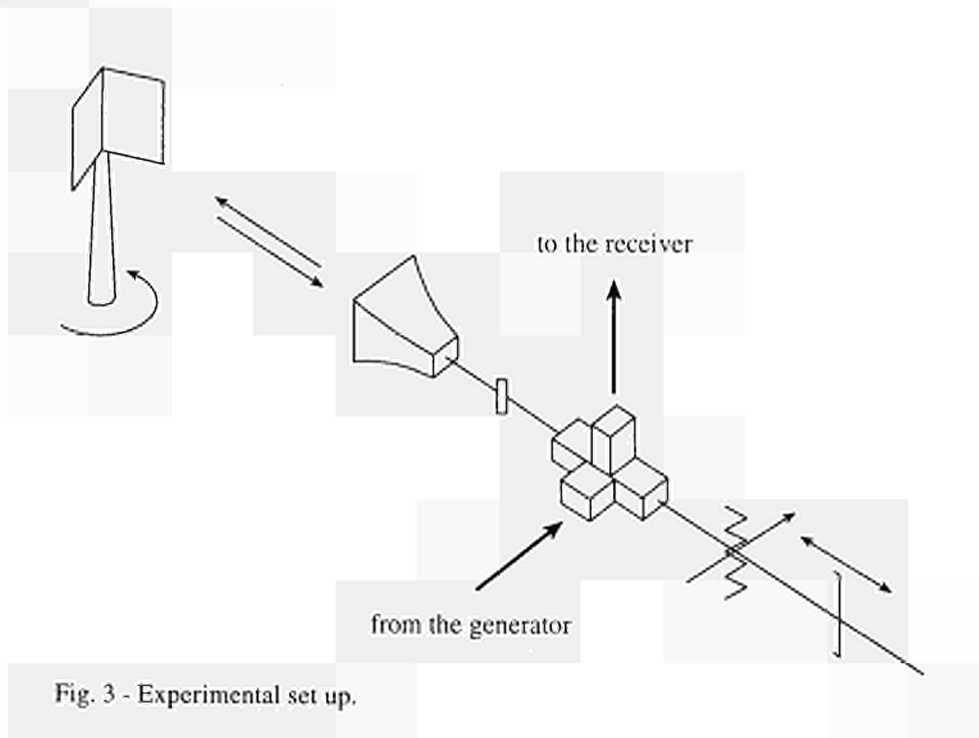


Fig. 3 - Experimental set up.

Table I

	Mean square error (dB)	
	$0^\circ \leq \phi \leq 90^\circ$	$40^\circ \leq \phi \leq 50^\circ$
PO	-23.69	-24.76
PO+PTD	-26.01	-23.19
IPO	-31.23	-30.32

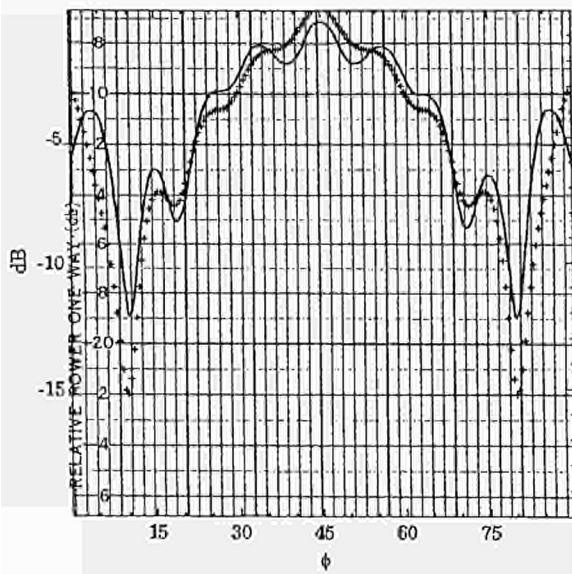


Fig. 4 - Field backscattered by a dihedral corner reflector with $a/\lambda = 3.33$. Solid line: measured. Crosses: evaluated by PO.

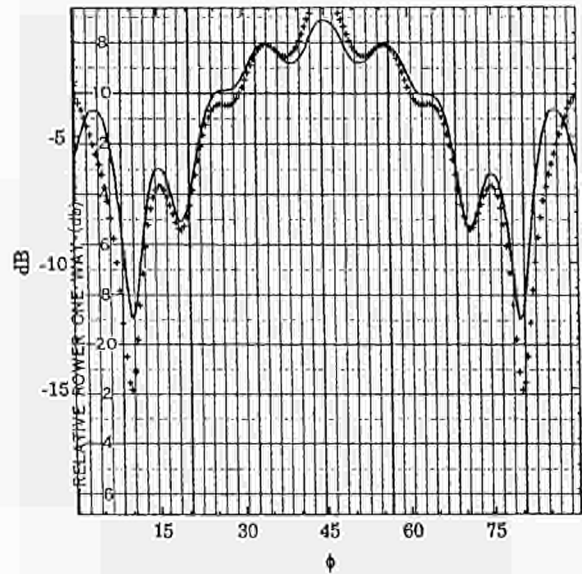


Fig. 5 - Field backscattered by a dihedral corner reflector with $a/\lambda = 3.33$. Solid line: measured. Crosses: evaluated by PO+PTD.

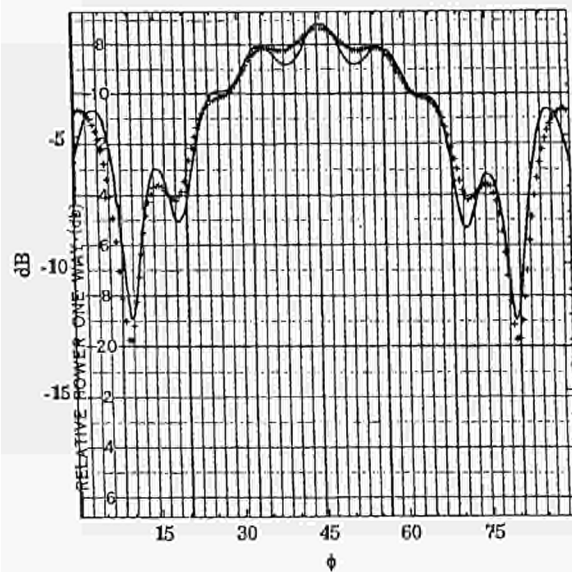


Fig. 6 - Field backscattered by a dihedral corner reflector with $a/\lambda = 3.33$. Solid line: measured. Crosses: evaluated by IPO.

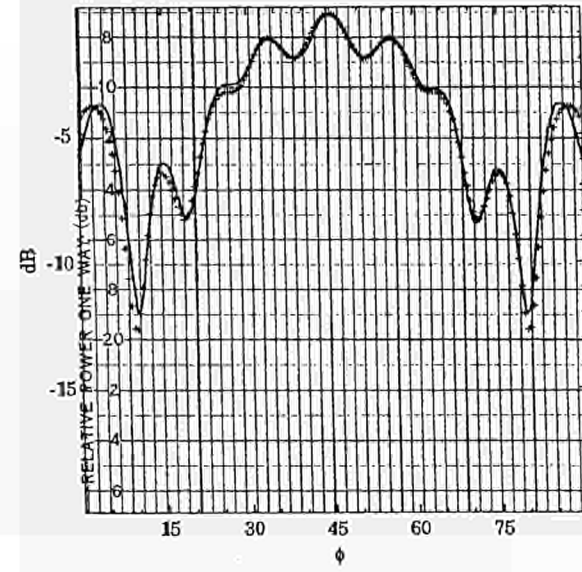


Fig. 7 - Field backscattered a dihedral corner reflector with $a/\lambda = 3.33$. Solid line: measured. Crosses: evaluated by IPO+PTD.

3. Trihedral corners

The Trihedral Corner Reflector (TCR) consists of three flat metal plates, which are mutually orthogonal. The faces can be arbitrarily shaped, but they are usually triangular or square (see Fig. 8). The peculiarity of such a reflector concerns its monostatic RCS, which is large over a wide angular range in both θ and ϕ angles. This characteristic and its low manufacturing cost justifies its use as radar enhancement device for navigational purposes [5] and as reference for the experimental determination of RCS values. Moreover, in recent years, TCRs have been widely used in microwave remote sensing as calibrators for the SAR images to give accurate informations on position and reflection level [6],[7].

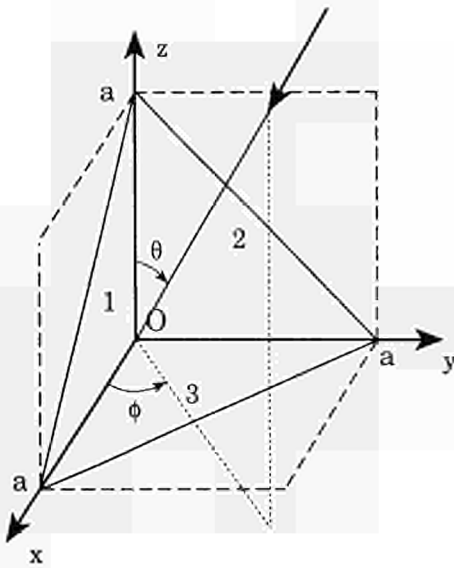


Fig. 8 - The trihedral corner reflector.

In [5], it has been shown that, for regular plate shapes, the effective area of the corner (simply related to its RCS) can be graphically determined. This area is evaluated by numerical integration in [7]. Groot [8] has proposed a Monte Carlo type numerical method, based on GO, to compute the RCS of an arbitrarily shaped TCR. The Shooting and Bouncing Ray (SBR) method has been employed to evaluate the scattering from TCRs and other benchmark targets [9]. A PO based tool, which uses GO to describe the interaction between faces and a computer aided technique to determine the patches involved in the PO integration, has been developed by Knott [10].

PO solutions, suitable to provide detailed informations concerning the field backscattered by TCRs, have been obtained by the authors in recent papers for various geometries of TCR faces [11]–[13]. In the basic PO model there developed, the global incident magnetic field on each corner plate and the corresponding PO surface current distribu-

tion have been determined by employing GO to take into account the lighting of each face by the direct, singly and doubly reflected rays. As a consequence, for all the faces, the integration in (2) has been performed over the patches directly lighted by the impinging rays and over those lighted by the reflected ones.

The evaluation in analytical form of all the lighted patches has been obtained by following the path of rays by means of the equation of the oriented line:

$$\frac{x - x_i}{\ell} = \frac{y - y_i}{m} = \frac{z - z_i}{n} \quad (5)$$

where (x_i, y_i, z_i) are the coordinates of the point of first incidence (second incidence) and ℓ, m, n are the direction cosines of the singly (doubly) reflected rays, which have been evaluated by applying the reflection law.

With reference to the path $1 \rightarrow 2 \rightarrow 3$, Fig. 9 shows as the shape of the lighted patches varies according to the incidence direction in the case of a TCR with triangularly shaped faces.

The analytical determination of the lighted patches has allowed to evaluate the PO integration in (2) in explicit form and to obtain a computer code which runs in a very short time.

A significant improvement [14] to the basic PO model is achieved by employing GTD instead of GO to describe the interaction between the TCR faces in a similar way as done with reference to DCRs and it is based on the fact that, in the basic PO model, the scattering contributions due

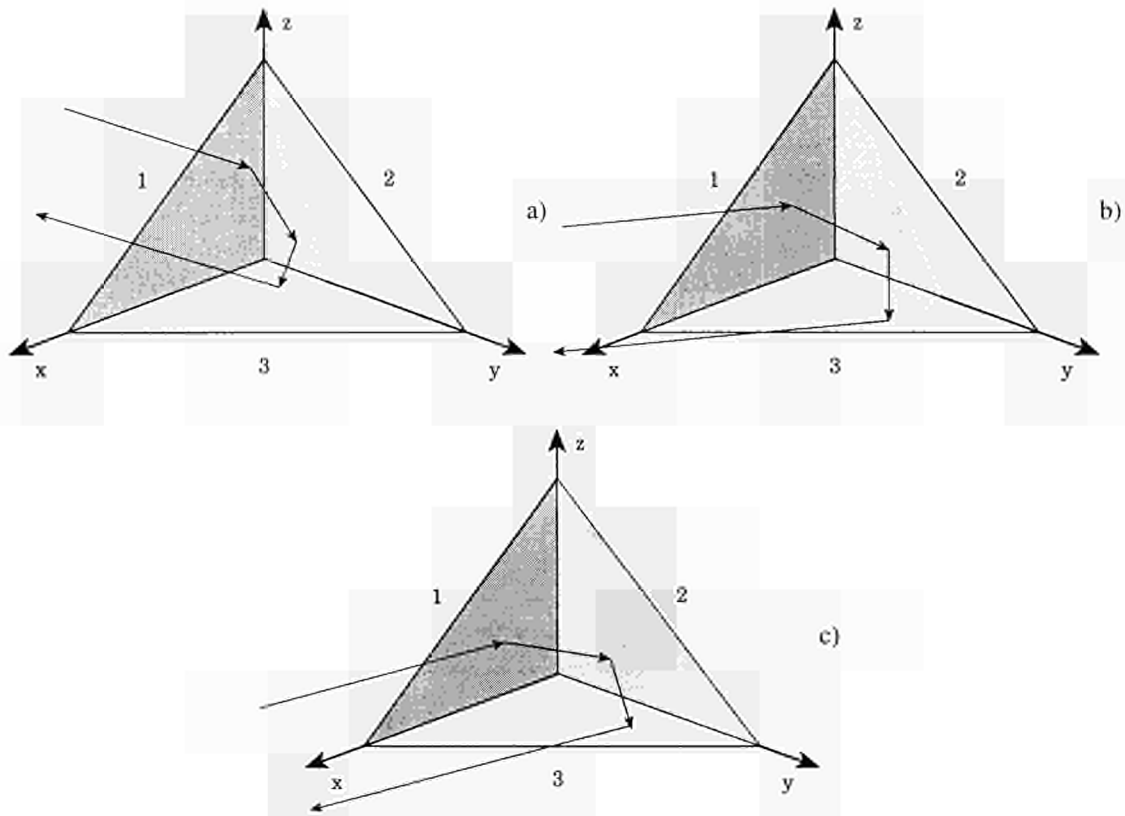


Fig. 9 - Path 1→2→3: GO illuminated patches.

to the interaction between the trihedral faces are more relevant than those due to the direct scattering. Accordingly, it may be expected that the most meaningful correction terms are those relevant to the “interaction” scattering, as already confirmed with reference to a DCR. The IPO model so obtainable takes into account also the lighting of each plate by the rays simply diffracted from the corner edges and by those diffracted and subsequently reflected.

With reference to the contributions due to the lighting by the rays simply diffracted from TCR edges, let us focus our attention on the terms related to the lighting of the faces 2 and 3 by the rays diffracted from the xz -plate edge (edge 1), see Fig. 10 a). To evaluate these contributions, we must integrate the corresponding currents induced over the lighted patches. To this end, we must use GTD both to establish the patches and to determine the lighting magnetic field diffracted from the considered edge.

Note that, for a fixed incidence direction, as the diffraction point moves on the edge 1 and the diffracted ray describes the cone, the patches lighted on the faces 2 and 3 assume the shapes depicted in Fig. 10 b).

Once the patches and the PO current parts related to the lighting by the diffracted rays are determined as function of the incidence direction, the PO integrations are numerically performed.

To avoid the complexity of a further raytracing, the contributions due to the lighting by the rays diffracted and subsequently reflected are evaluated by applying the principle of images. This last has to be applied to the images of the currents which effectively exist. This is accomplished by verifying that the reflected rays intercept the other face. The PO integrations are again numerically carried out.

As result of this mathematical model, a very accurate phase description is obtained [15]. Its knowledge allows the critical evaluation of the errors occurring in the interferometric use and

It is useful to note that the amplitude and phase description, obtained by the two models, does not change significantly in the neighbourhood of the (θ_M, ϕ_M) direction.

In figures 13 and 14 are reported the amplitude and phase patterns (referred to their values at the direction of maximum return) relevant to an incident electric field normal to the previously considered scanning plane and to a triangular TCR with $a/\lambda = 4.7$ and $a/\lambda = 10$, respectively.

4. Conclusions

The mathematical model developed by the authors uses a PO approach, suitable to provide the evaluation of the electromagnetic field backscattered by DCRs and TCRs. Solutions have been obtained for various faces geometries. They take into account the lighting of each face by the direct and reflected rays and edge corrections at various levels. The corresponding PO contributions are evaluated in closed form and, as a consequence, the computation requires a short computer time.

As result of this mathematical model, a very accurate pattern description is obtained. Its knowledge allows the critical evaluation of the errors occurring in the interferometric or polarimetric use and suggests computer supported procedures in the aim of correction of the phase errors, even in the case of intentional aiming of the corner reflectors out of the path, suitable for future use of corner reflectors not specifically aimed to a pre-defined path, but established in fixed locations, and to be used either for the ascending and the descending paths without re-aiming.

Field backscattered by TCRs has been computed either in amplitude and phase, this latter being of some interest in interferometric microwave remote sensing, and more generally in all SAR applications, reliability of presented results are testified by the comparison with amplitude, large angle, experimental patterns, very sensitive to the phase of each independent contribution to the e.m. field. Computed behaviour shows a phase sensitivity of some degrees (up to ten, across the full angular range) in the main patterns including boresight direction. It has to be expected an even larger variation in the off boresight cuts.

The use of the proposed model in the prediction of the (cross) polarisation pattern is under evaluation.

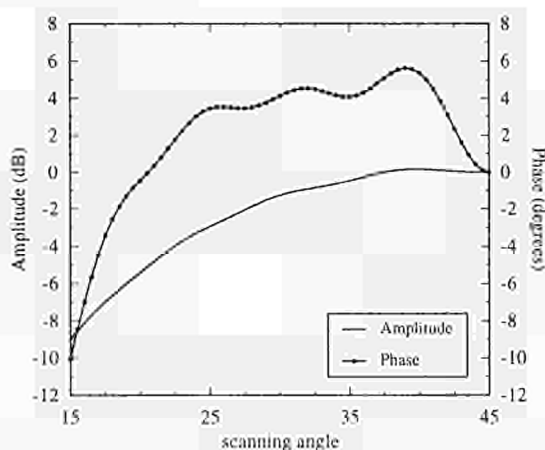


Fig.13 – Field backscattered by a triangular corner with $a/\lambda=4.7$.

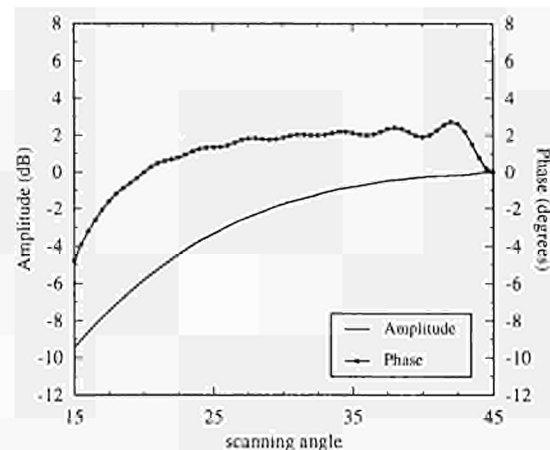


Fig.14 – Field backscattered by a triangular corner with $a/\lambda=10$.

References

- [1] P. Corona, A. De Bonitatibus, G. Ferrara and C. Gennarelli, "Accurate evaluation of backscattering by 90° dihedral corners," *Electromagnetics*, pp. 23-36, 1993.
- [2] P. Corona, G. Ferrara and C. Gennarelli, "The dihedral corner reflector as a reference target," *Annali dell' Istituto Universitario Navale di Napoli*, vol. LIII, pp. 27-36, 1984.
- [3] P. Corona, G. Ferrara and C. Gennarelli, "A simple and practical reference target for RCS measurements," *Alta Frequenza*, vol. LIV, no. 4, pp. 261-267, 1985.
- [4] E.F. Knott, "RCS reduction of dihedral corners," *IEEE Trans. Antennas Propagat.*, vol. AP-25, no. 3, pp. 406-409, 1977.
- [5] S.D. Robertson, "Targets for microwave radar navigation," *Bell System Tech. Journ.*, vol. 26, pp. 852-869, 1947.
- [6] A. Freeman, "SAR calibration: an overview," *IEEE Trans. Geosci. Remote Sensing*, vol. GE-30, pp. 1107-1121, 1992.
- [7] K.M. Keen, "New technique for the evaluation of the scattering cross-sections of radar corner reflectors," *IEE Proc.*, vol. 130, Pt. H, pp. 322-326, 1983.
- [8] J. Groot, "Cross section computation of trihedral corner reflectors with the geometrical optics approximation," *European Trans. Telecommun. and Related Tech.*, pp. 97-102, 1992.
- [9] J. Baldauf, S.W. Lee, L. Lin, S.K. Jeng, S. Scarborough and C.L. Yu, "High frequency scattering from trihedral corner reflectors and other benchmark targets: SBR versus experiment," *IEEE Trans. Antennas Propagat.*, vol. AP-39, pp. 1345-1351, 1991.
- [10] E.F. Knott, "A tool for predicting the radar cross section of an arbitrary trihedral corner," *Proc. IEEE SOUTHESTCON '81 Conf.*, pp. 17-20, 1981.
- [11] P. Corona, G. Ferrara, C. Gennarelli and G. Riccio, "A closed form Physical Optics solution for the backscattering by square trihedral corners," *Proc. of PIERS '94*, Noordwijk, The Netherlands, July 1994.
- [12] P. Corona, G. Ferrara, C. Gennarelli and G. Riccio, "A Physical Optics solution for the backscattering by triangularly shaped trihedral corners," *Annals of Telecommunications - Special Issue on Radar Cross Section of Complex Objects*, vol. 50, 5-6, pp. 557-562, 1995.
- [13] P. Corona, G. Ferrara, C. Gennarelli and G. Riccio, "Square-based trihedral corners: a Physical Optics model for the evaluation of the backscattered field," *Proc. of ICEAA '95*, Torino, Italy, September 1995, pp. 427-430.
- [14] P. Corona, F.D' Agostino, G. Ferrara, C. Gennarelli and G. Riccio, "An improved physical optics model for the evaluation of the field backscattered by triangular trihedral corner reflectors," *Proc. of MELECON '96*, May 1996.
- [15] P. Corona, G. Ferrara, C. Gennarelli and G. Riccio, "Phase mathematical modelling for corner reflectors in remote sensing synthetic aperture radar applications," *Proc. of IGARSS '95*, Firenze, Italy, July 1995, pp. 763-766.

THE TASK FORCE “CAR OF TOMORROW” ORIENTED TO TELEMATICS TECHNOLOGIES INTEGRATION

Y.R. CRUTZEN

*European Commission, Systems, Informatics & Safety Institute,
Joint Research Centre, Ispra Site, I-21020 Ispra, Italy*

ABSTRACT

A brief description of the Task Force “Car of Tomorrow” is followed by the role that the integration of telematics technologies will play in that context.

1. The Task Force “Car of Tomorrow”

The Task Forces have been set up and staffed by the European Commission last year in order to implement a strategic approach in fields where there are clear European industrial needs, especially considering the increased competition within world markets, and important societal needs, especially considering employment and environment. They have as main objective to better link research and industry and to help reduce the fragmentation of research across the European Union.

The most important tasks of the Task Forces are to:

- identify urgent needs and corresponding research priorities, e.g. technological bottlenecks, on the basis of wide ranging consultation with industry (manufacturers, suppliers, end-users), research institutions and public authorities;
- define new actions, within the European Commission specific research programmes, and develop a well structured Action Plan;
- study the necessary measures in order to improve the financial and legal environment of research activities.

The aim of the Task Force “Car of Tomorrow” is to accelerate the realisation of a new generation of vehicles which are clean, safe, energy efficient and “intelligent”^{1,2,3/}. This is a consequence of today road congestion and air pollution in city centres and of the need to preserve society’s mobility, public health and environment.

This will be achieved by coordinating relevant research projects, technological development and demonstration activities, including work being done, or soon to begin, under the specific research programmes of the European Union. These activities will also be coordinated with national programmes and industry initiatives.

The Research & Technological Development (RTD) priorities and associated performance targets proposed for the “Car of Tomorrow” have been established as a result of detailed discussions with the interested actors and are part of the Action Plan ^{1/}. It proposes safety, energy consumption and emissions performance targets and costs targets enabling the comparative assessment of competing technologies.

The Action Plan identifies research priorities for a range of technology options for ultra low & zero emission vehicles (ULEV & ZEV), which include:

- propulsion systems;
- technology integration;
- demonstration, testing and comparative assessment.

2. Integration of Telematics Technologies and Active Systems for Vehicle Operation, Safety and Control

Looking at the Action Plan /1/, of particular interest is the Chapter related to technology integration, vehicle design and telematics. The major key issue represents the integration of new vehicle concepts and alternative propulsion systems with transport telematics applications for vehicle control, safety, environmental performance monitoring and for minimising environmental impact.

As an example of ongoing activities related to an “intelligent” car, an in-car collision warning system is being developed that would automatically operate the brakes or throttle if the driver fails to take corrective actions when alarm sounds. In the Task Force Synopsis Book /4/, several existing projects are clustered in order to stimulate cooperation and collaboration. That is the case for the demonstration project “Rococo” performed by the Space Applications Institute and based on the concept of “drive by wire”/4/.

From the Detailed Performance Targets and Research, Technological Development & Demonstration (RTD&D) Priorities annexed to the Action Plan /1/, a list of industrial research priority areas related to the integration of road telematics systems for vehicle operation, safety and control are proposed as follows:

Speed Control, Lane and Distance Keeping.

Active systems based on advanced sensor products developed by electronics industries should be incorporated in the new generation of cars. Automated driving systems concepts are expected to be integrated too.

In-Car Collision Warning Systems.

Looking at driver monitoring and emergency handling, such systems should take automatically corrective actions. Close attention should be paid on the driver-system interface and human aspects. For example, research into optimally assisted driving and safety intervention systems is requested in poor weather and low visibility conditions.

Active Environmental Control Systems.

Development of transport telematics systems to link ULEVs & ZEVs with stationary atmospheric monitoring.

“Green Box” Recording Systems.

Such vehicle systems & associated sensors are needed for energy consumption & emissions data logging. Telematics links with green box is useful for remote monitoring of vehicle condition & for minimizing environmental impact.

Traffic Control and Driver Information Systems.

The development of reliable dynamic route guidance (collective and individual) systems and, in particular, of traffic information centres is confirmed. Motorway incident detection and immediate mobility response represents an urgent request.

Sustainable Urban Mobility, Traffic Congestion Warnings and Parking Guidance Systems.

The enhancement of urban road networks for travellers (car drivers, bus and tram users) is expected. Parking guidance systems will help to improve transport management and to make energy savings.

The best vehicle design and the most advanced telematics technologies will help to meet the expected achievements and exploitation into a high competitive market and will permit to improve competitiveness of European vehicle products.

3. References

/1/ Task Force "Car of Tomorrow", Action Plan & annexed Detailed Performance Targets and Research, Technological Development & Demonstration Priorities, European Commission, DG XII/F, 1996.

/2/ Task Force "Car of Tomorrow", Official Brochure, European Commission, ISBN 92-827-5386-7, 1995.

/3/ Task Force "Car of Tomorrow", Newsletter n.1, European Commission, DG XII/F, Apr. 1996.

/4/ Task Force "Car of Tomorrow", Synopsis Booklet, European Commission, DG XII/F, in preparation (1996).

NOISE RADAR TECHNOLOGY FOR CIVILIAN APPLICATIONS

Konstantin A. LUKIN

*Institute of Radiophysics and Electronics, National Academy of Sciences of Ukraine,
12 Akademika Proskura St., 310085 Kharkov, Ukraine*

E-mail: lukin@ire.kharkov.ua; fax: +38 0572 441105; tel:+38 0572 448349

Abstract

Noise Radar Technology has been shown to be both promising for civilian applications and adequate for today's microwave and electronic engineering. To use a chaotic oscillations generators as the sources of a wideband stationary noise signals and digital-analog time-integrating correlator with controllable digital delay line as the radar correlation receiver are the key points of the approach proposed for its development. Both vacuum and solid state microwave and millimeter wave chaotic oscillators have been designed using the principles of dynamical chaotization of the nonlinear system motion. The fast controllable digital delay line was designed using the two levels quantization of the reference chaotic signal. Two different models of the noise radars have been developed. One of them uses the correlation processing of the reflected signal, while another one exploits so called double spectral processing of the reflected noise signal. So called autodyne effect in chaotic generators has been proposed to use for radar measurements. It has been shown experimentally the possibility to use the chaotic signals in the noise radars with correlation processing which provides simultaneous measurements of the distance to moving target (such as buses, cars, bicycles etc) and their velocity with range accuracy about of 50 cm and resolution of 100 cm. This allows to use Noise Radar Technology in various civilian applications where the radars have to be used, such as automotive and navigation systems, as well as remote sensing systems like SLRs and SARs. The advantages of the Noise Radar Technology for design of such a systems and their implementation are discussed at the conclusion of the paper.

1 Introduction

Radar design is always a compromise between the radar characteristics desirable according to its destination, from one hand, and available ones, from another one. The radar characteristics first of all depend on the type of signal used in the radar. That is why the choice of an appropriate radar signal is the most critical point of its design. Such properties as high accuracy and resolution of the measurements both of range and velocity of a target; low levels of radiated signals and good electromagnetic compatibility; small sizes and light weights; low consumption and cost of the radars are more important properties in the case of their civilian application rather than military ones.

It has been accepted about 40 years ago that a noise signal with fast enough decay of correlations is theoretically the ideal one from many of viewpoints. For instance, the use of the noise signal provides such an advantages as the single-validity of its un-ambiguity function; simultaneous measurements of a distance until a target and its velocity, using the same transmitter-receiver unit; etc, etc. (See the Conclusion for more details) . However, many experiments which have been carried out in the sixties years showed very restricted abilities of the noise radars under development in comparison with a conventional pulse radars and phase code manipulated ones. This was connected with availability at that time only a narrow band noise signal generators and correlation receivers.

Meanwhile, quick development of the science on dynamical chaos gives the methods for generation of wideband chaotic signals, and at the same time the integrated circuit electronics provides a fast digital components for design of appropriate digital correlators for their processing. This gives a chance to go around the mentioned above difficulties of the noise radar development and take the advantages of the noise signal usage for a different remote sensing systems design.

In the present paper we describe one of the possible approaches to the development, of the Noise Radar Technology, which is under investigation in the Laboratory of Nonlinear Dynamics of Electronic Systems of the Institute of Radiophysics and Electronics, National Academy of Sciences of Ukraine [1] - [6]. The key points of that approach are the use of chaotic oscillations generator as a source of noise signals [2],[3],[6] and digital-analog time-integrating correlator with electronic controllable delay line as a main part of correlation receiver of the noise radar [1], [4],[5]. The advantages of the Noise Radar Technology and possible areas of their application are briefly discussed in the Conclusion.

2 Chaotic Generators as a Source of Noise Signals

The advantages of chaotic signal generators in comparison with, say, thermal noise signal sources consist in the much more high spectral density of the generated signals, availability of their parameters control, simplicity of generator construction etc. However, there is one question: whether is it possible to use the chaotic signals in the noise radars with correlation processing of the return signal reflected by a target? The short answer is very simple: Yes, if the required measurement time of the cross-correlation for a one distance is much longer decorrelation time of the chaotic signal, which also should not contain any fast periodical components. For the correlation processing it does not matter how the noise signal has been obtained, if it has no any auto-correlations during measurement time. This statement has been completely conformed by the experiments carried out with the use of millimeter wave noise oscillators developed on the principles of the dynamical chaotization of nonlinear systems motion and briefly described below.

Nonlinear dynamics of the BWOs is governed by the set of nonlinear integral-differential equations in partial derivatives which has no analytical solutions. In the simplest case the solutions of these equations depend on the only parameter K , which equals to the working current to starting current ratio.

Numerical modeling of the self-oscillatory regimes using these equations shows that increasing the parameter K causes the qualitative change of BWO's self-oscillatory regimes. Particularly, at $K = 30$ the oscillations become an irregular ones due to the chaotic auto-modulation of their amplitude. The signal generated in chaotic auto-modulation regime is characterized by both a continuous frequency spectrum concentrated around some central frequency and fast decay of its correlations. However, to provide a large enough values of the parameter K in millimeter waveband devices is very difficult problem. One of the ways to solve this problem is to provide a weak reflection of the slow waves at the ends of periodic structure. Such a slow wave resonator with an enlarged electrical length and weak reflections we called as weak-resonant oscillatory system. The quality factor of its resonant modes does not exceed the value of 80. We used that oscillatory system to construct the BWOs for generation of the millimeter wave chaotic signals with wide enough and uniform frequency spectrum and called it as Weak Resonant BWO (WRBWO) to distinguish it from conventional devices both resonant and non-resonant BWO.

The WRBWO's dynamical properties is characterized by the two parameters, namely by parameter K and the complex reflection coefficient R , which also defines the efficiency

of the additional feedback channel. The experiments carried out revealed the following behavior of the WRBWO developed. For the fixed value of the parameter R the qualitative change of oscillatory regimes take place with increasing the parameter K , i.e. the working current. For $K > 3$ regular single frequency oscillations with continuous tuning of the frequency within the band of 12% are observed with voltage changing. For $K > 6$ the periodic auto-modulation of the oscillation amplitude takes place, which is characterized by appearance of satellite frequencies near the central one. The frequency of the amplitude modulation can be tuned within the band of 140 MHz – 300 MHz by changing of the accelerating voltage. For $K > 11$ the regular auto-modulation becomes quasi-periodic one with equidistant frequency spectrum. Narrow band chaotic oscillations with the frequency spectrum concentrated around auto-modulation spectral lines, are observed at $K = 19$. That value of K is less than the corresponding value for a non-resonant BWO. Chaotic oscillations with $\Delta f/f = 2 - 3\%$ (at the power level of -10 dB) are observed for $K = 50$.

The packaged WRBWO noise oscillators developed on the base of the described principle generates the K_a -band noise signals with frequency bandwidth from 50 MHz to 1000 MHz. The central frequency lays in K_a -band and output power reaches the value of 15 W in continuous working regime.

Actually continuous working regime and correlation processing give possibility to use chaotic generators with very low output RF power. That is why the development of a solid state chaotic oscillators is of a big interest. Below we describe the main results of the millimeter wave chaotic oscillators development on the base of serial IMPATT an Gann diodes.

A resonant-cap IMPATT diode oscillators are in common use in the millimeter wave-band. The resonant-cap can be considered as a transformer allowing to match the impedances of the diode itself and waveguide. This construction contains two coupled oscillatory systems and allows to design the chaotic oscillations generator, on the base of dynamical chaotization principle, which is connected with the nonlinear modes interaction [7] and could be associated with the route to chaos via loss of torus smoothness. One of these oscillatory systems is formed by the resonant-cap diode itself and the nearest waveguide wall. Its eigen-frequencies are determined by both cap's disk sizes and its distance to the waveguide wall. The second oscillatory system is the waveguide resonator formed by the resonant-cap diode and a sliding short placed at the opposite end of the waveguide. Its resonant frequencies are mainly determined by the distance between these two reflectors. The generator construction provides the conditions needed for simultaneous excitation of the oscillations at the two resonant modes, namely: the resonant-cap mode, having a small quality factor ($Q = 50$) and the waveguide cavity mode, which has a higher quality factor. The conditions of the chaotic oscillations excitation are adjusted by mutual detuning of the resonators eigenmodes and changing of the bias voltage.

Two essentially different working regimes have been observed in the experiments conducted with GaAs IMPATT diodes in the K_a -band. In the first regime the chaotic oscillations with frequency spectrum width about of 150 MHz and central frequency being close to the resonator eigenvalues are excited. The second regime is characterized by the excitation of the oscillations with the spectrum width up to 1 GHz. This regime is observed for the longer distances between the sliding short and resonant-cap, which leads to the forming of the multi-mode waveguide resonator with a small values of quality factor. The output RF power of the both regimes is close to the nominal one.

The same idea of the nonlinear two-modes interaction has been used for the development of the two chaotic oscillators of another kind. One of them uses two coupled waveguide mechanically tunable resonators, being oriented mutually perpendicular and having the IM-

PATT or Gann diode at the joint area. The second chaotic oscillator uses the construction in which the tunable resonators are formed by the diode itself and two sliding shorts being placed in the same waveguide one after another. In this case we have the serial coupling of the waveguide resonators. For the both constructions the chaotic oscillations regime was observed in X - and K_a -bands. In the case of the Gann diode the influence of the low frequency oscillations excited on the microwave chaotic signals has been registered.

A single solid state noise oscillator developed allows to produce the continuous chaotic signals with output power up to 100 mW and controlled frequency bandwidth from 20 MHz to 200 MHz . The measurements of their auto-correlation function have demonstrated the fast decay of the correlation. The time of signal decorrelation is reciprocal of the frequency spectrum width, which is in good agreement with the theory of stationary random signals.

3 Digital-Analog Time Integrating Correlator for Noise Radar with Correlation Receiver

For the correlation processing of the received quasi-stationary noise signals the digital-analog time-integrating Correlator was designed and constructed (see Fig.1) on the base of fast digital components with clock frequency up to 500 MHz . To avoid an analog-digital converters usage the principle of the two levels quantization of the noise signal in the reference channel has been used. The correlator designed and constructed [1], [4], [5] allows to process the noise signals with bandwidth about of 200 MHz . Clock frequency used allows to provide the accuracy of time delay measurements about of 2.5 ns . Separate channel for the measurement of the Doppler shift of the carrier frequency caused by the target movement (or vibration) is available and allows to measure this shift in the range of 100 Hz to 200 KHz . This corresponds to the velocity range of 0.4 m/s to 750 m/s for the carrier frequency $\sim 40\text{ GHz}$. Integration time could be varied from $5\text{ }\mu\text{s}$ to $1500\text{ }\mu\text{s}$. To perform a two positions measurements, as well as the measurements of the auto-correlation function of the radiated signal, two corresponding channels for the signal correlation processing has been also constructed.

The controllable digital delay lines (CDDL) of two kinds were designed, namely: the CDDL on the base of shift registers - for a short distances and the fast RAM memory CDDL - for a long ones. Note that it is possible on the base of GaAs-technology to design the digital delay lines in a single ship with required delay times and the clock frequency up to 4 GHz .

In the case of correlation processing of the received noise signals the distance is defined via the time delay measured as the coordinate of the cross-correlation function maximum. To perform the corresponding experiments the laboratory models of the both one and two antennas versions of the noise radar were constructed using the heterodyne scheme, as well as the chaotic oscillators and digital-analog time-integrating correlator developed. The cross-correlation of the reference and received signals as a function of the CDDL delay time value is observed on the oscilloscope screen. Digital output for input to a computer is also provided in the correlator. Observation time (oscilloscope swiping) could be varied from 0.32 ms to 32 ms . The Doppler signal from the moving reflector was observed simultaneously on the both second oscilloscope screen and low frequency spectrum analyzer.

Experiments carried out showed that the noise radar designed provides the distance resolution value of 100 cm with accuracy about of 50 cm . The Doppler signal was observed from the moving target, having velocity within the range from 0.5 m/s to 50 m/s . The

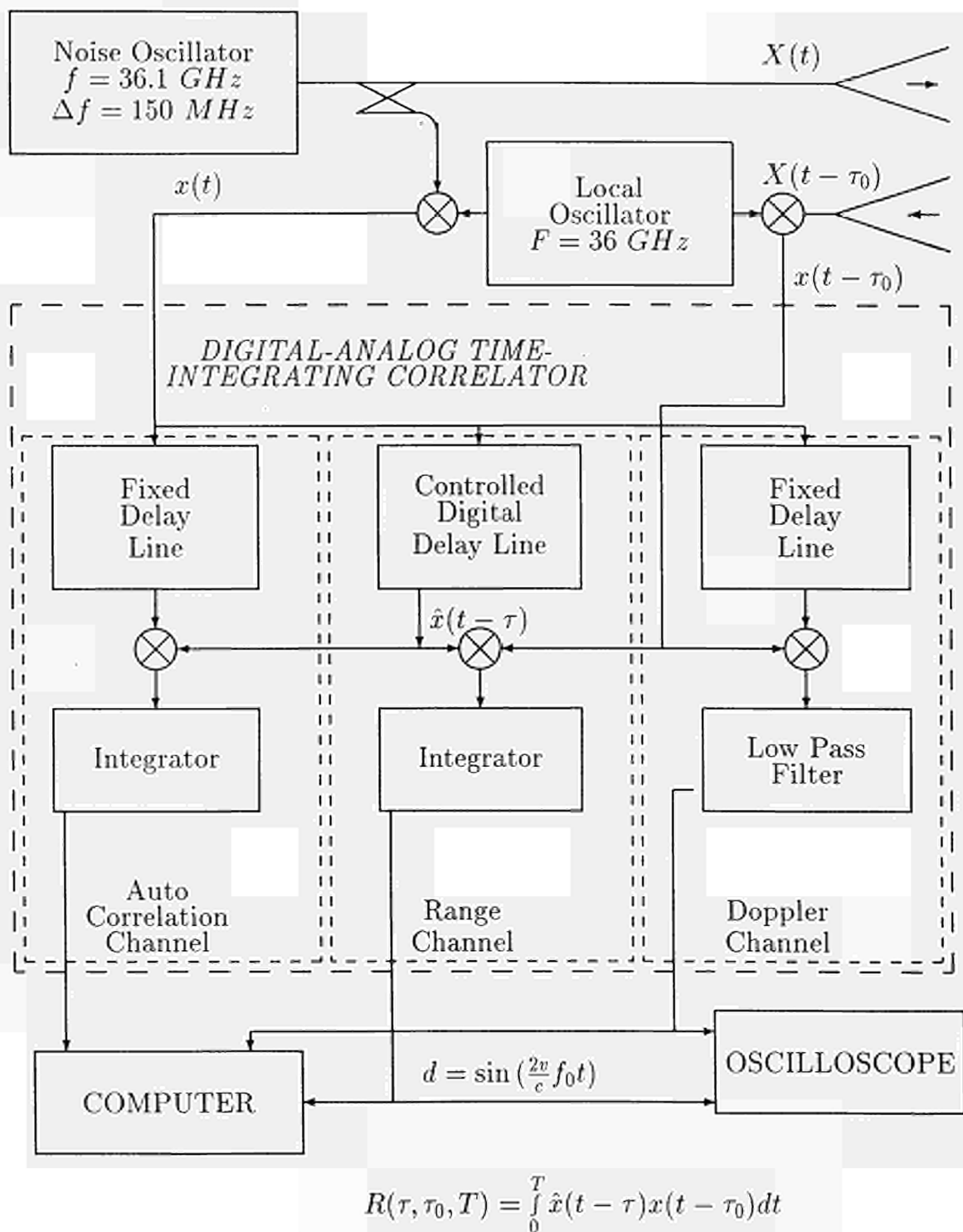


Fig.1. Block-diagram of the noise radar with correlation receiver.

cross-correlation function of the signal, reflected by moving cars, peoples and dogs was observed in the form of Gaussian-like curve moving across the oscilloscope screen in real time scale.

Immunity against interferences was tested by the fitting of the external noise signal with the same power spectrum bandwidth into the receiver channel. Normal operating of the noise radar took place when the voltage on the HF mixer-diode caused by the interference exceeded the useful signal voltage by 30 dB for the integration time about of 0.5ms.

4 Noise Radar with Double Spectral Processing

The model of the other kind of Noise Radar is also designed and tested, using so called double spectral processing of the reflected signal [8]. This processing method uses the phenomenon of the power spectrum periodic modulation of the sum of radiated (reference) and reflected signals under the conditions, when the signal propagation distance is much larger then it's coherence length ($l_c = v/\Delta f$, where v is the signal propagation velocity and Δf is the signal spectrum bandwidth). In this case the distance L is defined from the measured power spectrum modulation period T_ω in the following way $L = v/2T_\omega$. So, the device or computer spectrum processing of the sum of the reference and received signals and secondary spectral processing of the power spectrum envelope of the first spectrum analyzer gives possibility to measure distances avoiding the CDDL usage and employing a serial wide-band spectrum analyzers (allowing to process the noise signals with a bandwidth up to 2 GHz) in stead of special correlators. Experiments carried out showed the high accuracy of the distance measurements.

The construction of the noise radar with double spectral processing could be simplified by using the autodyne phenomenon, occurring for the wideband noise oscillators [9],[10]. This phenomenon consist in the periodic modulation (with the period mentioned above) of the output signal power spectrum under the effect of the reflected signal on the noise oscillator for the distances, exceeding the radiated signal coherence length.

5 Conclusion

The possibility of the development of the MM wave noise radars is experimentally proved for the noise signal bandwidth up to 200 MHz. This value is bounded by the clock frequency of digital components used in CDDL and, hence, can be increased by applying the modern semiconductor technology. Design of the one-channel correlator with 500 MHz signal bandwidth is in progress.

In conclusion let us list one more time the most important advantages of the Noise Radar Technology:

- I. Basic properties of random signals and correlation processing give the following advantages:
 - a. Unimodal un-ambiguity function provides:
 - no theoretical limits on the noise radar working range;
 - no false signals due to side lobes of un-ambiguity function;
 - simultaneous measurements of a target distance and its velocity.
 - b. Correlation processing of wideband noise signals gives ability to design a radar with :
 - optimal receiver for the reflected noise signals providing maximum of signal-to-noise ratio;
 - combination of the advantages and abilities of both pulse and continuous working radars;

- high electromagnetic compatibility characteristics and resistance against external electromagnetic interference, allowing simultaneous work of many similar devices at the same area.

c. Continuous working regime provides:

- low power of radiated signal - no peak power;
- no contradiction while providing the best conditions for simultaneous measurements of distance and velocity.

2. Expected advantages of the noise radar implementation:

a. The use of the chaotic oscillators developed provides the simplicity of signal forming scheme; in this sense such an oscillator is equivalent to a single frequency one.

b. Correlation receiver and low power of radiated signals give possibility to use a low voltage and low current components.

c. The use of the suggested digital-analog time-integrating correlator, as well as microwave or millimeter wave solid state electronic components allows to employ IC technology for a totally solid- state radar development.

All this gives the grounds to use Noise Radar Technology for development of compact, low consumption and cheap devices to be used in many civilian applications. For example, it could be used for the development of the efficient microwave sensors in the following remote sensing systems:

- both car collision warning and intelligent traffic control systems, where high resolution, accuracy and fast processing, as well as small sizes and light weights are required.

- millimeter wave navigation and surveillance systems with a high distance resolution, as well as high reliability and environmentally save characteristic;

- millimeter wave radar with synthetic aperture;

- noise radar-reflectometer for measurement of the cut-off layer position in fusion plasma reactors (tokamaks, torsatrons).

References

- [1] K.A.Lukin: K_n -band Noise Radars; Proceedings of the International Symposium "Physics and Engineering of Millimeter and Submillimeter Waves", June 7-10 1994, Kharkov, Ukraine; V.4, pp.761-763, June 1994.
- [2] K.A.Lukin and V.A.Rakityansky: Excitation of Intensive Chaotic Oscillations of Millimeter Waveband; Proceedings of ISSSE, 1-4 Sept. 1992, Paris, pp.454-457, Sept. 1992.
- [3] K.A.Lukin and V.A.Rakityansky: Sources of Millimeter Noise Oscillations; Proceedings of the International Symposium "Physics and Engineering of Millimeter and Submillimeter Waves", June 7-10 1994, Kharkov, Ukraine; V.2, pp.322-324, June 1994.
- [4] K.A.Lukin, Yu.A.Alexandrov, V.V.Kulik, et. al.: "Wideband Millimeter Noise Radars"; International Conference on Modern Radars, 1994, Kiev, Ukraine, pp.30-31.
- [5] K.A.Lukin: Noise Radar with Correlation Receiver as the Basis of Car Collision Avoidance System; 25-th European Microwave Conference, Bologna; Conference Proceedings, UK, Nexus, 1995, pp.506-507, September 1995.
- [6] V.A.Rakityansky and K.A.Lukin: Excitation of the Chaotic Oscillations in Millimeter BWO; Int. Journal of Infrared and Millimeter Waves; V.16, N6, pp.1037-1050, June 1995.

- [7] B.P.Efimov, K.A.Lukin and V.A.Rakityansky: Chaotic Interaction of Modes in the Electron-Wave Auto-Oscillator with Two Feedback Channels; Letters to Journal of Technical Physics; V.15, N18, pp.9-12,1989 (in Russian).
- [8] J.L.Poirier: Quasi-Monochromatic Scattering Signals and Some Possible Radar Applications; Radio Science;V.3,N9, pp.881-886, 1968.
- [9] B.P.Efimov, K.A.Lukin and V.A.Rakityansky:Transformation of Chaotic Oscillation Spectrum by Reflection; Journal of Technical Physics, V.58,12, pp.2398-2401, 1988 (In Russian).
- [10] K.A.Lukin, V.V.Kulik and V.A.Rakityansky: Autodyne Effect in BWO Operating in Chaotic Regime"; Proc. of the SPIE 2250, Ed. by M.Afsar, pp.207-208, 1994.

conditions, and there is still a need for new types of representations, particularly to account for the multiscale effects, or the fluctuations of local statistics. For example, the use of UWB pulse for buried targets detection, or the assessment of multifrequency spaceborne radar data, yield the need for a multiscale characterization of rough surfaces.

To another extent, in the processing step which consists in interpreting scattered data for identification of a given natural scene or a target embedded in clutter, the availability of numerous discriminating parameters is very important. Looking to improve the information extraction of a scattered signal leads to incorporate in the signature more numerous discriminating parameters such as, for example in the UWB regime, polarimetric features, diffracting centers, resonances...

Very valuable tools to deal with the previous topics are electromagnetic scattering simulation of scenarii of interest. In spite of its complexity, it is recognized that only a theoretical approach based on Maxwell's equations can yield both qualitative and quantitative understanding of the interaction between the electromagnetic wave and the rough surfaces. Among them, numerical methods may play a very important role because if they cannot cope with a complete scenario in most of the cases, they may solve rigorously part of the problem for a subsequent gathering of diffraction events or study phenomenological effects for example either on small scale, or on bidimensional representation.

The conducting theme of this paper is based on the fractal approach for soil studies, because this concept by itself permits presenting elements of responses to some of the above interrogations as well as dealing with all the above topics.

Indeed, fractals are known to be a good descriptor for some natural targets. The fractal geometry of vegetation is frequently reported (Fig. 1) [Prusinkiewicz 90]. The fractal geometry of soils has been also investigated: [Ogilvy 91] [Keller 89] [Le Mehauté 90].

Subsequently, it is interesting to know to what extent the fractal properties are transmitted to the scattered field. Some studies based on SAR images were conducted [Bourissou 94a] [Bourissou 94b] [Blackledge 92] [Stewart 93] and showed that a classification in several classes (sea, mountain, forest, town, grass land) is possible using the fractal dimension of the scattered field as a discriminating parameter. Some works [Jaggard 90b] have exposed relationships between the fractal characteristics of a rough surface and the field scattered by this surface. Other studies based on time-domain measurements for sea remote sensing purposes [Lo 93], exhibited a fractal behavior for the scattered field.

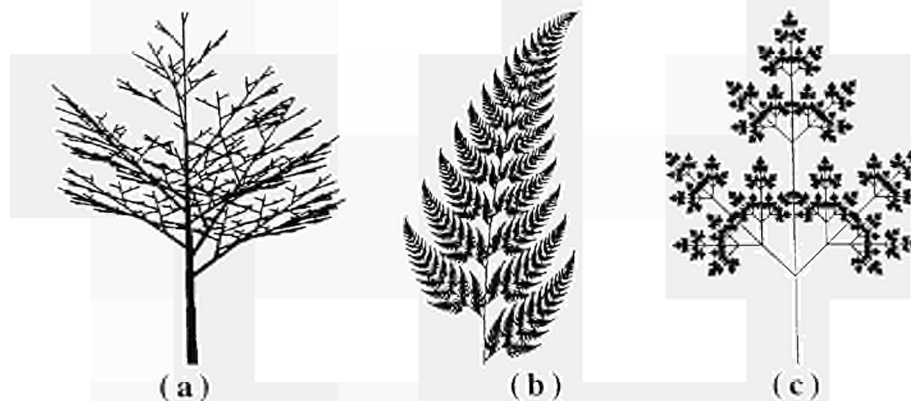


Fig. 1: Fractal representation of vegetation
(a) : random fractal - (b)&(c) : deterministic fractals

This paper is divided into three parts. The first part is dedicated to the generation of bidimensionnal fractal profiles and to the fractal dimension extraction. The fractal analysis is based on the well known box counting method for which we propose some improvements in the implementation. We present some realizations of generated fractal profiles, and subsequently discuss the pertinence of the fractal representation of soil surfaces versus usual representations, i.e. stochastic process based on the knowledge of the surface correlation function (including the correlation length).

The second part is dedicated to the numerical computation of the electromagnetic field. To deal with bidimensional Perfectly Electrically Conducting (PEC) profiles Method of moments (MoM) is the most convenient. For dielectric profiles, Finite Differences in the Time Domain (FDTD) is more appropriate because it can cope with heterogeneities of any kind and then address, in addition to surface scattering which is the main emphasis of this paper, other topics of most importance like volume scattering and subsurface scattering for detection and identification of buried objects.

Third part is dedicated to the field scattered by the previous profiles. Relationships between the fractal dimensions of the profile and of the scattered field are eventually investigated for several conditions of polarization, incidence and observation directions. Influence of noise is also investigated.

In a final step, the paper describes the follow up of these actions, in particular those related to the need of strong interaction between these theoretical studies and experimental ones taking advantage of the facilities of the JRC ISPRA center.

1. PROCESSING OF A FRACTAL FUNCTION

1.1. INTRODUCTION : USUAL DESCRIPTION OF ROUGH SURFACES

For remote sensing purposes, roughness of a soil surface is traditionally modeled stochastically. The description involves a gaussian probability density function for the height distribution, and a correlation function describing the statistics in the horizontal direction. In addition, the roughness spectrum (which is required for surface backscattering estimation), is defined as the Fourier transform of the surface correlation function. A typical example is a random surface with gaussian height distribution and gaussian surface correlation function (note that in general both might be different).

However, the above description of roughness state raises many open questions in the case of natural surfaces. Natural rough surfaces are not expected to match with an one-scale isotropic stationary bidimensional random processes modeling. Making use of the profile measurements (long profile, small sampling step, multidirectional, for different fields and surface types), further investigations on the subject are required, aiming at assessing a more realistic statistical model for natural surfaces. So far, the main conclusions derived from experimental analysis are as follows :

1) There are no experimental evidences against the assumption of gaussian distributed *profile heights*. In order to achieve a reliable estimate of the *r.m.s. heights* s , profiles must be long enough. As an example, the values of s estimated over the measured profiles on the smoothest agricultural fields have generally shown a convergent behavior only beyond 150 cm. In addition, estimates of s parameters for profiles extracted from a given homogeneous field have shown a variability increasing with the roughness of the fields.

2) For any surface type, experimental estimations of the *correlation length* l have shown a large inside-parcel intrinsic variability (typical mean values are ranging between 10 and 20 cm). A study aimed at assessing the minimum surface profile length offering a convergent behavior in the correlation length estimates has indicated poor convergence up to profiles of 300 cm length. The critical variability observed in the estimates of l cannot be explained completely by measurements errors and/or by the presence of multiscale roughness components.

3) Experimentally, *surface autocorrelation functions* (ACF) have generally indicated a shape more exponential than gaussian. However, it should be emphasized that a great variability of these shapes has been observed within a given parcel.

However, there are clues suggesting the existence of statistical parameters for characterizing the experimental profiles, which might be more stable than the correlation length. For example, in the case of profiles under investigation, the estimate of the profile root mean square slopes has been found to cluster around the average value of the estimates. This effect has been observed in other cases [Borgeaud, 1995]. In addition, a collection of other parameters aimed at quantifying the roughness effect are reported in the literature, without being necessarily considered in remote sensing applications. Characteristic function (Fourier transform of the height probability density function), higher order surface properties, fractals characteristics can be mentioned. Next paragraphs are dedicated to the fractal approach as an alternative way of characterizing a rough surface.

1.2. GENERATION OF A FRACTAL PROFILE

Fractal functions can be generated by using randomly phased sinusoidal functions: the Weierstrass functions, [Chen 93a] [Jaggard 90a]. They can be expressed as follows :

$$W(x) = \eta \cdot \frac{\sqrt{2} \left[1 - b^{(2D-4)} \right]^{\frac{1}{2}}}{\left[b^{(2D-4)} - b^{(2D-4)(N_2+1)} \right]^{\frac{1}{2}}} \cdot \sum_{n=1}^{N_1} \left(\frac{1}{b^{(2-D)n}} \cdot \cos(2\pi b^n x + \theta_n) \right) \quad (\text{Eq. 1})$$

$W(x)$ is defined for $x \in [-1 ; 1]$. D is the fractal dimension and ranges from 1 for a totally smooth curve to 2 for a band. b is an extra parameter greater than 1. η^2 is the standard deviation. The random phases, θ_n , are uniformly distributed over $[0 ; 2\pi]$. Truncation of the summation to a number of modes N_1 yields a deterministic realization of the random function.

Some examples of Weierstrass functions are presented on Fig. 2.

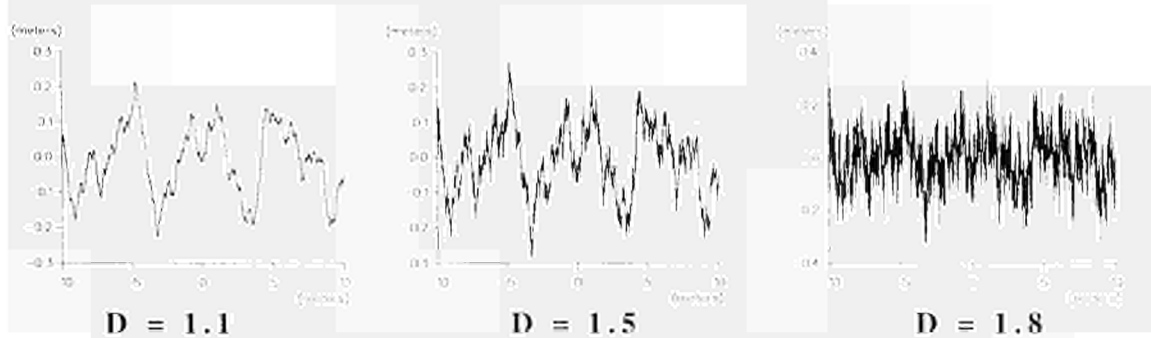


Fig. 2 : Weierstrass Functions { $b=(\pi)^{1/2}$; $\eta=0.2$; $N_1=120$ }

1.3. EXTRACTION OF THE FRACTAL DIMENSION

1.3.1. Box counting method

The box counting method is the most employed method to calculate the fractal dimension of a function. However, to increase its accuracy, we have to complete the usual process. Worth to be noted that it could be applied to any set of points (function, surface, volume...) [Lo 93] [Falconer 93]. We consider here the case of the fractal study of a function.

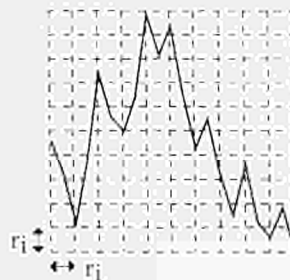


Fig. 3: The box counting method

The signal is first normalized in both coordinates, which does not modify the fractal dimension [Lo 93]. For a more complete characterization of a curve, the amplitude should be considered as well.

A square grid is then superimposed on the signal. The edges r_i of the cells are multiples of the sampling rate where i ranges from one to the number of samples. The number N_i of squares of dimension r_i , necessary to cover the entire signal, is counted (in gray on Fig. 3). The box counting method is based on the definition:

$$\ln N_i = -D \cdot \ln(r_i) + c \quad (\text{Eq. 2})$$

By definition, **D is the fractal dimension of the signal. Also, if the above linear relationship exists for a curve, then this curve is fractal.** The slope of the least squares straight line of the $\{-\ln(r) ; \ln N(A,r)\}$ set is known to be a good estimate of the fractal dimension.

Study of the curve $\{-\ln(r) ; \ln(N)\}$

The process is explained with the example of the Weierstrass function which is plotted in Fig. 2 with the following parameters:

$$\{ b=(\pi)^{1/2} ; \eta=0.2 ; N_1=120 ; D=1.5 \}$$

The curve \mathcal{C} ($\ln(N)$ plotted versus $-\ln(r)$) and the least squares line are shown on Fig. 4. Abscissa axis is oriented from high to low values of r . Two portions of the curve are obviously moving away from the least squares line :

- For little boxes, the local slope tends towards 1. It is a consequence of sampling : when box size is close to the sampling length, curve looks smooth. This problem was discussed by [Chen 93b] who has proposed a minimum value r_{min} for r :

$$r_{min} = \frac{L_{max}}{M^{1/D}} \quad (\text{Eq. 3})$$

where L_{max} is the length of the signal, M is the total number of samples and D is the fractal dimension of the signal. An important remark is that D is used to calculate r_{min} , and also D is dependent on r_{min} . So, D should result from an iterative process.

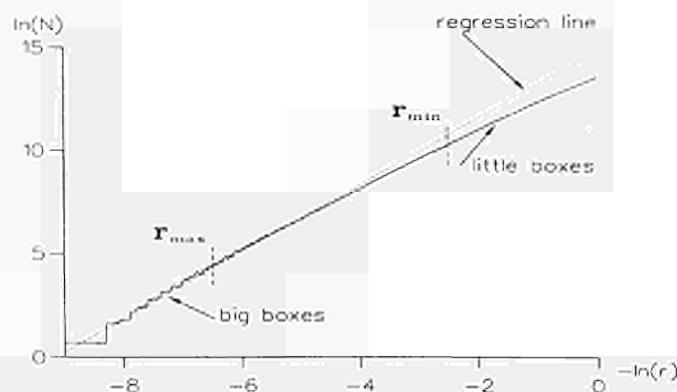


Fig. 4: Plot of $\{-\ln(r) ; \ln(N_i)\}$ and least squares line

- For large boxes, the curve \mathcal{C} shows some staircase steps. In fact, when the size r of the edges increases, some boxes overshoot the graph. This problem actually exists for any box size but, for large edges, only a few of them are necessary to cover the signal and so, the influence of this overshoot is stronger.

To counter this effect, it is possible to select box sizes which avoid overflowing. For example, if the signal is defined on $[0 ; 1]$, a widespread solution consists in considering box edges r_i such as:

$$r_i = 2^{-i} \quad (\text{Eq. 4})$$

Unfortunately, in this case, the \mathcal{C} plot does not contain enough points to allow an accurate determination for the least squares line.

We have used an interesting solution to this problem proposed by [Tricot 87] which consists in weighting the box sizes by their effective area. Nevertheless, not all discontinuities disappear and an upper limit r_{\max} for r_i must still be introduced.

Consequently, we have to determine the lower limit r_{\min} and the upper limit r_{\max} of the \mathcal{C} plot. On the other hand, we need to plot the least squares line with as many points as possible. To realize the best tradeoff, a new parameter is introduced : the correlation coefficient (CC) in the least squares sense. The closer to 1 the CC is, the straighter the curve. The next paragraph explains how to use the CC for improving the box counting method.

1.3.2. The box counting method implementation

Let us illustrate it through the same example of §1.2 with $M = 8000$ samples and $D = 1.5$. Implementation of the box counting method involves the following iterative steps :

1st step : r_{\min} is set to $r_{\min} = 1$: the smallest edges are equal to the sampling rate. Then, r_{\max} can take values ranging from $r_{\min}+1$ to M . For each r_{\max} , slope and CC are calculated on the curve restricted to $[r_{\min} ; r_{\max}]$. Then, a double diagram can be plotted (Fig. 5) :

$$\begin{cases} \text{fractal dimension} = \text{slope} = f(r_{\max}) \\ \text{correlation coefficient} = g(r_{\max}) \end{cases} \quad \text{for a given } r_{\min} \quad (\text{Eq. 5})$$

The fractal dimension appears to be strongly dependent on r_{\max} , and the box counting method accuracy will be improved if convergence of D versus r_{\max} is reached.

It is worth noting that the CC remains close to 1 for short values of r_{\max} , and drops for larger values. The most convenient value $r_{\max|}$ of r_{\max} is just before the decay of the CC plot because it includes the greater number of points with the best CC. Meanwhile, on the fractal dimension curve, D takes the value D_r . Both values are kept for the next step.

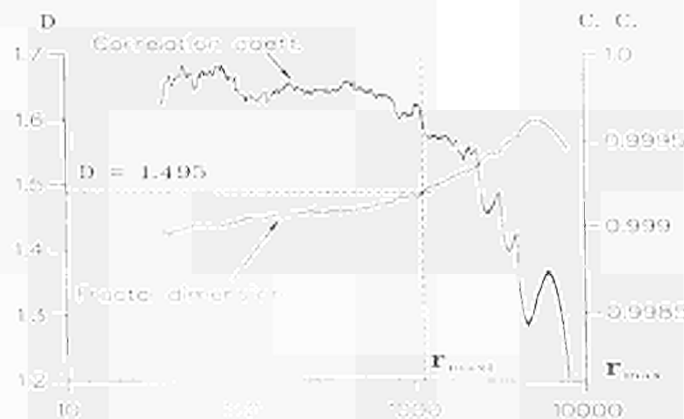


Fig. 5: Double diagram : slope / correlation coefficient = $f(r_{\max})$

2nd step : First estimate of the lower limit is then (Eq. 3) :

$$r_{\min 2} = \frac{N}{N^{1/D_1}} \quad (\text{Eq. 6})$$

Then, the first step may be reiterated until convergence is reached for D estimation. We could check that this one is obtained with 2 to 4 iterations.

To test the accuracy of this improved box counting method, we computed the fractal dimension of Weierstrass functions : for each fractal dimension, 50 sets are generated. Both mean value and standard deviation are calculated for D (see Table 1) :

Table 1 : Comparison of theoretical and calculated fractal dimensions

Theoretical Dimension	Calculated Dimension (Mean)	Standard deviation (%)
D = 1.3	1.30	0.48%
D = 1.5	1.50	0.34%
D = 1.7	1.66	0.22%

It appears that fractal dimension calculated with the improved counting box method is very close to the theoretical fractal dimension of the Weierstrass function. The standard deviation does not exceed 0.5%. Difference between expected values and results increases with D because of sampling : the more D increases, the more samples are needed. If sampling is not sufficient, the curve is smoother and D is lower.

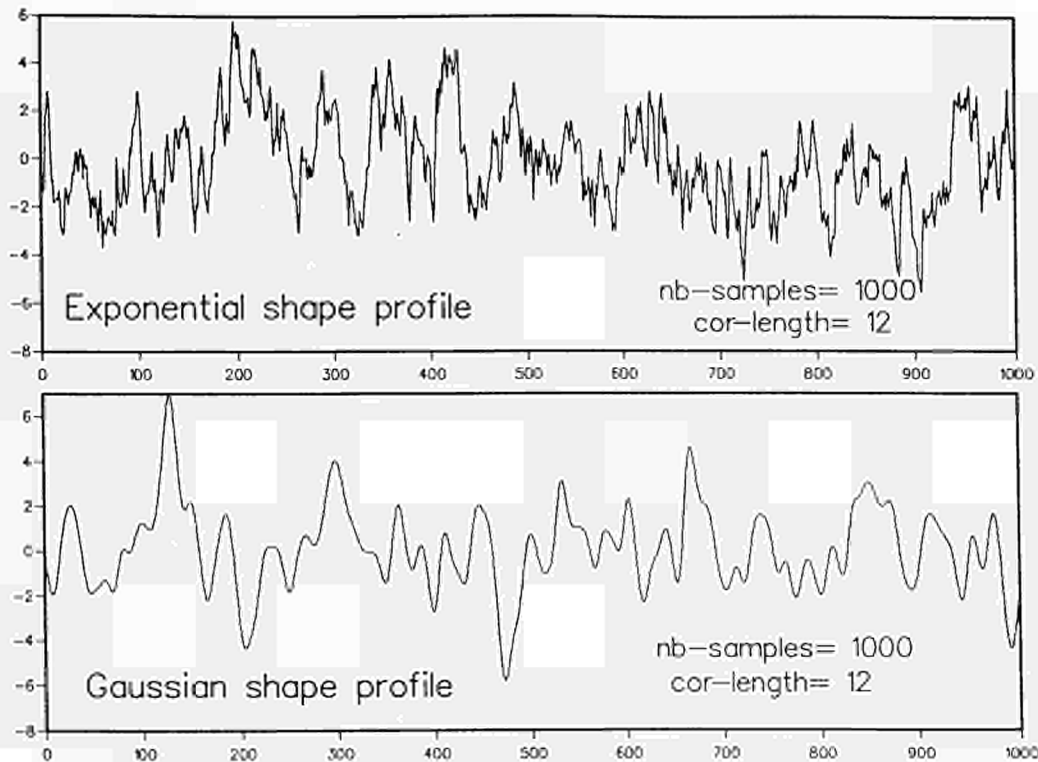
1.4. RELATIONSHIPS BETWEEN THE FRACTAL DIMENSION AND THE SURFACE CORRELATION FUNCTION.

1.4.1. Assessment of the relationship in the case of generated profiles

Once new approaches of surface roughness characterization have been introduced (here the fractal approach), it might be useful to compare them with the traditional roughness description based on the surface correlation function. This study is of particular interest, especially when asymptotical surface scattering models (e.g. Kirchhoff approach or the Integral Equation Method) are considered. In this case actually, the knowledge of the surface correlation function (including the correlation length) is a prerequisite. Consequently, the purpose of this section will be primarily to investigate the fractal behavior of stochastic profiles, and subsequently to assess the relationships between the fractal dimension and the surface correlation function.

However, the first step is to determine to what extent a stochastic profile exhibits a fractal behavior. For the ease of the study, we will consider hereafter only normalized random stochastic profiles (the r.m.s. height $s=1$). Note that the r.m.s. height is simply a term of normalization with no effect on the fractal behavior. Using a moving average process (MAP), which consists in filtering a set of independent realizations of a Gaussian, centered, unitary random process $N(0,1)$, we can easily generate stochastic random profiles of any statistics, in terms of output auto-correlation function [Ogilvy, 1991]. As an example, Fig. 6.a and 6.b display two examples of bi-dimensional profile realizations, for a Gaussian and Exponential surface correlation function, respectively. In both cases, the correlation length (normalized with respect to the profile sampling step) is assigned to 12, and the number of samples (10000) is chosen large enough, so that to avoid any spurious effect related to the profile finite length. It can be easily observed that beyond the correlation length value, the shape of the correlation function is a parameter of most concern for the profile outlook.

Subsequently, the box counting method has been applied to the generated gaussian and exponential profiles. Fig 7 displays the curve \mathcal{E} obtained in the two cases. The exponential profile indicates a behavior close to a fractal (\mathcal{E} is shown to be a straight line), with a fractal dimension estimated around 1.65. For the sake of comparison, Fig. 7 also displays the curve \mathcal{E} obtained from a Weierstrass profile of the same fractal dimension. Considering the gaussian profile, the curve \mathcal{E} obtained is not a straight line. Hence, we check the non fractality of the gaussian profile.



Figures 6.a and 6.b : exponential and gaussian profiles

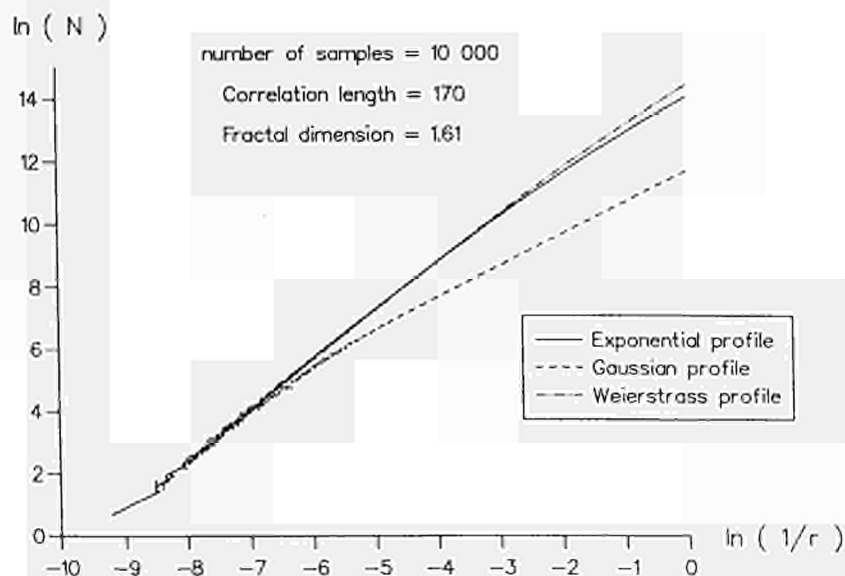


Fig 7 : \mathcal{E} curve of Exponential, Gaussian and Weierstrass profiles

In the exponential case, the previous analysis points out that it makes sense to investigate the relationship between the fractal dimension and the correlation length. Consequently, the fractal dimension of several exponential profiles generated through the *MAP* have been calculated. Fig. 8 displays their fractal dimension versus the correlation length (3 independent realizations have been generated for each correlation length). We notice a negative slope linear behavior of the fractal dimension versus the correlation length : the fractal dimension appears consequently to be a good candidate for the estimation of the correlation length.

1.4.2. Assessment of the relationship in the case of experimental profiles

Using a needle-like profiler, experimental profiles acquired over agricultural soil surfaces have been analyzed. The length of these profiles ranges between 3 and 9 meters, with a sampling step of 1.5 cm in the horizontal direction. The experimental surface correlation functions have indicated exponentially-like shapes, the same conclusion being reported in most of the studies dedicated to agricultural soil surface profile analysis. Consequently, it makes sense to derive a fractal dimension. The fractal dimension estimates range between 1.3 and 1.65, depending on the roughness state.

Fig. 9 displays the fractal dimension estimate versus the correlation length estimate. It is to point out that, due to experimental limitations (especially the available profile length), estimators of both fractal dimension and correlation length may not be very accurate. However, like for the generated profiles, we retrieve a decreasing trend, with an overall linear behavior.

1.4.3. Preliminary conclusions

Both simulated and experimental profiles have indicated a linear behavior relating the fractal dimension to the correlation length. However, further investigations are required in order to investigate to what extent the fractal behavior, and the fractal dimension in a further step, can be efficient indicators of the surface correlation function. In addition, further experimental analysis should also assess the respective accuracies of the fractal dimension and correlation length estimates, with respect to the measurement features : length of the profile, sampling step, accuracy of the measurement.

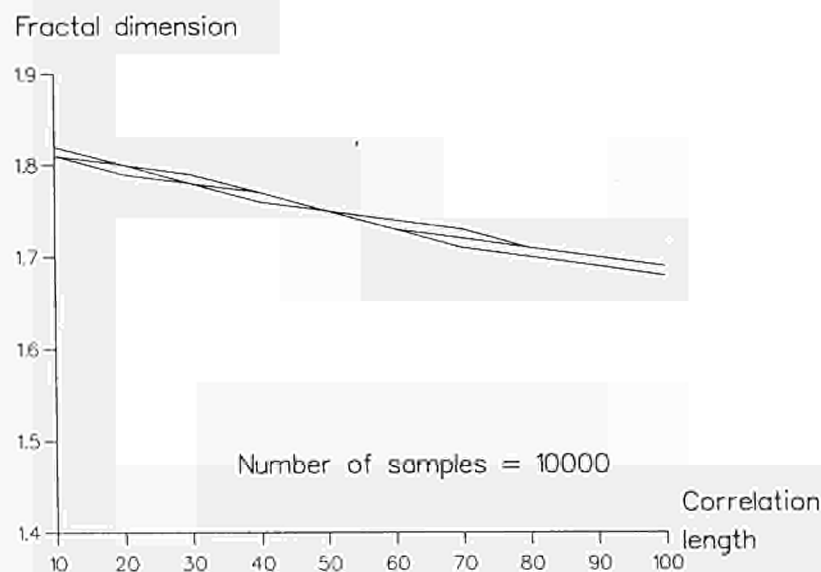


Fig 8 : Relationship between the fractal dimension and the correlation length of three exponential profiles

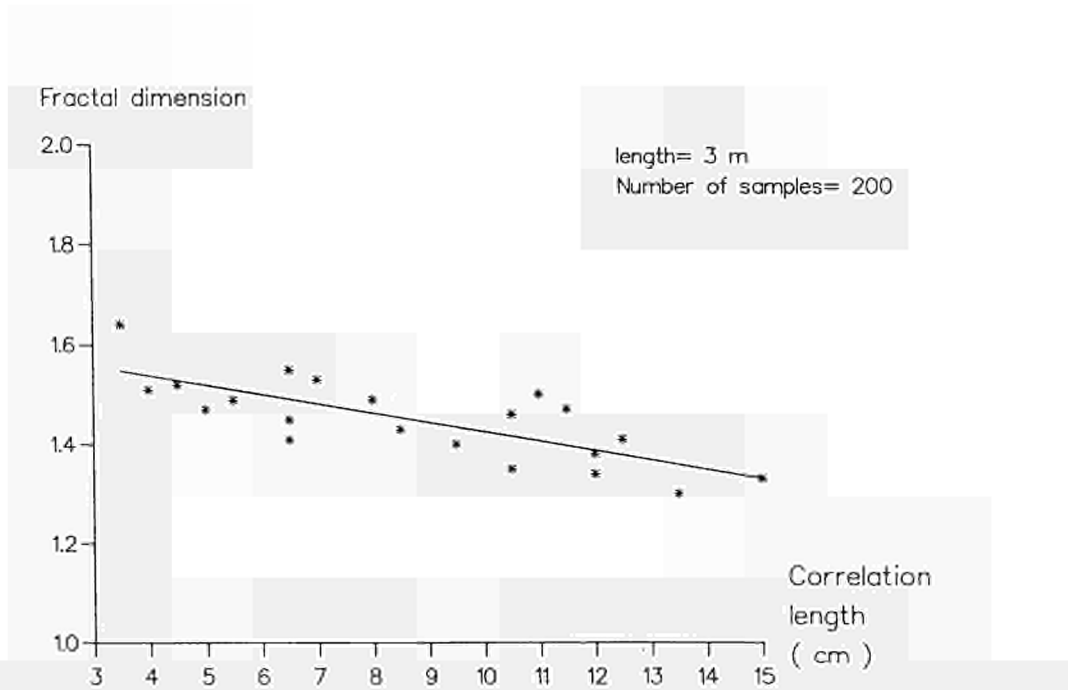


Fig 9 : Relationship between the fractal dimension and the correlation length of experimental profiles

2. COMPUTATION OF THE FIELD SCATTERED BY A BIDIMENSIONAL PROFILE

2.1. INTRODUCTION

Relatively simple analytical solutions exist which have different regions of validity, in terms of roughness conditions. Back to 1951, Rice developed a theory to obtain the polarization dependence of the scattering from slightly rough surfaces [Rice, 1951], which is in a way similar to the more generalized small perturbation method (SPM). This perturbation theory requires small surface rms. height and slope with respects to the wavelength. In 1967, Valenzuela extended Rice theory up to the second order for the estimation of the depolarization of electromagnetic waves from slightly rough surfaces [Valenzuela, 1967]. When the surface roughness is such that the correlation length and the average radius of curvature are much larger than the wavelength, the basic assumption of the Kirchhoff approximation (KA) is that a plane boundary reflection occurs at every point of the surface [Beckman et Spizzichino, 1963. In the high frequency limit, the Geometrical Optics (GO) approximation assumes that only the facets with appropriate orientation with regards to the incident wave (i.e. the facets which are normal to the incident beam) contribute to the scattered signal. Finally in 1992, a backscatter model has been developed based on an approximate solution of a pair of integral equations for the tangential surface fields [Fung et al., 1992]. Both like and cross-polarized scattering coefficients can be calculated.

However, all the above-mentioned models present the following defects : 1) They do not deliver phase information. 2) All of them have limited validity range. 3) They are based on a simplified surface description. Indeed, they directly respond to point 1) and can be used as references for points 2) and 3). For these reasons, the method of moments, based on the exact resolution of Maxwell equations, are introduced.

2.2. PEC PROFILE : METHOD OF MOMENTS

2.2.1. Frequency domain

The scattered field will be calculated using the **method of moments** [Harrington 68]. Indeed, an exact method of resolution is necessary because of the profile roughness. For sake of computational simplicity, we have limited the calculation to a 2-D metallic profile. The incident wave can be plane or cylindrical and a radiation pattern can also be defined. TE or TM cases can be considered. There is no restriction on the location of source and observation points in the upper half space. Edge effects will be neglected.

In the TM case, with the $e^{j\omega t}$ convention, Maxwell equations lead to :

$$\nabla^2 E_z + k^2 E_z = j\omega\mu J_z \quad (\text{Eq. 7})$$

The expression of the solution is as follows :

$$E_z^s(\vec{\rho}) = -\frac{k\eta}{4} \int_c J_z(\vec{\rho}') \cdot H_0^{(2)}(k|\vec{\rho} - \vec{\rho}'|) dl' \quad (\text{Eq. 8})$$

where $H_0^{(2)}$ is the Hankel function of the second kind, zero order, and η is the intrinsic impedance. Other notations are indicated on Fig. 10.

Rigorously, this integral would need a theoretical approach taking into account the very peculiar character of fractal curves which by nature are of infinite length and we should demonstrate convergence property of this integral. Actually, we have checked this point numerically. But simple physical considerations permit to explain this convergence: the scattered field for a given wavelength λ is not sensitive to details whose size is lower than a given threshold. Then the levels of details below this threshold are not seen any more by the electromagnetic waves and can be approximated by a smooth curve leading to a finite length.

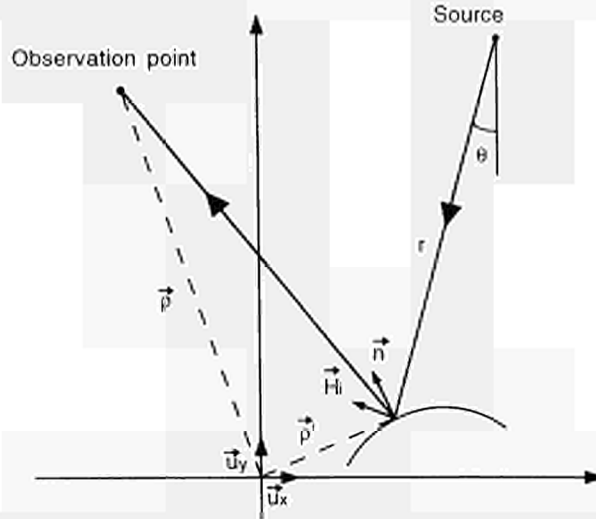


Fig. 10 : Calculation of the scattered field - notations

The profile is divided into N segments ΔC_n . The unknown current J_z is expanded on pulse functions:

$$J_z(\vec{\rho}) = \sum \alpha_n \cdot f_n(\vec{\rho}) \quad (\text{Eq. 9})$$

with :

$$f_n(\vec{\rho}) = \begin{cases} 1 & \text{on } \Delta C_n \\ 0 & \text{on other } \Delta C_m \end{cases} \quad (\text{Eq. 10})$$

Then, using the method of moments, we solve the integral equation [Harrington 68] expressing the boundary condition on the profile and using (Eq. 8):

$$\begin{array}{c} E_z = E_z^i + E_z^s = 0 \\ \left. \begin{array}{c} \downarrow \quad \uparrow \quad \uparrow \\ \text{incident} \quad \text{scattered} \end{array} \right\} \text{on the profile} \end{array} \quad (\text{Eq. 11})$$

2.2.2. Time domain

The method of moments needs 10 samples per wavelength to be accurate. Then we can address bidimensional profiles 20 meters long up to 10 GHz. As the UWB incident field contains several frequencies, we match the number of unknowns to the frequency and lately the solutions (J_z in TM polarization) are interpolated in space and frequency before computing the resulting diffracted field, first in the frequency domain and then in the time domain by Fourier transform.

2.3. DIELECTRIC SOILS : FDTD

FDTD looks to be the most appropriate rigorous method to model electromagnetic diffraction by dielectric soils. Indeed, it may cope with the detailed model of a soil (surface roughness, volume *heterogeneities*) as well as take into account arbitrary constitution and shape of possible embedded scatterers. Another advantage of FDTD is its ability to take into account large computational volumes due to its computational power. As it is a time domain technique it is readily matched to UWB radar simulations for example ground penetrating radar (GPR) studies for buried objects scattering computations [Jaureguy 96]. When it is followed by a Fourier transform giving the corresponding frequency domain response, it may address remote sensing problems of limited size or in bidimensional geometry.

We have then implemented a bidimensional FDTD code which can compute the field scattered in a volume composed of 2 semi-infinite media separated by a rough interface and which may include possible scatterers, and which can address typical length of several meters with pulses covering DC to 10 GHz bandwidth.

Implementation is based on Yee's leapfrog algorithm with Mur second order absorbing conditions and Taflove's corner ones [Mur 81] [Taflove 89]. Dielectric and magnetic losses of materials are taken into account conventionally through real electric and magnetic conductivities. Frequency dispersion in soils has to be considered here because for the pulses which are able to penetrate significantly soils, complex dielectric permittivities vary substantially. Possibility of taking into account the presence of such dispersive materials with either Debye or Lorentz models [Luebbers 93] is necessary to describe soils behavior. We could check that a 4 poles Lorentz model fit the complex permittivity of a clay soil containing 5% water [Jaureguy 96].

Main improvements of this classical algorithm are the following :

- subgridding : To be precise and avoid significant numerical dispersion artifacts, FDTD should be uniformly meshed. But the high sampling rate in space and time, imposed by the shortest significant wavelengths included in the pulse spectrum, is also inversely proportional the optical index of the material. Then if either the scatterer or the surrounding medium include high permittivity samples, use of uniform structured mesh become very shortcoming in terms of memory storage and time computation. For this ,we have implemented local mesh refinements by power of 2 by extending Yee's subgridding technique [Zivanovic 91] based on interpolation in space and time. We could check that such an interpolation introduced low level spurious reflections at their crossing which of course

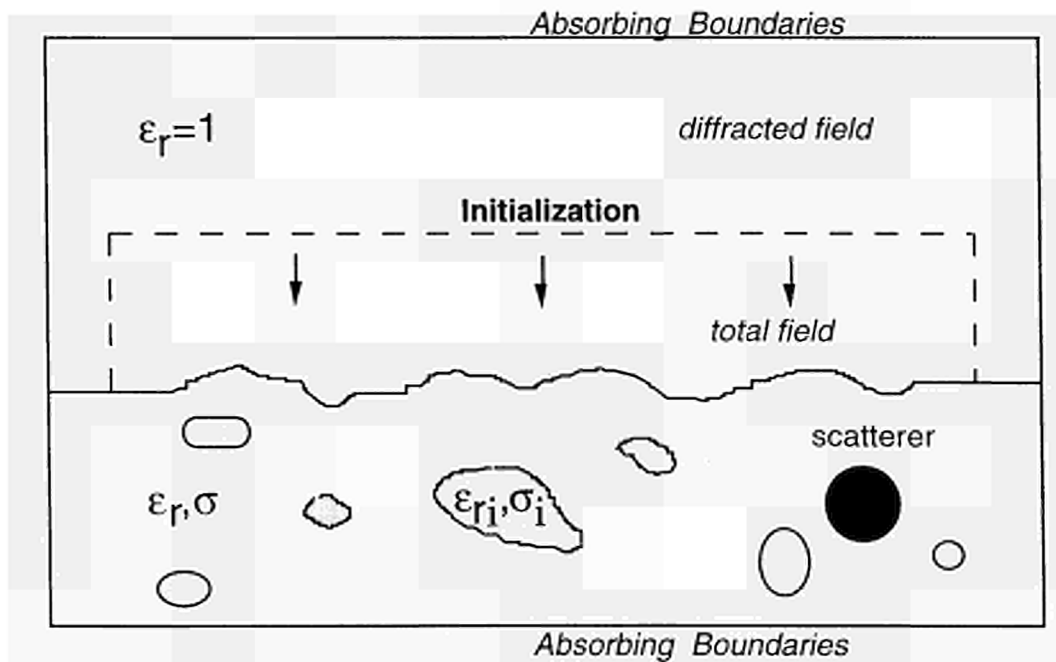


Fig. 11: Geometry of dielectric soil scattering

depend on the size of the subgridded zone. We could check as well that the levels of these spurious reflections induced by a subgridding by 4 were nearly identical to those induced by a mere subgridding by 2, all this being coherent with theoretical predictions [Jaureguy 95]. At last, this subgridding technique counters the traditional drawback of FDTD of not conforming to curved boundaries because of staircasing effects : when staircases are substantially reduced in size, grid conform to boundaries of scatterer or to the rough interface in question.

- *absorbing boundaries* : As we want to simulate short plane pulse scattering of a subsurface scatterer or evaluate scattering due to surface or volume scattering for a given stochastic process, we need the computation to be free of spurious numerical reflections at the artificial boundaries. Classical absorbing boundaries adapted to the host medium under the homogeneous assumption were found to work well even if this medium is lossy and then used in both of the semi-infinite media. Special points at the junction between the upper and lower absorbing boundaries at the interface were found to introduce no significant spurious diffractions. Nevertheless, when a plane wave impinges an interface and penetrates the host medium, it may be still very energetic when it reaches the lower absorbing boundary which, as well known, is not perfect. When the host material is lossy enough, this natural absorption combined with MUR's ones are sufficient to insure a parasitic level of reflection inferior to say -80 dB. When it is not the case, we add a rectangular slice of broadband radar absorbing material of intrinsic impedance that of the host medium and dielectric and magnetic loss angles following within the slice a gaussian law, which insures the same performances on this spurious level. Berenger's PML were implemented as well in the 2 media but they require more storage.

3. FRACTAL DIMENSION OF THE SCATTERED FIELD

3.1. INTRODUCTION

Profiles are generated by Weierstrass functions with the same parameters as §1.1 and $M = 1500$, $x_{\min} = -10$ meters, $x_{\max} = 10$ meters, $D \in \{1.1 ; 1.5 ; 1.8\}$. They are shown in Fig. 2.

We are going to consider pulses defined from very low frequencies to 9 GHz. First, we consider a spectral window which is defined by a Rayleigh function centered at 3 GHz. The incident pulse is described in Fig. 12 and its spectrum in Fig. 13. We have considered as well a rectangular spectral window. Frequencies involved in the profile spectrum are shown in Fig. 13.

3.2. RESULTS

Fractal dimension of the profile is noted D_p and fractal dimension of the scattered field is noted D_s . Let us first consider a TE plane wave normal to the profile. Monostatic far field observation is assumed.

Fig. 14 shows \mathcal{E} graphs for scattered field. Behavior observed in Fig. 4 for the fractal profile itself is retrieved for the scattered field. Discontinuities in the lower range and the slope limit in the upper range appear more quickly than for the profile itself. Indeed, smallest scales are rubbed out by the pulse window and now the change in slope is due to physical resolution instead of sampling considerations. From now on, we will limit our analysis of the \mathcal{E} curve before this limit, i.e. in the part of the curve where a unique fractal dimension can be defined.

D_s is a monotonous function of D_p . The interval $D_s \in [1.45 ; 1.77]$ is smaller than the initial interval $D_p \in [1.1 ; 1.8]$ but it is sufficient to distinguish the 3 fractal dimensions, thanks to the accuracy of the fractal dimension extraction method.

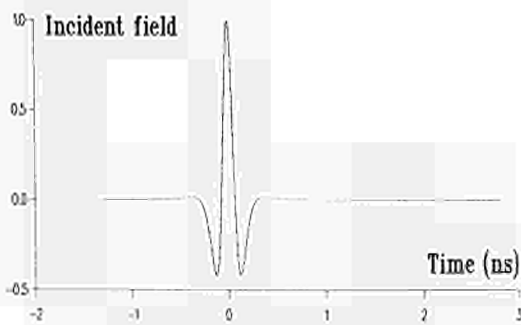


Fig. 12 : Incident wave (temporal curve)



Fig. 13 : Incident wave (spectral curve) and spectrum of Weierstrass profiles

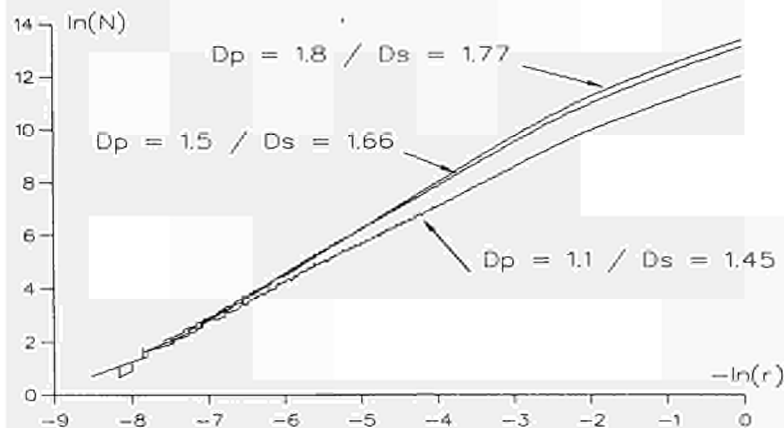
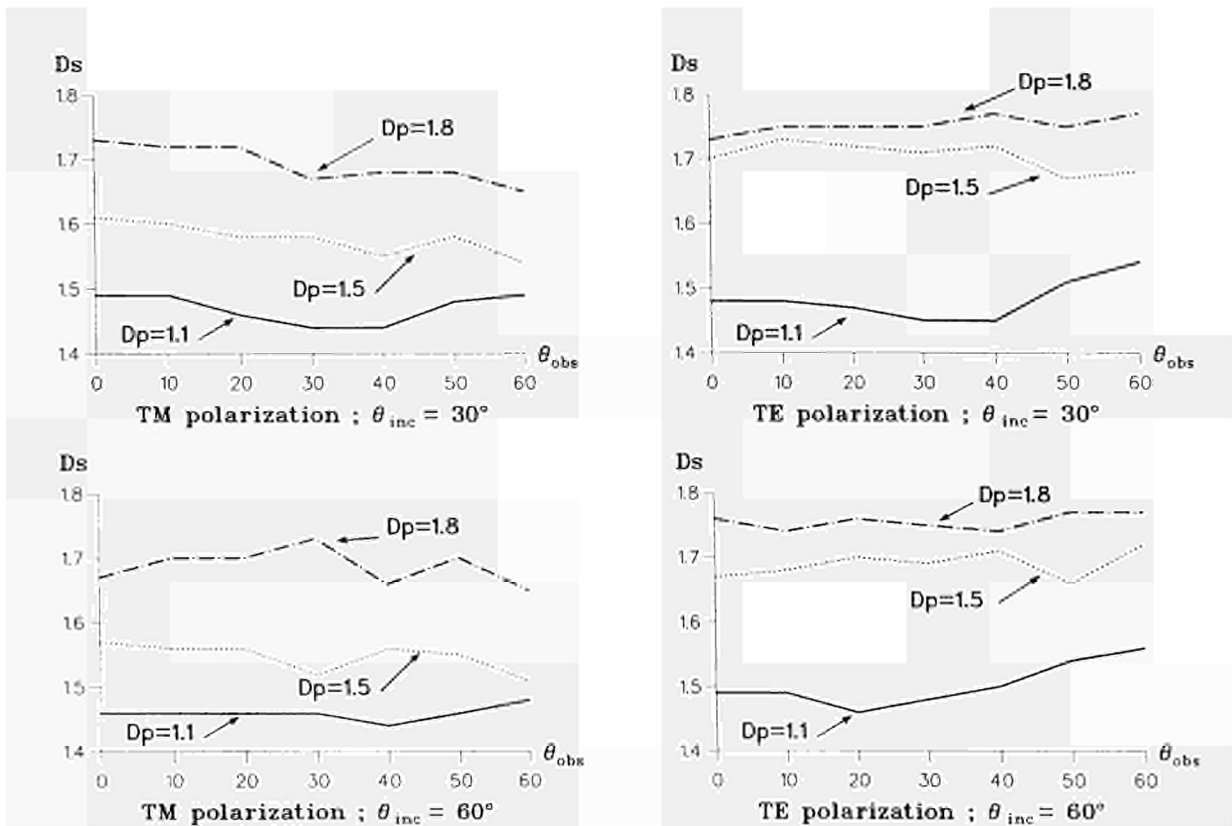


Fig. 14 : Fractal dimension of the scattered far field ($\theta_i=0^\circ$, $\theta_{obs}=30^\circ$)

Fig. 15 shows the evolution of D_s for different observation angles and for different incidence angles. Both TE and TM cases are considered. The incidence angle is equal to 30° or 60° .

We can note the following conclusions :

- For a given polarization, D_s is nearly constant with regards to observation and incidence angles.
- D_s is a monotonous increasing function of D_p .
- We can also note that for small or medium values of D_p , D_s is much larger. This increase can be analyzed by multiscattering effects. Indeed, a ray method like, for example U.T.D. [Kouyoumjian 74], considering only single diffractions would yield a scattered signal which duplicate all the wedges of the profile itself, and there would be no reason to obtain D_p different from D_s . Method of moments, in nature, incorporates single and multiple scattering events and the increase in D_s may be interpreted as the account for this multiple scattering contribution. This is well physically understandable, because multiscattering makes the impulse response of the profile much rougher than the duplication of the low fractal dimension profile. It is to notice that these multiscattering events in the short pulse regime have both high frequency and low frequency features, and thus they cannot be accounted for uniquely on a multi-diffraction ray basis.
- For high values of D_p , D_s becomes closer to D_p . Again, it looks understandable because now the multiscattering contributions interact with a profile rough by itself and so are less sensitive. Furthermore, they compete with the "shadow" effects. At last, in the zone of very high fractal dimensions, counting box method gets saturated by nature.



**Fig. 15 : Fractal dimension of the scattered far field
Study of the influence of observation and incidence angles and of polarization**

Fig. 17 shows a very good behavior of D_s with regard to noise. It does not disturb D_s until a level of 10 dB signal to noise ratio. Moreover, fractal dimensions remain separated until 0 dB level. We can remark that for high noise levels, D_s tends to be equal to the noise fractal dimension counting box result extraction. This result logically should be 2 (like for surfaces), but due to unavoidable sampling effects, counting box method saturates to 1.85, which is a common feature of all very high fractal dimensions.

3.5. DIELECTRIC PROFILES

Previous study on PEC fractal profiles should now be extended to dielectric rough profiles.

Actually, only water surface can be reasonably considered as PEC at centimeter wavelengths. This study can be done using FDTD simulations. At this time such a study has not yet been done in a systematic way. Nevertheless Fig. 18 displays the \mathcal{C} curves of dielectric fractal profiles ($\epsilon_r=9$) for an observation point in the near field above the interface.

We can see that there is still a correspondence between the profile fractal index and the one of the diffracted field, but that this influence is less important than in the case of a PEC profile, and that the point at which slope is changing is much earlier. These features look very logical because small scale details are much less sensitive in the dielectric case. Further studies should assess which informative content can be derived from such regression curves in the case of variable dielectric permittivities but from now on one may think that not only the slope but the curvature point as well should be pertinent for this.

4. CONCLUSION AND FUTURE PROSPECTS

Fractals have been considered from several points of view.

Concerning surface representation, they have been applied to experimental measurements as well as compared to other usual stochastic representations. While stressing that such confrontations should be pursued and completed for complete assessment, these first results show that fractal representation of rough surfaces might be a rather good descriptor in some cases.

We have shown on canonical perfectly conducting examples that if a profile is fractal then the scattered field in the time domain is fractal too. Corresponding fractal dimensions are different but the

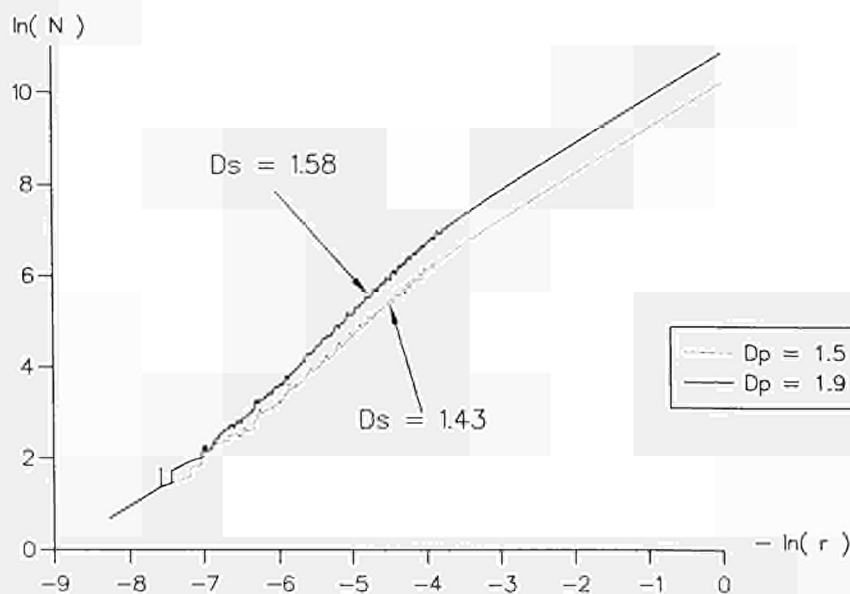


Fig. 18 : \mathcal{C} curves for dielectric profiles

order relation is preserved. Moreover the fractal dimension of the scattered field weakly depends on the direction of incidence and observation. Some differences are observed between TE and TM cases. Noise influence was also studied and the fractal characterization appears to be robust on this point. Consequently, fractal dimension of time domain scattered field seems to be a relevant parameter for characterization and classification of natural scenes.

Among others, this work should be pursued on the following aspects:

1) Characterization of soils: further assessment on the usefulness of fractal approach to characterize soils are necessary from a practical point of view.

2) Extension of this study to dielectric surfaces on a systematic way

3) Extension to real 3D surfaces

Actually, even if we plan to address these points from a *theoretical* point a view, *coupling* these results with *experiments* on soil structures, on scattered field and on relationships between them, would be of primary interest. These experiments can be of both types. First of them consists in working with real world soils in order to refine the pertinence of soil surface description. Second kind of experiments is related to the scattered field characterization in relation with soil properties. This latter should be developed in laboratory environment with very well controlled conditions. Consequently, there is a need for a surface generator coupled with experimental facilities, preferentially UWB. At this time, Ispra JRC facilities are for sure the most appropriate to meet these requirements.

BIBLIOGRAPHY

- [Beckmann 63] Beckmann, P., A. Spizzichino, *The scattering of electromagnetic waves from rough surfaces*, Macmillan, New-York, 1963.
- [Besicovitch 34] A.S. Besicovitch, *Sets of fractional dimensions*, J. Lond. Math. Soc., vol. 9, 1934
- [Blackledge 92] J.M. Blackledge, E. Fowler, Fractal dimensions segmentation of synthetic aperture radar images, *International conference on image processing and its applications* (Maastricht, Netherlands), pp. 445-449, 7-9 April 1992
- [Borgeaud 95] Borgeaud, M., "Analysis of bare soil surface roughness parameters with ERS-1 SAR data", *Proceedings International Symposium : Retrieval of BIO- and Geophysical parameters from SAR data for Land Applications*, Toulouse, France, October 10-13, 1995.
- [Bouligand 29] G. Bouligand, Sur la notion d'ordre de mesure d'un ensemble plan, *Bull Sc. Math.*, 1929
- [Bourissou 94a] A. Bourissou, K. Pham, J. Levy-Vehel, A multifractal approach for terrain characterization and classification on SAR images, *PIERS*, pp. 223, July 1994
- [Bourissou 94b] A. Bourissou, K. Pham, Une méthode de classification en deux étapes d'images SAR polarimétriques utilisant des concepts de la géométrie fractale, *Colloque International sur le Radar*, Paris, pp. 309-312, May 1994
- [Chen 93a] J. Chen, T. Lo, J. Litva, Time varying fractal surface scattering, *PIERS*, 1993
- [Chen 93b] S.S. Chen, J.M. Keller, R.M. Crownover, On the calculation of fractal features from images, *IEEE Trans.-Pattern Anal.-Mach.-Intell.*, vol. 15, n°10, pp. 1087-90, 1993
- [Costes 94] F. Costes, I. Chênerie, T. Le Toan, N. Boudier, J. Lemorton, *PIERS 94*, Noordwijk, Netherland, July 11-15 1994
- [Falconer 93] K. Falconer, *Fractal geometry mathematical foundations and applications*, John Wiley & Sons, 1993
- [Fung 92] Fung A.K., Z. Li and K.S. Chen, "Backscattering from a randomly rough dielectric surface", *IEEE Trans. Geosci. Remote Sensing*, vol. 30, no. 2, pp. 356-369, March 1992.
- [Harrington 68] R.F. Harrington, *Field computation by moment method*, The Macmillan company, New York, 1968
- [Hausdorff 19] F. Hausdorff, Dimension und äusseres Mass, *Math. Annalen*, vol. 79, 1919
- [Jaggard 90a] D.L. Jaggard, On Fractal Electrodynamics, Recent advances in Electromagnetic Theory, *Springer-Verlag*, pp. 183-222, 1990
- [Jaggard 90b] D.L. Jaggard, X. Sun, Fractal surface scattering: a generalized Rayleigh solution, *J. Appl. Phys.*, vol. 68, n°11, pp. 5456-5462, December 1990
- [Jaureguy 95] M. Jaureguy, Etude de la diffraction par impulsions électromagnétiques très courtes d'objets en espace libre ou enfouis: modélisation numérique et extraction des paramètres caractéristiques, *thèse de l'ENSAE*

- [Jaureguy 96] M. Jaureguy, P. Borderies, Modeling and processing of ultra wide Band scattering of buried targets, *Detection of abandoned land mines*, 7-9 October 1996, Conference Publication N° 431
- [Keller 89] J.M. Keller, S. Chen, R.M. Crownover, Texture description and segmentation trough fractal geometry, *Computer vision, graphics and image processing*, vol. 45, n°2, pp. 150-166, February 1989
- [Kouyoumjian 74] R.G. Kouyoumjian, P.H. Pathak, A uniform geometrical theory of diffractaion for an edge in a perfectly conducting surface, *Proc. of the IEEE*, vol 62, n° 11, November 1974
- [Le Mehauté 90] A. Le Mehauté, *Les géométries fractales*, Hermès, 1990
- [Lo 93] T. Lo, H. Leung, J. Litva, S. Haykin, Fractal characterisation of sea-scattered signals and detection of sea-surface targets, *IEE Proceedings*, vol. 140, pp. 243-250, n°4, 1993.
- [Luebbbers 93] R. Luebbbers, D. Steich, K. Kuntz, *IEEE Tr. AP*, vol. 41, n°9, 1993
- [Mandelbrot 84] B.B. Mandelbrot, Fractals in physics: squig clusters, diffusions, fractals measures, and the unicity of fractal dimensionality, *Journal of Statistical Physics*, vol. 34, n° 5-6, pp. 895-930, mars 1984
- [Mur 81] G. Mur, *IEEE Trans. Electromagn. Compat. EMC-23*, 377-382, 1981
- [Ogilvy 91] J.A. Ogilvy, Theory of wave scattering from random rough surfaces, *Adam Hilger*, 1991
- [Prusinkiewicz 90] P. Prusinkiewicz, A. Lindenmayer, Fractal properties of plants, *The algorithmic beauty of plants*, Springer-Verlag, 1990
- [Rice 51] Rice, S.O., "Reflection of electromagnetic waves from slightly rough surfaces", *Commun. Pure Appl. Math.*, vol. 4, pp. 351-378, 1951.
- [Rouvier 95] S. Rouvier, P. Borderies, I. Chênerie, *Electromagnetic scattering of a fractal profile: direct and inverse problems*, Symposium international sur l'extraction de paramètres bio-géophysiques à partir des données RSO pour les applications terrestres, 10-13 October 1995
- [Rouvier 96] S. Rouvier, P. Borderies, I. Chênerie, J.C. Souyris, T. Le Toan, N. Flourey Fractal analysis of ploughed soils profiles and application to electromagnetic scattering of soils.(IGARSS'96)
- [Stewart 93] C.V. Stewart, B. Moghaddam, K.J. Hintz, L.M. Novak, Fractional brownian motion models for synthetic aperture radar imagery scene segmentation, *Proceedings of the IEEE*, vol. 81, n°10, pp. 1511-1522, October 1993
- [Taflove 89] A. Taflove, K.R. Umashankar, *PIER 2*, Finite element and finite difference methods in electromagnetic scattering, chap. 8, 1989
- [Tricot 87] C. Tricot, J.F. Quiniou, D. Wehbi, C. Roques-Carmes, B. Dubuc, Evaluation de la dimension fractale d'un graphe, *CRM-1465, Université de Montréal*, May 1987
- [Valenzuela 67] Valenzuela, G.R., "Depolarization of EM waves by slightly rough surfaces", *IEEE Trans. on Antennas and Propagation*, vol. AP-15, n°4, July 1967.
- [Zivanovic 81] S.S. Zivanovic, K.S. Yee, K.K. Mei, *IEEE Trans. on microwave theory and techniques*, vol. 39, n°3, 1991

EXPERIMENTS ON PRECIPITATION DETECTION AND SOIL MOISTURE MEASUREMENTS

M. MARTIN-NEIRA
European Space Agency, ESTEC
PO.Box 299
2200 AG Noordwijk
The Netherlands

ABSTRACT. This paper is concerned with new measurement techniques for the space Earth remote sensing of two geophysical parameters which are central in the global water cycle, namely precipitation and soil moisture.

1. Introduction

For the mapping of soil moisture at global scale from space the European Space Agency (ESA) is conducting a feasibility study on MIRAS, a Microwave Imaging Radiometer using two dimensional Aperture Synthesis. An aircraft breadboard of this instrument is currently being integrated and will be flown in Spring 1997. This paper introduces the MIRAS spaceborne instrument describing briefly the prototype and the results achieved following its final integration [1].

A new measurement technique for the detection of precipitation is also introduced. The concept is based of a Focused Wide band millimeter wave Interferometer (WINTER-F) comprising two different observation points. The two observing points, phase synchronized, perform near field interferometry by passive (radiometer) and active (radar) means. Experiment results carried out so far are shown. More tests on the fundamentals of this concept are expected to be performed at EMSL.

2. MIRAS

2.1 SCIENTIFIC OBJECTIVES

The main scientific purpose of MIRAS instrument is the measurement of soil moisture. The knowledge of soil moisture is essential in surface hydrology, in the computation of evaporation and is central in life, biogeochemical cycles and global food production. In addition soil moisture is needed to extend precipitation forecasts over continental areas and to study climate variability. Overall soil moisture measurements, at global scale, would provide a major input to global hydrology and would be extremely useful for quantitative models of biomass production.

Over ocean MIRAS can measure the salinity if the sea water temperature is obtained from another sensor independently. Ocean salinity variations can be used to observe the thermohaline circulation and the energy exchange with the atmosphere, both important in global climatology.

2.2 SPACEBORNE INSTRUMENT

Based on the experimented potential use of aperture synthesis (Le Vine 1990), ESA initiated in 1992 the study of the MIRAS spaceborne instrument directed towards the demonstration of the feasibility of two dimensional aperture synthesis for measuring the Earth soil moisture and ocean salinity from space. The result of this activity has been the definition of a baseline configuration of the instrument which is briefly described here.

MIRAS receives the thermal radiation coming from the Earth surface in the protected microwave frequency band between 1400 and 1427 MHz (in L-band). The nominal orbit which has been chosen to define the baseline configuration is the one of ENVISAT, i.e. 800 km altitude. In order to achieve a reasonable spatial resolution of a few tens of km at this low frequency band MIRAS performs aperture synthesis, a technique which has been used in radioastronomy for several decades now. Aperture synthesis allows to synthesize a large aperture from a number of small antennas by cross correlating the field received by them. The set of cross correlations is then related to the brightness temperature of the scene viewed by the small antennas basically through a Fourier transform, which can be performed on ground.

The antenna of MIRAS has been optimized to avoid aliasing effects with the minimum number of small apertures possible. The baseline configuration consists of three arms of 8.3 m in length, co-planar, spaced by 120° . The boresight direction is tilted 31.2° ahead nadir in order to image co-incidence cones from 40° till 55° within a swath of 900 km. The small antennas have dual polarization to resolve the soil moisture from the soil physical temperature. Over ocean though, an independent measure of sea surface temperature is required to retrieve the ocean salinity, which could be provided by a contemporary mission with an instrument of the type of MIMR (Multifrequency Imaging Microwave Radiometer).

Every arm of MIRAS antenna is composed of a linear array of 43 small apertures with a diameter of 0.89λ and adjacent to each other. In addition there is an element at the intersection of the three arms plus other 3 in between the arms which are used for phase restoration, a technique intended to compensate for phase biases between receiving chains based on phase closure relationships. In total MIRAS antenna has 133 small apertures.

Every small antenna is connected to an L-band receiver which performs low noise amplification of the signal, pass-band filtering, in-phase (I) and quadrature (Q) down-conversion and 1-bit quantization. The two polarizations are measured sequentially every 300 ms and periodically the input of the receiver is switched onto two reference signals, one correlated and the other uncorrelated among different receivers, for calibration purposes. The local oscillator and the sampling clock of every receiver are derived from a 54 MHz reference clock signal input.

The three receivers connected to the antenna elements used for phase restoration have a power splitter before the quantizer. One of the splitter outputs serves to sense the total brightness temperature of the scene which is used to normalize the 1-bit correlations. In this branch the receiver behaves as a conventional total power radiometer. The two reference loads are provided by the correlated and uncorrelated noise inputs before the first low noise amplifier. In these three receivers the generation of the reference noise inputs is carefully designed to provide the required calibration accuracy.

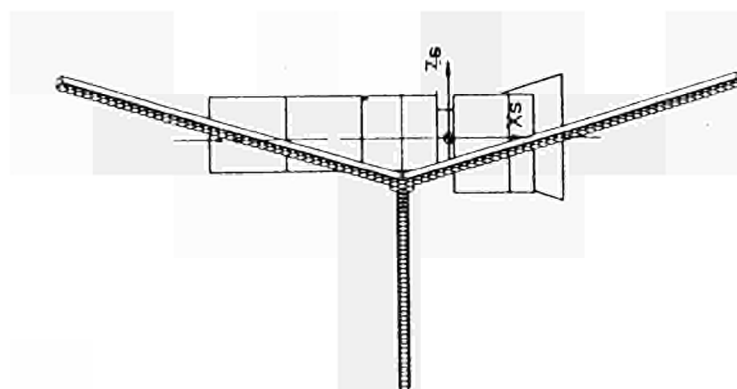


Figure 1: MIRAS Spaceborne Instrument

The 43 receivers of every arm are multiplexed in 10 groups of 4 receivers and 1 group of 3 receivers by 11 multiplexers which convert the 8 or 6 1-bit parallel receiver outputs into optical signals and transmit them in serial to a central demultiplexer unit. The 3 receivers for phase restoration and the receiver at the antenna node are also multiplexed together. The multiplexers receive also the 54 MHz reference clock optical signal from the central demultiplexer unit, convert it to electrical and distribute it to the group of attached receivers. There are thus one uplink and one downlink optical fiber per multiplexer. Other lines are foreseen within the signal harness as those providing the supply to the remote receivers, the control of the calibration/polarization switch and others dedicated to thermal monitoring.

The central demultiplexer unit receives the 34 optical fiber inputs from all the multiplexers and converts them into 133 I and Q electrical 1-bit digital signals. These are then fed to the correlator unit. The demultiplexer also generates the 54 MHz reference clock, converts it into an optical signal and then splits it among the 34 uplink optical fibers which go into the multiplexers.

The correlator unit performs an alignment of the 133 I and Q incoming digital signals and then the cross correlation, at the origin of time, of all possible pairs of signals, without repetition. The total number of 1-bit digital correlators is therefore 17556. The result of every correlation is then output as a 2 byte word at a data rate of about 300 kbps.

The spatial resolution of the MIRAS spaceborne instrument varies over the swath with a best value of $20 \times 27 \text{ km}^2$ and a worst value of $51 \times 30 \text{ km}^2$. The radiometric resolution over the integration time of 2.5 s corresponding to one pixel is 3 K and this reduces to 0.8 K when the maximum available integration time of 35 s is used in the image processing. The estimated total mass of MIRAS is 230 kg and the estimated power consumption 296 W. Figure 1 shows the MIRAS spaceborne instrument.

2.3 AIRCRAFT BREADBOARD

As a result of the activity mentioned above a prototype has been built to be flown on board an aircraft during a flight campaign next Spring 97. This breadboard is working at the same frequency and has the same configuration as the spaceborne instrument but with only 3 elements per arm and 1 element for phase restoration. Together with the element at the node the prototype has 11 antenna elements and its arms measure 0.65 m roughly. The reference clock signal is distributed through optical fiber but, unlike the spaceborne version, the I and Q samples are connected through coaxial cables to the correlator unit which includes only the required 110 correlators. For the calibration both a correlated and uncorrelated noise inputs are provided.

The MIRAS breadboard is mounted on a structure which can interface with the pallet of the rear ramp of an Hercules C-130 aircraft. The structure provides the translation and rotation motion needed to have the instrument pointing 45° behind the aircraft nadir direction from the open ramp. The measured spatial resolution of the breadboard is 18° which, when flying at an altitude of 1 km, gives a ground resolution $260 \times 370 \text{ m}^2$ over a swath of 4 pixels, i.e. 1 km. The measured radiometric resolution is 0.6 K and the radiometric accuracy is 3 K. Figure 2 shows the MIRAS aircraft breadboard.

3. The WINTER-F System for Precipitation Observations

3.1 THE WINTER-F CONCEPT

The Winter-f (mm-Wave wide band INTERferometer - Focused) concept, which was first developed for a passive system, comprises the following main theoretical basis [2]:

- a radiometer system performing interferometry in near field can have range resolution much in the same way as a radar does;

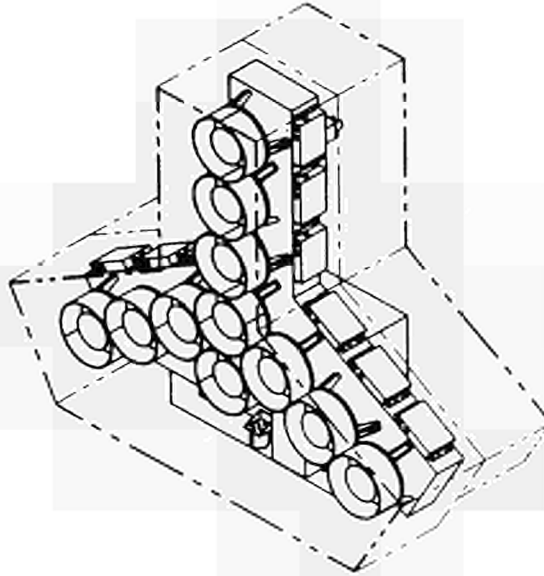


Figure 2: MIRAS Aircraft Breadboard

- range resolution in one direction is achieved by decorrelation;
- range resolution in another direction is obtained by doppler processing.

When these theoretical basis are applied to a spaceborne passive system for Earth remote sensing the following theoretical results are found:

- the signals from ground and the continuous atmosphere can be filtered out by selecting a proper spatial frequency (receivers baseline) of observation;
- the signals originated by hydrometeors (both through scattering and emission) can be observed by the properly chosen observation baseline;
- the output of the passive system is proportional to the density of hydrometeor particles (i.e. rain rate) free of contamination from the background (ground and continuous atmosphere).

The same concept can be applied to an active system (radar) where time gating can be performed. In this case we have a third degree of freedom and the spatial resolution in the third dimension becomes possible.

3.2 RESULTS OF THE SENSITIVITY STUDY

The sensitivity of a spaceborne system based on the WINTER-F concept for precipitation observations has been studied in detail. A constellation of two small satellites, phase synchronized by the GNSS (Global Navigation Satellite System) signals, performing near field interferometry by passive (radiometer) and active (radar) means has been analysed [3,4].

In the case of the passive system the amplitude of the signal due to the rain increases, for large baselines, with the square root of the number of drops (if they are all assumed with the same absorption cross section). This has to be compared with the output of a total power radiometer which is proportional to the number drops. The appearance of the square root behaviour in the WINTER-F system is due to the fact that the rain drops are chopped by many phase fringes when a large baseline is used and this makes the individual impulse responses to partially cancel among each other. This same mechanism is the one responsible for the washing out of any signal coming from a uniform background. Numerical computations of the amplitude of the rain signal for a realistic scenario show that the useful amplitude would be smaller than 1 mK which is well below the 100 mK sensitivity of present radiometer sensors.

The sensitivity in the case of an active system has also been studied showing that it is of the same order of magnitude of a conventional mono-static rain radar and therefore a properly designed active WINTER-F system should achieve an adequate signal to noise ratio. However, the same coherence between echoes from different rain drops which allows to reach a suitable sensitivity level in the active system makes it impossible to attain spatial resolution by decorrelation and by doppler when the baseline is large.

3.3 STUDY ON BASELINE LENGTH

All these results of extremely low rain signal in the passive system and impossible spatial resolution in the active system hold for large baselines. Therefore the baseline length and the variation of the main system parameters with it are currently being subject of further study. The results of this analysis are not available yet but we shall present the interest of considering the effect of changing the baseline length.

In the passive WINTER-F system using a long baseline the rain signal is low because of the rain drops are observed from many grating lobes at the same time. If all rain drops were observed by the same grating lobe their contribution would add constructively leading to a much stronger signal. This means that the size of the grating lobes should be that of typical rain cells, which, except for stratiform rain, is of about 4 km. Such wide grating lobes can be generated only with very short baselines. If in addition we want to achieve high beam filling factor from the typical rain cells, the antenna element diameter must be as large as possible, this is, equal to the baseline length. In this configuration we have then two antenna elements with $s/d=1$. In general, the number of grating lobes within the common footprint to the two antenna elements is given by twice the ratio between the spacing s and the diameter of the single antenna d , that is, $2s/d$. Therefore in the discussed configuration, we have 2 grating lobes where ideally one of them contains a rain cell and the other is empty, as depicted in Figure 3.

The concern in this new configuration comes from the background signal and its interaction with the rain drops. Reducing the number of grating lobes to only 2 makes the interferometer sensible to the corresponding spatial frequency component of the background. On the other hand, a detailed study has not been carried out on the effect of the mutual interaction between the rain drops and the background through attenuation, reflection and scattering mechanisms showing that the particles will be visible over the background, even when having the same brightness temperature of the background. An experiment in this direction would be very helpful to assess the capability of the short baseline WINTER-F system.

As regards the active system, a short baseline configuration has a great potential in terms of spatial resolution capabilities as compared to the long baseline case. This is mainly because the monostatic and

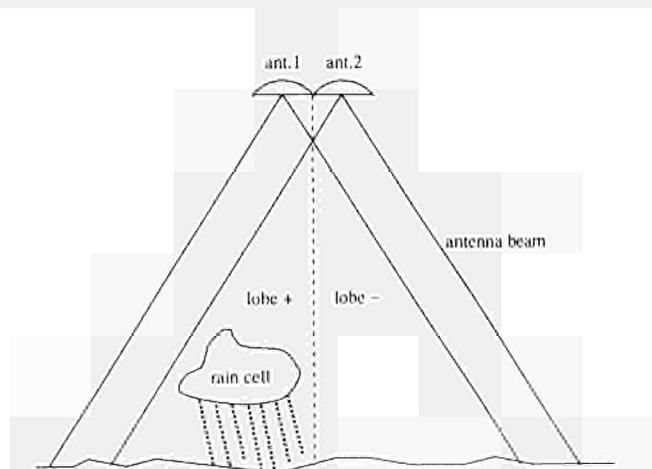


Figure 3: WINTER-F Short Baseline Concept

bistatic iso-range loci define greatly overlapping volumes. Besides the ground echo coming through the two grating lobes with opposite sign should be much smaller than the one which would be received by a monostatic radar. The on-going study will give more detailed results on the capabilities and advantages of this radar system as compared to a conventional monostatic radar system.

3.4 MEASUREMENT RESULTS

Several tests have been performed in the laboratory at 10 GHz which demonstrate the fundamentals described above of the WINTER-F concept. Also the good agreement found between the measured signal levels and the predicted ones has confirmed the lack of sensitivity of a satellite system using a long baseline as has been already discussed.

The first measurements were carried out on a “dry” target consisting of a cloud of particles of lossy rubber embedded in porexpan. The output of the interferometer cross correlator was consistent with the predictions, namely, null output for a uniform background (microwave absorber) and a given amplitude level, depending on the relative positions of the particles, when the particles were placed in between the interferometer and the uniform background. This proved the basics of the theory as well as the capability of the interferometer to detect the presence of particles in front of a background.

The second measurement used real water drops generated as an artificial rain inside the laboratory. The theoretical predictions and simulation expected results were again confirmed. The interferometer was able to detect the presence of water drops in front of the uniform background and the predicted effect of the falling velocity was observed using different integration times as shown in Figure 4. The number of drops simultaneously in view from the two antennas within the optimum integration time is estimated to be of less than 20. The low signal level of a few K even in this laboratory experiment limited the distance between the interferometer and the water drops to about 1.5 m.

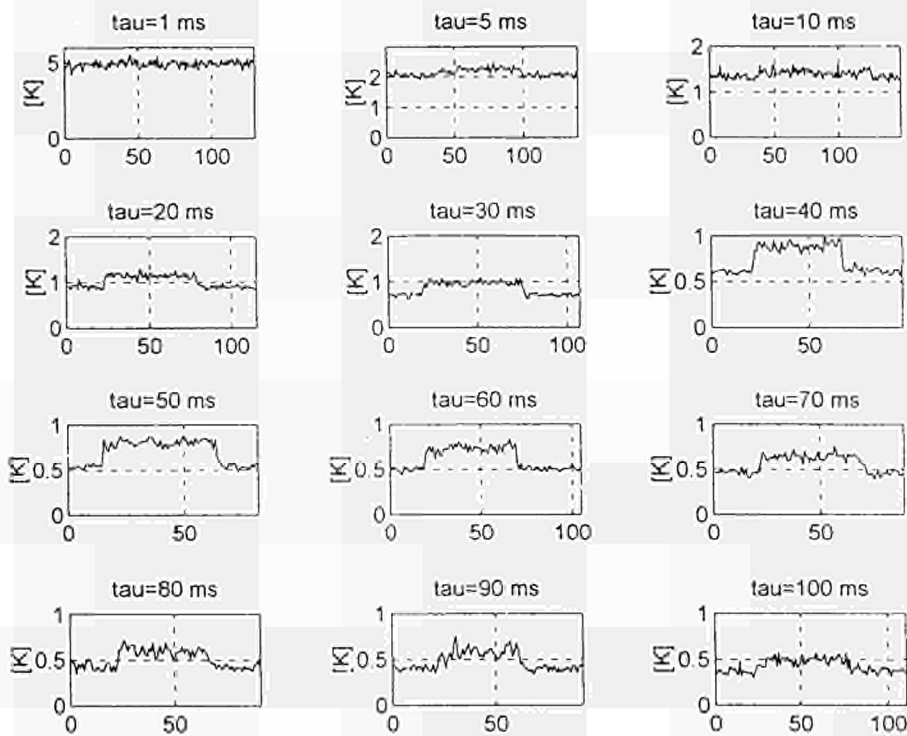


Figure 4: Amplitude of the cross correlation during an artificial rain event using different integration times.

The final measurement was done on a moving strip of lossy rubber to preliminary test the capabilities with respect to doppler discrimination. The strip, which was long in the direction perpendicular to the baseline and narrow along the baseline, moved along a circle in front of the interferometer. The results agreed perfectly with the theory showing a phase history of the complex cross correlation as expected from the traversing of the strip through the phase fringes. This result is shown in Figure 5 where the slope of the phase versus time is related to the speed of the strip.

4. Proposed Measurements in EMSL

4.1 EXPERIMENTS ON PRECIPITATION

Within the ESA study on the WINTER-F concept it is intended to perform experiments in the EMSL microwave laboratory. The definition of the experiments is still open but they will be directed towards the verification of the fundamentals of the WINTER-F concept, in particular the capability to perform spatial resolution by decorrelation and by doppler, as well as the test of the short baseline concept described above using an artificial rain generator already developed by JRC [5].

4.2 EXPERIMENTS ON SOIL MOISTURE

Although no provisions have been presently done to perform passive microwave L-band soil moisture measurements to test retrieval algorithms, this type of experiments would be helpful in the future development of MIRAS spaceborne instrument. The suitability of the anechoic chamber or another outdoor set-up facility would then have to be investigated.

5. Conclusions

An L-band Microwave Imaging Radiometer with 2 dimensional Aperture Synthesis (MIRAS) has been presented for the measurement of soil moisture from space at global scales which is strongly demanded by the scientific community.

The research on a Wide band mm-wave INTERferometer - Focused (WINTER-F) concept for the observation of precipitation from space has been described and initial results presented. An experiment on the concept will be carried out in the EMSL in the near future.

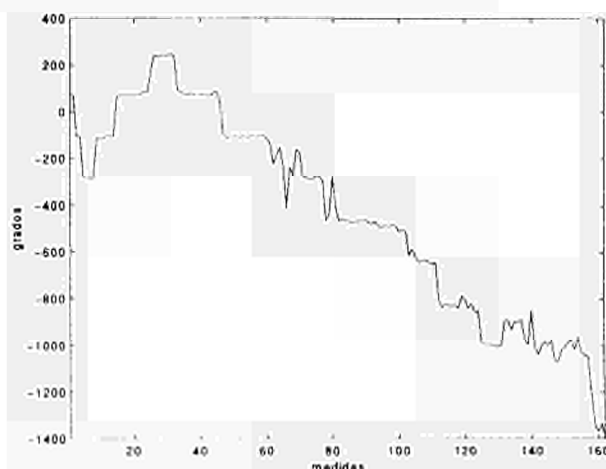


Figure 5: Phase history of the complex cross correlation of a moving target.

6. References

- [1] M.Martín-Neira et al, "*Theoretical Research on New Concepts for the Remote Sensing of Hydrometeors*", IGARSS-96 proceedings, Lincoln (Nebraska, US), pp 315-317.
- [2] M.Martín-Neira et al, "*Integration of MIRAS Breadboard and Future Activities*", IGARSS-96 proceedings, Lincoln (Nebraska, US), pp. 869-871.
- [3] J. Bará et al, "*Study on mm-Wave wide band Interferometry - Focused / Passive (WINTER-F / P)*", Department of Signal Theory and Communications of UPC, Barcelona (Spain), under ESA Contract No.10590/93/NL/JV with Officine Galileo (Italy), June 1996.
- [4] M.V. Arbolino et al, "*Study on mm-Wave wide band Interferometry - Focused / Active (WINTER-F / A)*", Dune, Rome (Italy), under ESA Contract No.10590/93/NL/JV with Officine Galileo (Italy), June 1996.
- [5] E. Olhmer et al, "*Rain Detection Experiments at the EMSL*", EMSL Newsletter, No.8, JRC, Ispra (Italy), June 1996.

EXPERIMENTAL PROPOSAL ON BACKSCATTERING ENHANCEMENT AND CLUSTERING EFFECTS ON ARTIFICIAL RANDOM MEDIA: APPLICATION TO BARE SOIL AND VEGETATION CANOPY

P. COPPO
*Centro di Telerilevamento a Microonde,
Via Panciatichi, 64
50127 Florence, Italy*

P. PAMPALONI
*CNR-IROE
Via Panciatichi, 64
50127 Florence, Italy*

P. BRUSCAGLIONI
*Dipartimento di Fisica,
Università di Firenze,
Via S.Marta, Florence, Italy*

1. Introduction

Backscattering enhancement has attracted significant interest in volume and surface-scattering problems: it is due to an effect of multiple scattering (the constructive interference of two waves travelling in opposite directions, which is not destroyed by randomness of positions of elements). An important quantity to be determined is the angular width of enhancement because it indicates whether the enhancement can be observed with a receiver of narrow angular width in active remote sensing, and also it affects passive remote sensing data because the surface emissivity is related to the bistatic scattering coefficient integrated over the upper half space.

While in the case of volume-volume interaction the angular width is usually very small (of the order of a degree), in the case of surface-surface and volume-surface interaction it can be on the order of 10-30 degrees. Whereas surface scattering conventional theories based on Physical or Geometrical Optics and on perturbation method cannot predict the enhancement, two approaches based respectively on the second-order Kirchhoff approximation (Sengers et al. 1995, Phu et al 1993, 1994) and on the Fung approximation (IEM) (Fung et al. 1996) with appropriate shadowing functions can explain this effect.

Backscattering enhancement can exist in volume-surface interaction where a double bounce can arise from one volume scattering and one surface scattering. It is a consequence of reciprocity and will not disappear as a result of the randomness of particle positions or the rough surface random heights. In vegetation canopies, the fractional volume of scatterers is low (usually between 0.1 and 0.5%), but often the scatterers, such as branches and leaves can occur in clusters. In these media, which can be described as "locally dense" media, collective scattering and absorption effects can be very important, and they cannot be studied with the classical vector radiative transfer theory, as it assumes that the particles scatter independently. This condition may not be satisfied for some natural media, such as branches and leaves in a vegetation canopy, where correlated scattering effects may appear if the relative distances between the scatterers are less than an electromagnetic (e.m.) wavelength.

In this case the radiative transfer theory must be modified to take into account these effects. In

a study carried out by L. Tsang et al. (Tsang et al. 1995 a, b) the volume is taken much larger than a wavelength and contains many particles so that the collective scattering effects of the particles within the volume are taken into account.

Validations of these models have been carried out in the 1D-dimensional case by using exact numerical methods (Method of Moment and MonteCarlo). On the other hand real surfaces and real vegetation may not well represent the approximations introduced by the models. Thus a first step for validation with experimental data can be that of measuring the backscattering from experimental models in indoor experiments. This approach allow one to control both the statistic and dielectric properties of the target, as well as the scattering measurements. Only a few experiments have been done with this technique for very rough surfaces in the range between 1 and 20 GHz, while to date no measurements have been done to study clustering effects in volume media.

The EMSL can be very useful to conduct experiments aimed at the validation of theoretical models. Because of its various capabilities of changing observation parameters (polarization, incident and observation angles, frequency), the EMSL allows one to obtain the accuracy and the repeatability of measurement not achievable in airborne or other ground based campaigns.

2. Objectives and significant aspects of the proposal

The proposed research aims at studying monostatic and bistatic scattering properties of isotropic and anisotropic random surface and volume media with particular emphasis on the backscattering enhancement. The objective will be pursued by means of monostatic and bistatic scattering measurements of various targets at different illumination and observation angles.

Such experimental investigation, besides being an extension of an experiment already performed at the EMSL for the study of scattering from non-vegetated terrains, is also an innovative research which well fits in with international activities of other researchers. Indeed we think that it will be possible to explain the high values of backscattering found in many experimental data acquired from airborne or satellite (SARX-SIRC) platform at higher frequencies (C and X bands).

3. Investigation approach

The proposed research includes the following activities:

- 1) Review of the State of the Art on surface and volume backscattering enhancement,
- 2) Implementation of physical models (for surface and volume scattering) predicting backscattering enhancement,
- 3) Realization of two experimental models:
 - a - random rough dielectric (or metallic) surfaces (surface media),
 - b - set of nearly vertical cylinders with different densities and clustering (volume scattering media),
- 4) Scattering measurements at the EMSL,
- 5) Comparison of model(s) with experimental data.

Surface scattering from very rough surfaces (isotropic and anisotropic case) will be studied by measuring the bistatic and the monostatic scattering coefficient in scatterometer and SAR mode. The measurements will be carried out on metallic and dielectric surfaces expressly designed with

- A.K. Fung, C.Y. Hsieh, G.Nesti, A. Sieber, P.Coppo, (1996), " A Further Study of the IEM Surface Scattering Model", Proceedings of IGARSS'96, 27-31 May, 1996, Lincoln, Nebraska, USA, vol.IV, pg.2116-2118.
- L.Tsang, K.H.Ding, G.Zhang, C.C. Hsu, J.A. Kong, (1995 a), "Backscattering Enhancement and Clustering Effects of Random Distributed Dielectric Cylinders Overlying a Dielectric Half Space Based on Monte-Carlo Simulations", IEEE Trans. on Antennas and Propag., vol.43, N.5, May 1995, pg.488-499.
- L.Tsang, J.A. Kong, Z.Chen, K.Pak, C.Hsu, (1995 b), " Theory of Microwave Scattering From Vegetation Based on the Collective Scattering Effects of Discrete Scatterers", in "Passive Microwave Remote Sensing of Land-Atmosphere Interactions", Editors: Choudoury, Kerr, Njoku, Pampaloni, USP Press, Utrecht, The Netherland, 1995.

PROPOSAL FOR AN EXPERIMENTAL INVESTIGATIONS OF SOIL RADIO PHYSICAL PROPERTY PECULIARITIES ON SOIL MOISTURE CONTENT.

N. V. RUZHENTSEV
Radio Astronomy Institute
of National Academy of Science
310002, 4 Krasnoznamennaya Str., Kharkov
The Ukraine

ABSTRACT. The article turn attention to the weak clarity about radio physical properties of the small and middle moisture soil. In view of this the hypothesis explained some peculiarities of dependence of radar signal on soil moisture as well as the directions of carrying out of additional investigations this problem are offering.

1. Introduction

In spite of many papers deal with investigations of soil radar cross section (RCS) and soil radio brightness temperature (T_b) there is number of questions required additional investigations.

From one aspect a cause of such situation is limited field of the questions which were examined by some of research teams as well as differences in methods and conditions of the measurements. I have in mind a limited wave band, angle ranges and polarization as well as limited set of types of soil that were investigated. Besides the investigations were worked out either in active or in passive regime of sounding and it render difficult for development of complex active - passive Remote Sensing method.

From other aspect many papers did not attract enough attention to significant questions of the soil test-specimen parameters control. This cause leads to difficulties in comparing of data were obtained by different authors. It render more difficult for comparison of measured data too.

2. The main point of problem

Before to turn to essence of the article it is a meaning to turn to some results of one of activity directions of our research group at latter years [1-3]. In all probability it will be useful for understanding of primary source of the offered programme investigation in the project.

During number years the angular, polarization and frequency dependencies of RCS and T_b for different types of earth covers and atmosphere conditions at millimeter waveband were investigated by Remote Sensing of Environment research group from Radio Astronomy Institute of NAS of Ukraine (RI NAS). We used 94 GHz and 136 GHz at active regime of sounding as well as 39 GHz and 94 GHz at passive regime. At that

the radiometer measurements were realized with using a measuring tower, a sea shore and a helicopter. The scatterometer measurements were realized with using the measuring tower only. As result, if discuss the bare soil data, we have examined test-specimens of sand and black earth, but more detail - the surfaces of black earth. Figure 1-2 show angular dependencies of black earth RCS (warm and frozen) that we have got for different grades of soil humidity and surface roughness. These measurements were realized with five characters of polarization at 2 mm and 3 mm waves band.

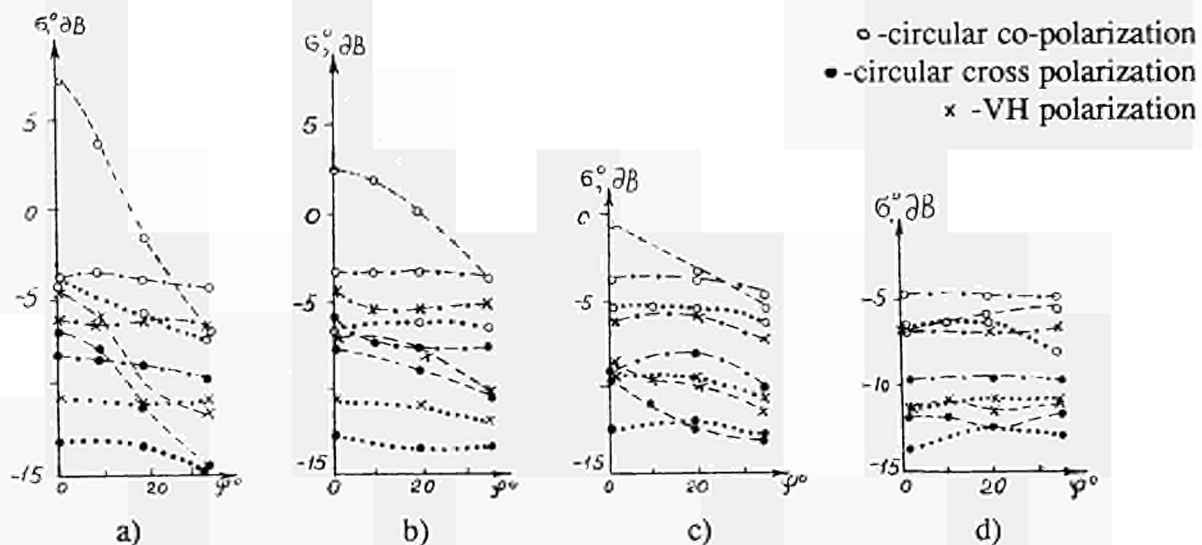


Figure 1. Angular dependence of RCS of bare soil (black earth).

a - $d_h = 0.9$ mm; b - $d_h = 4$ mm; c - $d_h = 11$ mm; d - $d_h = 35$ mm; dash curves- 25 % of weight moisture capacity; dot curves - 15 %; dash-dot curves - 4%. (2-mm range)

The dependencies of ratio of co-polarization RCS to cross-polarization RCS on soil humidity (Figure 3a) as well as the dependencies of RCS value on soil humidity for different polarization (figures 3b) were constructed using the data obtained by us.

These dependencies have "turning" in curves that are unexpected for us if judge from point of view of wide spread theories which supposes the increase of soil humidity cause increase of soil permittivity and as result - increase of soil RCS value. These "turnings" we observed on both frequencies, on every polarization and observing angles.

Similar "turnings" in RCS dependencies on soil humidity are found by us in one of articles by Dr. F. Ulaby [4]. It has results of measurement of loam surface RCS at 7GHz. Figure 4 is took from [4].

Besides the investigations of the radio brightness temperature on soil moisture carried out by us for analogous kinds of soil show such nonlinearity of curves at small and near middle signs of soil moisture (Figure 5).

Showed "turning" examples at dependencies of RCS (m) and T_B (m) evoke a question: Why this peculiarity writings absences in most of experimental publications of different authors who interesting in such field ? As it can judge this situation explanation might be connected with the most of authors studied three - four moisture values only (dry soil, middle and much moisture) as well as with using of control of volume soil humidity only or using of sand specimens only for the experiments. Indeed the every of these causes might to screen that phenomenon.

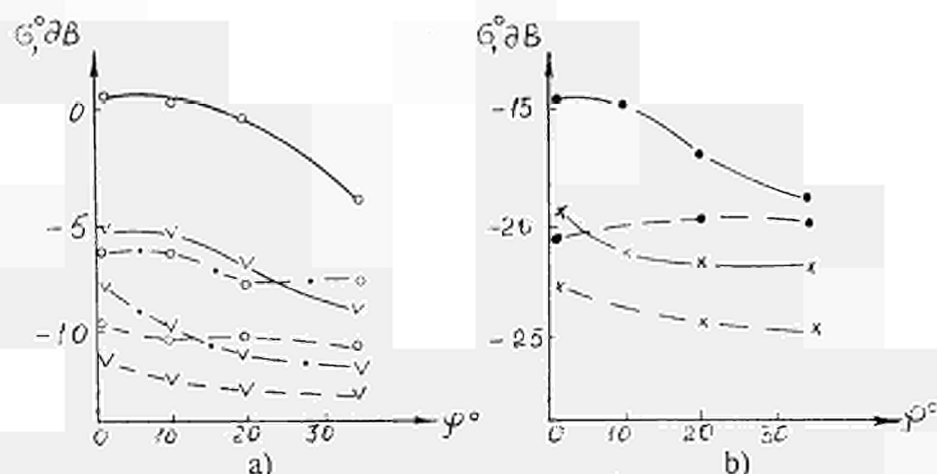


Figure 2 Frozen soil angular dependence of RCS (3-mm range).

Dash curve - $d_h=35\text{mm}$, $m=13\%$; solid curve - $d_h=4\text{mm}$, $m=24\%$; dash-dot curve - $d_h=35\text{mm}$, $m=23\%$; \circ -black earth (VV polarization); \bullet -black earth (VH polarization); ∇ -frozen black earth (VV polarization); \times -frozen black earth (VH polarization);

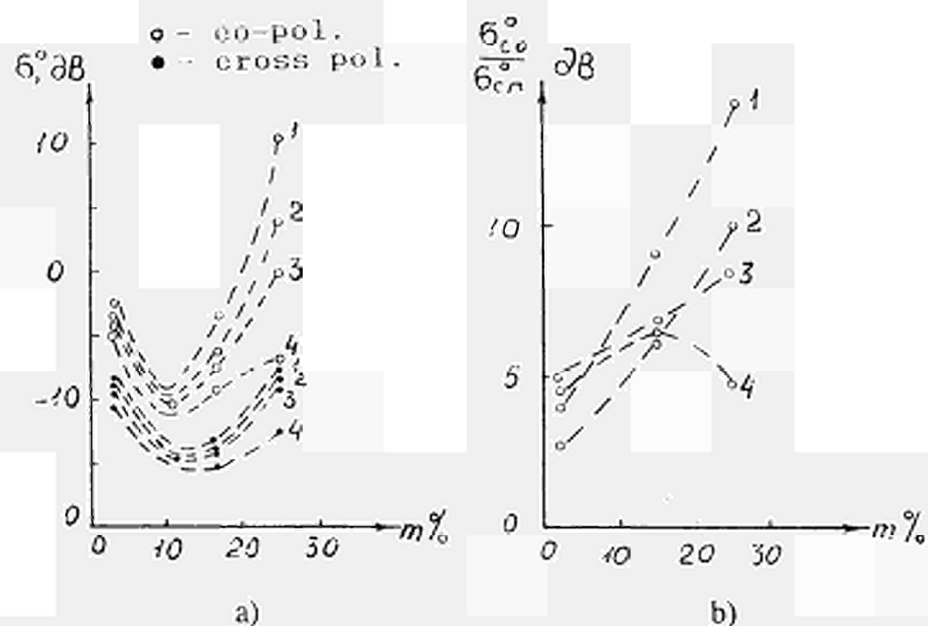


Figure 3. Soil dependencies of RCS and RCSco/RCS cross ratio on weight moisture capacity (2-mm range).

1 - $d_h=0.9\text{ mm}$; 2 - $d_h=4\text{ mm}$; 3 - $d_h=11\text{ mm}$; 4 - $d_h=35\text{ mm}$;

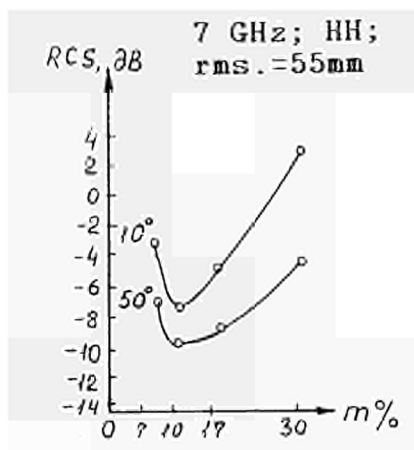
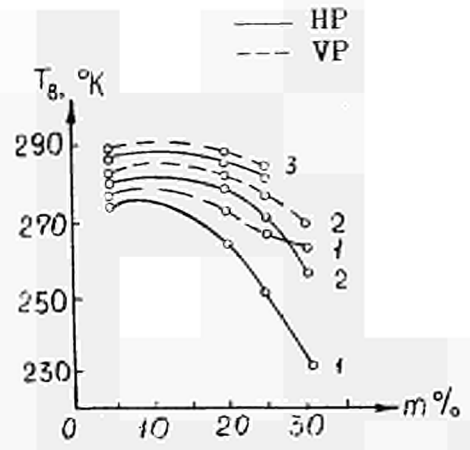


Figure 4. The bare loam RCS dependence on moisture (7 GHz range) [4].



1 - $d_h=1\text{mm}$; 2 - $d_h=11\text{mm}$; 3 - $d_h=35\text{mm}$.

Fig. 5. Moisture T_g dependencies of bare black earth ($\varphi=45^\circ$).

3. The "work" hypothesis

It is possible to suppose that two factors has influence on the above mentioned peculiarities RCS (m) and $T_g(m)$ dependencies.

FIRST FACTOR. A presence of three different form of soil humidity and namely: free water, firmly connected (or absorbed water) and crumbly connected water.

It is useful to remind that "free water" is water filling soil pores (emptiness), subjected by capillary and gravity forces influence as well as evaporable and condensable water for ordinary temperature of near grounding air. A permittivity value such form of water has a significant dependence on electromagnetic frequency and amount from 8-10 up to 75-80 digits accordingly for short millimeter and decimeter waves band.

The connected form of water has a series of phases that differed its interconnection with soil matter as on crystal-grate level of soil components as and in the form of film water adsorbed with soil particles surface (with depths of films composed from 6-8 up to 10-20 molecular layers). At that (and it is important for our following consideration) the connected water has the anomalous low permittivity value (ϵ) and small mobility - that is the property similar of radio frequency property of ice.

Here it is necessary to note that influence of soil water phases transitions to its radio physical properties are studied very weakly in this time. Indeed only one author team's articles take to solid for such investigation direction [5-6]. And one of important conclusion for us from these investigations results is a note about existence of essential dependence of the soil water connected form containing on soil kind. So the values of connected soil water (on ratio to maximum or full soil capacity) might has for sand from 5% up to 25% and to 50% accordingly for loam and yellow earth soil. The last note is following from figure 6 [6]. Here χ is an emissive coefficient ($\chi = 1 - p$, then p - is integral reflecting coefficient).

SECOND FACTOR. A presence of soil micro structure and soil density changes on dependence of soil humidity change. (At that as it follow from our previously

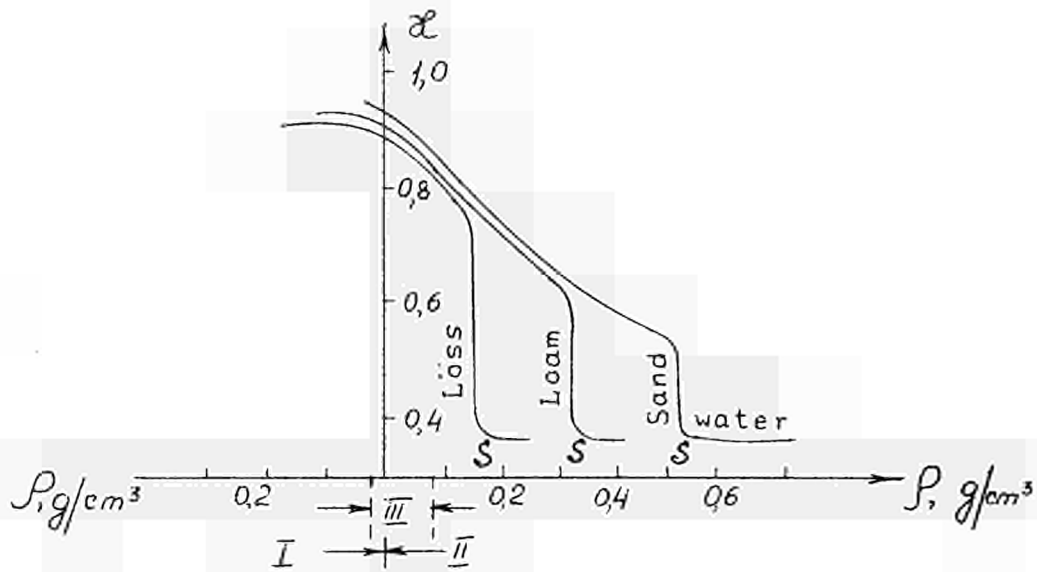


Figure 6. The emissive coefficient dependence on moisture containing for different kind of soil [6].

1 - firmly connected (absorbed) water; II - free water; III - intermediate state (crumbly connected water); S - water saturation state

observations the above mentioned changes depends on soil kind and displays at process of cramping or distraction of soil lumps. These processes are more intensive at diapason of minimum and near middle values of soil humidity).

Figure 7 show influence of the differences of soil density to dependence of soil emissive coefficient on soil humidity. Here it is seen essential influence of soil density change (from 1g/cm^3 up to 1.5g/cm^3) on it emissive coefficient (and as result and it integral reflection coefficient). This influence is essentially not only for big values but and for small humidity values (characteristic for existing of connected soil humidity forms only).

Besides an arising, crumpling or distracting lamps processes in micro structure of soil evidently might influence as on soil density change as and on volume diffraction contribution into summary signal as well as on surface diffraction contribution that take place because of changing of small scales roughness ingredients of surface roughness spectrum.

Taking into account these two factors I would like to offer the following explanation of above mentioned phenomenon of RCS(m) dependence nonlinearity.

With increasing of soil humidity from minimal values up to certain values there are not any essential modifications of soil permittivity value because increase of firmly and crumbly connected and thin filmy phases of soil water take place at that stage. However modification of soil micro structure and soil density take place with that increasing of soil humidity. And it is cause of decrease of solid scattering contribution in process of the signal back scattering. I think the totality of these two causes lead toward the decrease of RCS value.

(Here an analogy with snow cover which we studied too may be appropriated. It is known the solid scattering nature dominating for dry snow. And as our data shows

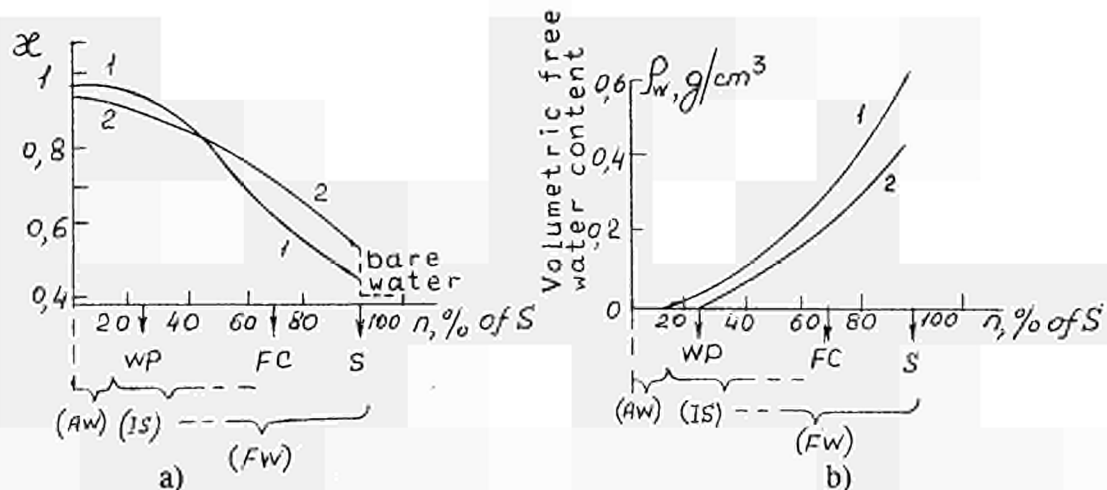


Figure 7. The interdependence of characteristics of radiation with soil (gidrological) constants and forms of water [5].

WP - wilting point; FC - field capacity; S - state of saturation; AW - absorbed water; FW - free water; IS - intermediate state; (1 - $1\text{g}/\text{cm}^3$, 2 - $1.5\text{g}/\text{cm}^3$).

snow RCS decreases with snow melting, aging and transforming of snow micro structure).

On next stage of increase of soil humidity the increase of free water contents in soil take place. And such further increase of soil humidity leads toward increasing of soil permittivity and decreasing of soil skin layer depth. And as result we have the increasing of RCS value, already in accordance with conceptions wide spread in present time.

By the way If this suggested explanation is near to reality it is possible to wait an absence of smaller expression of noted "turning" in curve of RCS-to-humidity dependence for sand surface. Indeed it is known the contents of firmly and crumbly connected and filmy water in sand is several times smaller of one in loam or black earth. Besides according to our observations the sand soil has small changes its micro structure during change its humidity as regards to most of other kind of soil.

4. The ways of suppose investigations project

Of cause this explanation we can accept as working (or previous) hypothesis only. A confirmation or specification one depends on answer on such opened and weakly illustrated questions as:- investigations of soil kind influence on distribution its connected and free soil humidity forms as well as on its micro structure and density change with its total humidity change (and as result on its permittivity change);

- correlation between weight and volume humidity value for different kind of soil;
- correlation between volume and surface diffraction contributions into summary receipt signal for soil surfaces with different values of roughness and soil kind as well as influence its causes on skin-layers depth;
- correct comparison of back scattering and radio heat emissive characteristics conjointly carried out with experimental way and at wide band of waves.

Detailed investigations these questions (every one of its has besides an independent scientific importance) necessary as for valid quantity explanation of soil back scattering and radio heat emission nature of processes as for rise of interpretation accuracy of airspace remote sensing data.

These days the EMSL provide a successful activity with "soil moisture" research program. There are the unique wide waves band radar [7] and radiometer systems complex that is using in frame this program already. Besides worked off methods of carrying out of radio physical and accompanying geophysical measurements of soil specimens as well as there are an experience of interaction and take place a co-ordination activity between different Italian and European Community research group who interesting in investigation same problems at radio physical or biogeophysical aspects.

In view of this if to take into account above mentioned facts and argumentation here is offering to realize the additional investigation program of radio physical properties interconnection of bare soil with its geophysical properties using the unique and big possibilities of EMSL. This program must include such three main and interconnected activity directions as:- providing of the soil specimens production and carrying out of accompanying control and investigation of the soil specimens geophysical properties; —apparatus and methodical guarantee of the radio physical and geophysical investigations; —carrying out of the measurements radio physical cycles as well as collection, accumulation and analyze got data and its theoretical generalization and substantiation.

4.1 THE TEST-SPECIMENS AND ACCOMPANYING MEASUREMENTS.

For the investigation of soil kind influence to processes of micro structure changing, to correlation of different soil moisture forms and changing at that the soil density, to correlation of volume and weight soil humidity as well as for carrying out of radio physical measurements it is necessary to choice about five or six soil types that are most differ with its above mentioned properties:

- 1) fine-grained sand;
- 2) coarse-grained sand;
- 3) clay;
- 4) loamy soil;
- 5) black earth;
- 6) yellow earth (löss).

At that it is necessary realize about three or four different shapes of roughness with rms. values from 0.3mm up to 40mm approximately for every one.

The forming of surface roughness we suppose to realize by an oppressing way with special worked out stamps (using modern EMSL's technologies [8]). For the control of soil micro structure dynamic and different forms of soil humidity and an other it suppose a calling of experienced soil-authority specialists (for example from Kharkov State University, Universities of Basel, Naples and Gent, Politecnico di Milano).

4.2 THE APPARATUS AND METHODOLOGICAL MAINTENANCE.

For the soil radio physical measuring carrying out it suppose to use the wide waves band (from 2 GHz up to 26 GHz) scatterometer and radiometer apparatus. At that it keep in mind that this apparatus complex and methodical maintenance there are at EMSL already [7] as and laboratory measuring apparatus for catch of soil permittivity values [9].

As to radiometer systems, it is necessary its create (including such radiometers might be created in our institute [10-12]) or use the other institution's one. For example a suitable radiometers are at IROE, Florence and its are using already at the EMSL[13].

Besides it is desirable to use not only usual for remote sensing of soil moisture waves band but and short millimeter waves system for such kind program. It is connected with although an application of short millimeter is not actuality for practice of soil moisture remote sensing (because of very thin depth of soil skin layers amounted from 2-3mm up to 10-15mm) however role of such canal as auxiliary canal might be expediently for understanding of process diffraction physics. Particularly the one might be useful for learning of influence of volume diffraction process and diffraction in thin upper surface layer to integral back scattering process of moisture soil.

4.3 THE CARRYING OUT OF THE RADIO PHYSICAL MEASURING CYCLES.

The realization of the radio physical and geophysical (accompanying) above mentioned observations it is necessary provide at narrow co-operation (and it is vary important) between specialists of both of its spheres.

In EMSL (with participants of "Soil Moisture" program from other organizations) and in RI NAS there are an experience such interacting. At that the apparatus and methods of radar measuring and its data collection and analysis are enough developed in the EMSL.

At same time the similar situation take place in RI NAS if say about radiometer investigations.

As to theoretical substantiation got data in particularly a choice of soil-water mixture model for account of permittivity value for different kind of soil, a choice and application of models that adequately reflect the process of back scattering and radio heat emission [14-15], that part of offered project might be decided too on basis of EMSL and RI NAS possibilities with calling other organization (for example with the Universite Catholique de Louvain, Belgium or the Politecnico di Milano, Italy).

So it is possible conclude that these days on basis of the EMSL and around one take place a propitious situation for decision questions and problem placed in this article.

5. Conclusion.

The weak clarity of radio physical properties of the small and middle moisture soil that lead tononlinearity of radar cross sections and radio heat temperature dependencies on soil humidity for some kind of soil are noting. The "work" hypothesis for explanation its nonlinearities as well as the propositions carrying out of additional investigations this problem and the formulated about its questions are offering by author.

REFERENCES.

- [1] Ruzhentsev N.V. and Churilov V.P., Results of radiolocation and radiometer investigations of Earth cover and Atmosphere at the short millimeter wave range //"Space Science and technique Journal". Problem articles of science. Kiev, Naukova Dumka, 1992, issue 7, pp. 99-115. (in Russian)
- [2] Ruzhentsev N.V. and Churilov V.P. Terrain radiation - measurement Investigation at 3-mm wave band // International Journal of Infrared and Millimeter Waves, 1996, 17pp. (accepted for publication in v.17, N 2)
- [3] Ruzhentsev N.V. and Churilov V.P. Earth covers back scattering characteristics at the frequency 94 GHz and 136 GHz // International Journal of Infrared and Millimeter Waves, 1996, 15pp. (accepted for publication in v.17, N 4)
- [4] Ulaby F,T. Radar measurement of soil moisture content. IEEE Transactions, 1974, v. AP-22, N 2. p. 257-265.
- [5] A. M. Shutko Microwave radiometry of lands under natural and artificial moistening. IEEE Transaction on GARS, 1982, v. GE-20, N 1, p. 18-26.
- [6] N. A. Armand and A. M. Shutko Earth covers moisture properties determination by radiometry way / The modern radio technique and electronic problems. Edited by V.A. Kotelnikov, - Moskow, "Nauka" press,1987, p. 118-131.
- [7] The EMSL experimental facilities // EMSL's second announcement of opportunity (Annex 1), JRC, Ispra, Italy, 1995.
- [8] D. Tarchi Random surface structure for soil samples in microwave experiments. //EMSL News-Letter, N5, JRC, Ispra, Italy, April 1995.
- [9] M. Weinberger Dielectric properties of nonsolid lossy material. // EMSL News-Letter, N8, JRC, Ispra, Italy, June 1996.
- [10] Belobrov A.V., Ruzhentsev N.V. and Churilov V.P. Scatterometer 140 GHz for polarization investigation of earth covers Radar Cross Sections // Proc. of All-Unionconf. "Radar remote sensing systems " (Kamensk-Uralsky, Sept. 1988), Sverdlovsk, 1988, pp. 146-147. (in russ.)
- [11] Podyachi V.I. and Ruzhentsev N.V. Aircraft radiometer system at millimeter waves band // Proc. of All-Union conf. "Radar remote sensing systems " (Kamensk-Uralsky, Sept. 1988), Sverdlovsk, 1988, pp. 144-145. (in russ.)
- [12] Ruzhentsev N. V. Radiometer without diplexer // Proc. of 21st All-Union conf. "Radioastronomical equipment", Erevan, 1989, p.45-46.
- [13] The IROE was EMSL's guest for radiometer test measurements. // EMSL News-Letter, N8, JRC, Ispra, Italy, June 1996.
- [14] Belobrov A.V. and Ruzhentsev N.V. Experimental and theoretical polarization investigations of back scattering characteristics of terrain surface over the short millimeter wave range // Proc. of III All-Union School-Symposium on propagation of millimeter and submillimeter waves in the atmosphere. (St. Saltov, October, 1989), pp.103-104. (in Russ.)
- [15] F.G. Bass and Io.M. Fuks The waves diffraction on statistical roughness surface / Moskow, "Nauka" press, 1978, 424pp..

List of Participants

F. Albanese

CNR
via Amendola 166/5
70125 Bari, Italia
Phone +39 80 5588 2293
Fax +39 80 548 4311
email albanese@ercole.ba.cnr.it

A. Bedidi

Université de Mame La Vallée
2 rue de la Butte Verte
93166 Noisy La Grande, France
Phone +33 1 49 32 9074
Fax +33 1 49 32 9137
email bedidi@univ.mlv.fr

P. Borderies

CERT/ONERA
@ave.E.Belin
31055 Toulouse Cedex, France
Phone +33 62 25 2718
Fax +33 62 25 2527
email Pierre.Borderies@oncertr.fr

A. Broquetas

Dept TSC, Ed. D3, Campus Nord
UPC, Gran Capitain s/n
08034 Barcelona, Espana
Phone +34 3 401 7221
Fax +34 3 401 7232
email toni.@voltor.upc.es

D. Casarano

Dipt. Interateneo di Fisica
via Amendola 173
70125 Bari, Italia
Phone +39 80 544 3166
Fax +39 80 544 2434
email casarano@expba1.ba.infn.it

P. Colombo

DIIAR Politecnico di Milano
20133 Milano, Italia
Phone +39 2 55 10 243
Fax +39 2 23 99 6207

P. Coppo

CETEM-FLORENCE
via Panciatichi 64
50127 Firenze, Italia
Phone +39 55 2750 4779
Fax +39 55 70 0685

P. Corona

Istituto Universitario Navale
via Acton 38
80133 Napoli, Italia
Phone +39 81 551 3976
Fax +39 81 551 2884

G. Cottard

S.A.T.I.M.O. - Le Pin, Rue de la
Terre de Feu, z.a. de Courtaboe
91952 Les Ulis, France
Phone +33 1 69 29 02 47
Fax +33 1 69 29 02 27

Y. Crutzen

JRC ISIS Industrie environ
via E. Fermi
21020 Ispra, Italia
Phone +39 3322 78 9371
Fax +39 332 78 9150
email Yves.Crutzen@jrc.it

F. De Masi

DIIAR Politecnico di Milano
20133 Milano, Italia
Phone +39 2 2896 495
Fax +39 2 23 99 6207

A. Franchois

JRC-SAI Advanced Techniques
T.P. 720
via E. Fermi
21020 Ispra, Italia
Phone +39 332 78 9131
Fax +39 332 78 5772
email Ann.Franchois@jrc.it

J. Fortuny

JRC - SAI Advanced Techniques
T.P. 720
via E. Fermi
21020 Ispra, Italia
Phone +39 332 78 5104
Fax +39 332 78 5772
email Joaquim.Fortuny@jrc.it

J. Groot

TNO-FEL - P.O. Box 96864
22509 The Hague
The Netherlands
Phone +31 70 3740 432
Fax +31 70 3280 961
email groot.@@fel.tno.nl

R.H. Lang

George Washington University
Dept. of Elect. Engineering and
Comp. Science
20052 Washington D.C., USA

E. Legros

DGA-CELAR - Route de Lailé
35170 Bruz, France
Phone +33 99 42 9058
Fax +33 99 42 9094

D. Lesseller

LSS (CNRS-SUPELES)
ESE- Plateau de Moulon
91192 Gif-sur-Yvette Cedex
France
Phone +33 1 6985 1561
Fax +33 1 6941 3060
email lesselier@supelec.fr

K. Lukin

NAS of Ukraine, In-te of
Radiophysics and Electro Academy
of Sciences
12, Akad. Proskura St.
310085 Kharkov, Ukraine
Phone +38 0572 448349
Fax +38 0572 441105
email lukin@ire.karkov.ua

M. Mancini

Politecnico di Milano DIIAR
P.zza Leonardo da Vinci 32
20133 Milano, Italia
Phone +39 2 2399 6209
Fax +39 22 2399 6207
email mancini@idral.iar.polimi.H

J.P. Marcellin

O.N.E.R.A. - Fort de Palaiseau
91120 Palaiseau, France
Phone +33 1 6993 6268
Fax +33 1 6993 6269
email marcel@onera.fr

M. Martin-Nelra

European Space Agency
P.O. BOX 299
22200 AG Noorwijk
The Netherlands
Phone +31 71 565 4052
Fax +31 71 5654 596
email mneira@estec.esa.nl

F. Mattia

CNR-ITIS
c/o CGS - ASI Loc. Terlecchia
75100 Matera, Italia
Phone +39 835 377 7282
Fax +39 835 33 9027
email mattia@asirnto.rnt.asi.it

O. Migliore

Torino, Italia
Phone +39 11 949 3819
Fax +39 11 949 3819
email o.migliore@crf.it

S. Morucci

JRC-ISIS Industrie Environ
via E. Fermi
21020 Ispra, Italia
Phone +39 332 78 9878
Fax +39 332 78 5378
email Stephane.Morucci#@jrc.it

P. Nardone

Université Libre de Bruxelles
CP 231, Sciences Physique
Bld. du Triomphe
1050 Bruxelles, Belgium
Phone +322 22 650 5515
Fax +322 2 650 5767
email pnardon@ulbac.be

G. Nesti

JRC-SAI Advanced Techniques
T.P. 720
via E. Fermi
21020 Ispra, Italia
Phone +39 332 78 5922
Fax +39 3322 78 5772
email Giuseppe.Nesti@jrc.it

E. Ohlmer

JRC-SAI Advanced Techniques
T.P. 720
via E. Fermi
21020 Ispra, Italia
Phone +39 332 78 9315
Fax +39 332 78 57722
email Eggert.Ohlmer@jrc.it

C. Pichot

CNRS Université de Nice - Sophia
antipolis, France
Phone +33 92294 22828
Fax +33 9294 2812
email pichot@alto.unice.fr

F. Posa

Politecnico di Bari
Bari, Italia
Phone +39 80 544 3171
Fax +39 80 544 2434

J. Reddy

European Space Agency
ESTEC
Keplerlaan 1
2200 AG, The Netherlands
Phone +31 71 565 4420
Fax +31 71 565 4999
email jreddy@estec.esa.nl

B. Röde

DLR, Inst. f. HF-Teknik
Postfach 1116
82230 Wessling, Deutschland
Phone +49 8153 282351
Fax +49 8153 281135

J.P. Rudant

Université Pierre et Marie Curie
tour 26, etage 1, 4 Place Jussieu
75005 Paris, France
Phone +33 1 4427 5087
Fax +33 1 4427 5085
email jpr@bs.iussieu.fr

H. Rudolf

JRC-SAI Advanced Techniques
T.P. 720
via E. Fermi
21020 Ispra, Italia
Phone +39 332 78 5986
Fax +39 3322 78 5772
email Hans.Rudolf@2jrc.it

N. Ruzhentsev

Radio Astronomy Institute of NAS
of Ukraine
\$ Krasnoznarrlennaya Str.
3100022 Kharkov, Ukraine
Phone +38 0572 476506
Fax +38 0572 476506
email nns@rian.kharkov.ua

M. Saillard

CNRS Lab. Optique
Electromagnétique
Faculte de St. Jerome
13397 Marseille Cedex 20, France
Phone +33 91 670936
Fax +33 91 674428
email marc@loe.univ.mrs.f

K. Schmitt

University of Karlsruhe
Kaiserstrasse 12
76128 Karlsruhe, Deutschland
Phone +49 721 966 1574
Fax +49 721 69 1865
email kerl@ihewap.etc.uni-karls-
nuhe.de

A. Sieber

JRC-SAI Advanced Techniques
T.P. 272
via E. Fermi
21020 Ispra, Italia
Phone +39 3322 78 9089
Fax +39 3322 78 5469
email Alois.Sieber@jrc.it

U. Smilansky

Weszmans Inst. of Science
Dept. of Physics of Complex
Systems
76100 Rehovot, Israel
Phone +972 8 934 3180
Fax +972 8 934 4157
email fnsmila@weizmann.ac.il

G. Solaas

ESA/ESRIN/RS/ED
Via Galileo Galilei
00044 Frascati, Italia
Phone +39 6 94180 628
Fax +39 6 94180 622

J.C. Souyrls

CESBIO - BPI 2801
31055 Toulouse Cedex, France
Phone +33 1 61 55 8584
Fax +33 1 61 55 85 00
email sourys@cesbio.cnes.fr

D. Tarchi

JRC-SAI Advanced Techniques
T.P. 720
via E. Fermi
21020 Ispra, Italia
Phone +39 332 78 5143
Fax +39 332 78 5772
email Dario.Tarchi@jrc.it

T. Tares

JRC-SAI Advanced Techniques
T.P. 272
via E. Fermi
21020 Ispra, Italia
Phone +39 332 78 6110
Fax +39 3322 78 5469
email teemu.tares@jrc.it

G. Toso

Università degli Studi di Firenze
lab. di microonde
Faculté St. Jerdmo
13397 Marseille Cedex 20, France
Phone +33 91 670936
Fax +33 91 674428
email toso@loe.univ-mars.fr

P. Troch

University of Ghent
Coupure Links 653
9000 Gent, Belgium
Phone +322 22 264 6138
Fax +32 2 2264 6236
email Peter.Troch@rug.ac.be

D. Vidal-Madjar

CEIP/CNRS-UVSQ
10-12 Ave. de l'Europe
78140 Velizy, France
Fax+33 1 39254822
email daniel.vWal-
madjar@cetp.ipsl.fr

R. Winter

JRC-SAI - Director
T.P. 441
via E. Fermi
21020 Ispra, Italia
Phone +39 332 78 9765
Fax +39 332 78 9536
email Rudolf.Winter@jrc.it

European Commission

**EUR 17326 – 1st EMSL User Workshop
Proceedings**

1996 – IV, 158 pp. – 21.0 x 29.7 cm

CL-NA-17326-EN-C

These Proceedings include a number of papers covering the topics presented and discussed at the 1st EMSL User Workshop, held at the JRC, Ispra on 23 and 24 April 1996.

